Study of T Cell Activation and Migration at the Single-Cell and Single-Molecule Level

by

Irene Yin-Ting Chang

S.B. Brown University (2001)
M.S. Stanford University (2004)

Submitted to the Department of Materials Science and Engineering
in partial fulfillment of the requirements for the degree of

Doctor of Philosophy in Materials Science and Engineering

at the

MASSACHUSETTS INSTITUTE OF TECHNOLOGY

June 2011

Author……
Department of Materials Science and Engineering
May 3, 2011

Certified by……
Jianzhu Chen
Cottrell Professor of Immunology
Thesis Supervisor

Certified by……
Darrell Irvine
Thesis Reader, Department of Materials Science and Engineering

Accepted by……
Christopher Schuh
Chair, Departmental Committee on Graduate Students

Study of T Cell Activation and Migration at the Single-Cell and Single-Molecule Level

by

Irene Yin-Ting Chang

Submitted to the Department of Materials Science and Engineering
on May 3, 2011, in partial fulfillment of the
requirements for the degree of
Doctor of Philosophy in Materials Science and Engineering

Abstract

T cells are required by their immunological roles to recirculate in the body and migrate to tissue sites, a journey that exposes them to distorting forces and physical obstacles that hinder their movement. Therefore, they must possess appropriate deformability to accommodate and adapt to these mechanical stimuli to migrate unimpeded. Since T cells alter their physical properties and migration routes upon activation, they may possess dissimilar mechanical properties as a result of this process. This hypothesis was tested using the techniques micropipette aspiration and atomic force microscopy, which allow the investigation of the elastic and viscous responses of single T cells. It was discovered that the activation process reduced T cell stiffness by more than three folds, a finding that agrees with the motility gain observed in activated T cells. The same testing procedure was applied to Wiskott-Aldrich syndrome protein (WASp)-deficient T cells that exhibit abnormal morphology and impaired chemotaxis. The stiffness of the diseased cells in the naïve state was 1.5 times less than that of the non-diseased cells, a result that may be due to the disrupted polymerization and cross-linking of the actin cytoskeleton in the absence of WASp, a regulator of actin growth and organization. Furthermore, the viscous response of the diseased cells in the activated state was found to be impaired. Chemokines were found to dramatically reduce the stiffness of naïve T cells that were induced to migrate. These findings suggest that WASp plays an important role in maintaining cell mechanical property and facilitating T cell extravasation by tailoring the cells' deformability. At the molecular level, activation of T cells is triggered by the binding of their surface receptors to antigens, a mechanism that is also key in T cell development. In both cases, the bond strength, conventionally measured by the affinity (K_D) or the dissociation rate (k_{off}) of the interacting pair, dictates the biological outcome. Since a few weak interactions may nudge a sub-threshold signal over the threshold strength, and observing that the current methods for measuring K_D and k_{off} lack the resolution to detect very weak bonds, this work explored the possibility of utilizing dynamic force spectroscopy (DFS) to study very weak binding strengths. Preliminary results confirm this capability.

Thesis Supervisors: Jianzhu Chen, Subra Suresh
Title: Cottrell Professor of Immunology, Vannevar Bush Professor of Engineering

Acknowledgments

First, I acknowledge my advisors Prof. Jianzhu Chen and Prof. Subra Suresh for their continued support and guidance throughout my graduate studies at MIT. Their enthusiasm toward and dedications to scientific research have been an inspiration. I am very grateful to my thesis committee members Prof. Arup Chakraborty, Prof. Darrell Irvine, and Prof. Lorna Gibson, for their guidance, suggestions, and feedbacks on my research work. I want to extend a special thank you to Prof. Lorna Gibson for agreeing to serve on my thesis committee upon a short notice, as well as to Prof. Darrell Irvine for co-advising me towards the end of my PhD work. I am also extremely grateful to Singapore MIT Alliance – Biology and Singapore-MIT Alliance for Research and Technology for funding this thesis work.

I am very thankful toward Dr. Scott Snapper and his research group members for the generous gift of WAS-/- mice and help with the transition of these animals to MIT. I also want to thank Prof. David Kranz and his research group for their help with TCR and pMHC synthesis, especially Dr. Jennifer Stone's suggestions and advice. I am very grateful to Dr. Ming Dao for his advice and guidance. I am also very grateful to Dr. Ching-Hung Shen and Dr. Vinay Mahajan for their guidance and help on all the biological procedures involved in this work, as well as for all the inspiring discussions. I am very thankful to Rosemary Zhang for her help with the micropipette aspiration experiments. I am deeply appreciative of Kenneth Greene and George Labonte in Prof. Subra Suresh's lab for their help with the general lab- and school-related affairs. I also want to thank all members of the Chen Lab and the Suresh Lab for the support, guidance, and friendship that they have given me. I would also like to thank Thibault Prevost, Kristin Bernick, Nathan Hammond, Yoda Patta, Dr. Ming Dao, David Quinn, and Sotiris for their helpful academic interactions.

Lastly, I want to extend the deepest gratitude to my parents and my brother.

Contents

List of Figures

complex. Class I MHC consists of a transmembrane α chain noncovalently associated with a β_2-microglubulin. The α chain has three domains, with the $\alpha 1$ and $\alpha 2$ domains forming the peptide-binding cleft. Class II MHC consists of a α chain and a β chain, with each chain having two domains. The $\alpha 1$ and $\beta 1$ domains act together to bind a peptide. Illustration from reference 30 [30]. P.31

1-8 MHC antigen presentation. A cell infected by a virus produces viral proteins, which are degraded into peptide through the cytosolic pathway. The viral peptides are bound to class I MHC molecules in the endoplasmic reticulum, and the pMHC complexes are subsequently transported to the surface of the infected host cell, where they can be recognized by $CD8^+$ T_C cells. Antigens that are endocytosed are degraded into peptides via the endocytic pathway. These peptides bind class II MHC molecules, and the resultant pMHC complexes are transported to and inserted into the cell membrane, where they can be recognized by $CD4^+$ T_H cells. Illustration from reference 31 [31]. P.33

1-9 Binding of TCR to pMHC. A TCR binds to the peptide and the variable region of a pMHC, while the T cell coreceptor CD8 (T_C cell) or CD4 (T_H cell) binds to the constant region of the same MHC molecule. Accessory molecules on the surface of the T cell and the APC also pair to help stabilize the TCR-pMHC binding. These interacting pairs include LFA-1/ICAM, CD28/B7, CD2/CD58, and CD45R/CD45. Illustration from reference 32 [32]. P.34

1-10 Structure of an immunological synapse (IS). A IS is composed of concentric regions of SMACs containing segregated molecular species. The cSMAC is enriched in pairs of TCR/pMHC, CD28/CD80, CTLA4/CD86, and protein kinase C-θ, one of the downstream signaling effectors of the activation process. The pSMAC is concentrated with mainly adhesion molecules including pairs of LFA-1/ICAM-1, as well as the cytoskeletal linker talin and the coreceptor CD4 or CD8. The outermost region is the dSMAC, which contains bulky molecules such as CD43 and CD45. Illustration from Huppa and Davis [33]. P.36

2-1 Extravasation of naïve (top) and activated (bottom) T cells. Naïve T cells circulate to secondary lymphoid tissues and egress via HEVs, while activated T cells travel to tertiary extralymphoid tissues and enter which through postcapillary venules. Endothelial cells at the two exit sites have dissimilar shapes, as depicted above, being cuboidal and flattened at the HEVs and the postcapillary venules, respectively. Despite these differences, both naïve and activated T cells extravasate the vessel wall to enter the tissue space. Illustration from Norman *et al.* [16] p.43

2-2 Arrangement of actin microfilaments and microtubles at the site of TCR ligation. (Left) Actin polarizes and polymerizes at the site to form a platform that helps recruit cell activation signaling molecules and faciliates their interactions. (Right) MTOCs also transloctes to the TRC engagement site to form a delivery

2-8 Fitting micropipette aspiration data using the half-space model to derive apparent Young's modulus values for T cells. Even though the data shown here were obtained from naïve WT (Balb/c) T cells, the linear fits (solid lines) are representative and characteristic of all the cell populations tested in this work. The equations for five of the liner fits are shown. The modulus is calculated from the slope of a linear fit as described in the text. P.77

2-9 Average apparent Young's modulus of WT T cells before (niave) and after (activated) cell activation as determined by the micropipette aspiration method. The modulus is 290+/-102 Pa (mean +/- SD) and 94+/-49 Pa for naïve and activated WT T cells, respectively. The error bars designate the standard deviation. P.78

2-10 (left) A representative approach curve from an AFM cell indentation experiment fitted with the linear elastic Hertz model. The good overlap of the Hertzian fit (red line) and the experimental data indicates goodness of the model. (right) Variation of the apparent Young's modulus of a T cell with cell indentation depth. The shape of the plot is characteristic of both naïve and activated T cells. The initial fluctuations reflecting the uncertain contact conditions quickly subside and stabilize to yield a constant modulus value, indicating that no substrate effect was involved in the indentation process. P.79

2-11 Variation of the apparent Young's modulus of naïve and activated WT T cells with AFM indentation speed. Cells were tested at 200 nm/sec, 1 μm/sec, 10 μm/sec, 20 μm/sec, and 50 μm/sec. The data points shown are the mean of the modulus values obtained at the indicated testing speeds. The modulus of naïve T cells at the five speeds were determined as 264+/-87 (n=17), 293+/-119 (n=17), 358+/-120 (n=21), 454+/-116 (n=19), and 525+/-99 (n=22) Pa. Similarly, the modulus for activated T cells were found to be 158+/-47 (n=23), 167+/-50 (n=30), 205+/-74 (n=29), 207+/-54 (n=23), and 257+/-91 (n=27) Pa. P.80

2-12 (Left panel) Average apparent Young's modulus of WAS-/- T cells before (niave) and after (activated) cell activation as determined by the micropipette aspiration method. The modulus is 190+/-69 Pa (mean +/- SD) and 121+/-41 Pa for naïve and activated WAS-/- T cells, respectively. (Right panel) The average moduli for WT T cells before and after activation are shown side-by-side for comparison. The error bars designate the standard deviation. P.82

2-13 Variation of the apparent Young's modulus of WT and WAS-/- T cells in the naïve (left panel) and activated (right panel) state with AFM indentation speed. Cells were tested at 200 nm/sec, 1 μm/sec, 10 μm/sec, 20 μm/sec, and 50 μm/sec. The data points shown are the mean of the modulus values obtained at the indicated testing speeds. For naïve WAS-/- T cells, the elastic moduli corresponding to the tested speeds were 220+/-48 (n=17), 217+/-65 (n=43),

320+/-77 (n=22), 386+/-131 (n=21), and 525+/-150 (n=14) Pa. (Left panel) The shape similarity of the curves for the former suggests that naïve WT and WAS-/- T cells respond to increased deformation rates with a similar resistance. (Right panel) Compared to the steady rise in the modulus observed for activated WT T cells, the unvarying stiffness in activated WAS-/- T cells below 20 μm/sec suggests an impaired viscous response. The elastic moduli for these cells are 135+/- 40 (n=17), 131+/-48 (n=27), 136+/-33 (n=20), 133+/-30 (n=20), and 222+/-53 (n=11) Pa. P.83

2-14 FACS analysis of phenotype of naïve WT T cells induced to migrate by the chemokine CCL19. T cells were first gated on PI to exclude dead cells (not shown). The cell samples tested were naïve T cells not exposed to CCL 19 (A, D), cells that remained in the insert after CCL19 exposure (100 ng/mL) for seven hours (B, E), and cells that migrated across the insert membrane after the same chemokine treatment (C, F). Gating on Thy1 (A-C), one marker that identifies T cells, revealed that more than 99% of the cells in all three samples were most likely T cells. Gating simultaneously on CD62L and CD44 (D-F) showed that a similar percentage of cells stained CD62L high and CD44 low, indicative of the naïve T cell phenotype. P.85

2-15 The average apparent Young's modulus of WT and WAS-/- T cells under different treatment conditions determined by micropipette aspiration. The modulus is 128+/-33 Pa (mean +/- SD) and 152+/-102 Pa for CCL19-stimulated WT and WAS-/- T cells, respectively. The average moduli for WT and WAS-/- T cells before and after activation were described in the previous sections and are shown side-by-side here for comparison. The error bars designate the standard deviation. P.87

2-16 Confocal microscopy images of fluorescently labeled peripheral blood T lymphocytes (PBT) upon exposure to the chemokine SDF-1 showing cytoskeleton rearrangement and polarization. In a resting PBT, actin microfilaments form a shell that lies directly below the cell membrane (a, blue). Microtubules radiate outward from MTOCs (b, green), and vimentin intermediate filaments form a cage-like network that permeates the cytoplasm (c, red). After a 3-min exposure to 100 ng/mL of chemokine, a PBT polarizes and exhibit lamellapodia in the leading edge and an uropod in the cell rear (g). All three cytoskeletal elements undergo reorganization. Actin concentrates in the cell leading edge (d, blue), while both the microtubule (f, green) and intermediate filament (e, red) structures collapse and retract into the uropod. A composite image of the three stainsings from d, e, and f, is shown in g. Scale bar = 5 μm. Figure from Brown *et al.* [100] P.89

2-17 Actin reorganization in normal and WASp-deficient T cells in response to anti-CD3 antibody stimulation. After 5 minutes, F-actin both distributes throughtout the cytoplasm and concentrates in a ring next to the cell cell membrane of

Chapter 1 Introduction

This thesis work is divided into two research projects. In chapter 2, characterization of the mechanical properties of T cells, both healthy and diseased and under different stimulation conditions, is introduced and described in detail. Chapter 3 covers the development of a procedure to apply dynamic force spectroscopy to two different TCR-pMHC systems and delineates the utilization of this technique to derive a dissociation rate for both systems. Chapter 4 summarizes all the findings and contains the conclusions of this research work. Lastly, Chapter 5 describes follow-up studies that may be conducted to broaden the scope of the presented results. This chapter provides a brief description of the motivations behind the two research projects in this work, with each project description preceded by an introduction to the relevant T cell biology as means to facilitate subsequent discussions.

Immune responses are properly executed by the coordination and interplay of innate and adaptive immunity. Innate immunity is nonspecific and targets infectious agents in general. Components of innate immunity can be anatomical barriers such as the skin and the mucous membranes of tissues that barricade the entry of microbes, soluble molecules and special receptors such as antimicrobial peptides, complement proteins, and Toll-like receptors, as well as cellular players including neutrohils, macrophages, dendritic cells, and natural kills cells that can mount generalized immune responses [1]. Adaptive immunity, in contrast, is specific. Recognition of particular antigens triggers immune defense mechanisms that specifically aim at removing the infectious sources. Leukocytes,

commonly known as white blood cells, consist of a family whose members include neutrophils, lymphocytes, monocytes, eosinophils, and basophils. Resting leukocytes are spherical in shape and display many membrane folds and projections called microvilli on their surface. This membrane reservoir enables the cells to deform and enter capillaries with diameters much smaller than those of the cells [2]. Based on function and cell membrane components, lymphocytes can be further classified into B lymphocytes, T lymphocytes, and natural killer cells. The first two subpopulations are the key immune cells that orchestrate adaptive immune responses.

Organs of the immune system can be distinguished by function as the primary and secondary lymphoid organs. The primary lymphoid organs include the bone marrow and the thymus. Precursor cells of B and T lymphocytes arise in the bone marrow as a result of hematopoiesis. They subsequently either mature in the bone marrow to give rise to B lymphocytes, or migrate to the thymus to develop into T lymphocytes. Secondary lymphoid organs encompass lymph nodes, the spleen, and various mucosa-associated lymphoid tissues (MALT). They trap antigens, species that trigger immune responses, and provide an environment for lymphocytes to interact with these antigens to become activated. Primary and secondary lymphoid organs are connected by blood vessels and the lymphatic system.

T lymphocytes, also known as T cells, develop and mature in the thymus, a bi-lobed organ enveloped in a capsule and divided into lobules (Figure 1-1) [3]. Each lobule consists of two compartments, the cortex that occupies the outer compartment and the

medulla that occupies the inner compartment. The thymic cortex is densely packed with immature T cells called thymocytes, which proliferate extensively. These cells interact with various stromal cells in the thymus, including cortical and medullary epithelial cells, dendritic cells, and macrophages, that display high levels of class I and II major histocompatibility complex (MHC) molecules and help select thymocytes for continued development. Thymocytes must have T cell receptor (TCR) that is able to recognize and bind to self MHC, MHC molecules produced in the host. Those that fail to do so

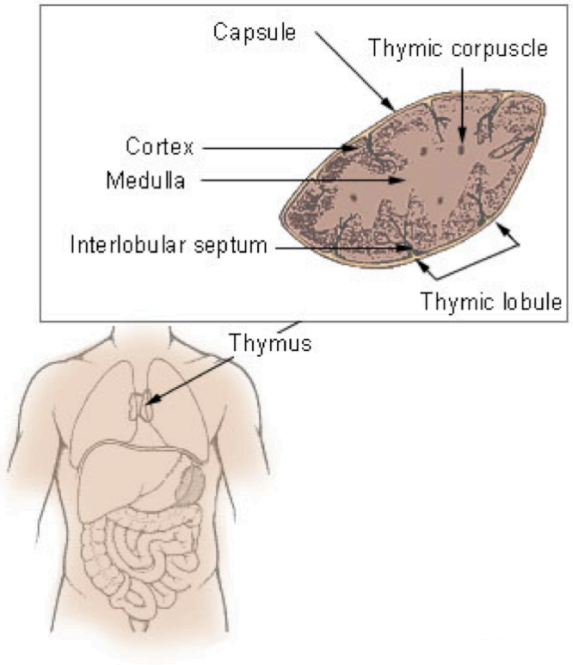

Figure 1-1: Anatomy of the thymus. The thymus is enveloped in a capsule and can be divided into lobules, with each consisting a cortex compartment that occupies the outer region of the thymus, as well as a medulla compartment that occupies the inner thymic region. Illustration from reference 3 [3].

will be deleted through a process called death by neglect. Thymocytes that bind too strongly to either self MHC or self MHC conjugated to self-peptides are negatively selected

and eliminated. Only about 5% of the total thymocytes can satisfy both criteria, referred to as being positively selected, and give rise to a mature T cell repertoire that can distinguish host cells from foreign species while generating minimal autoimmune reactions. During the maturation process, thymocytes move from the cortex to the medulla, where those of higher maturity are sparsely populated. Mature T cells output from the thymus survey the body for any breach in immunity by recirculating between the blood and the lymph systems.

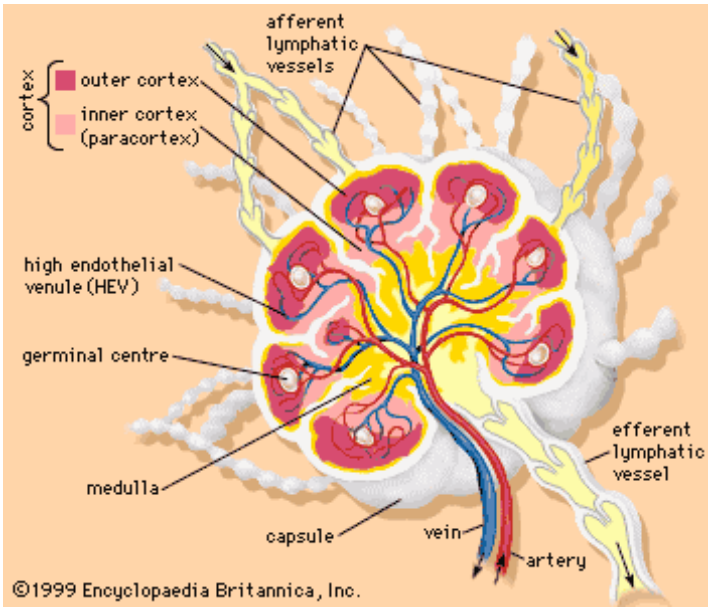

Figure 1-2: Anatomy of a lymph node. A lymph node can be divided into three regions, the outer cortex, the paracortex, and the medulla. Antigens are carried into lymph nodes through the afferent lymphatic vessels and captured by macrophages and dendritic cells residing in the cortex and the paracortex. Lymphocytes enter via HEVs in the postcapillary region. Illustration from reference 4 [4].

Lymph nodes are sites where naïve T cells can become activated by antigen, resulting in the mounting of immune responses. A lymph node is divided into three regions, the cortex that contains mostly B cells, the paracortex that is enriched with helper T (T_H)

cells, and the medulla that has mostly antibody-secreting plasma cells (Figure 1-2) [4]. Antigens are carried into lymph nodes by the lymph, fluid exuded from the blood into the tissue space during normal circulation, and are captured by macrophages and dendritic cells residing in the cortex and the paracortex. The antigens are subsequently processed and presented as pMHC on the surface of these cells. Blood-borne T cells continuously migrate to and enter lymph nodes through the walls of specialized structures called high endothelial venules (HEVs), postcapillary venules that are lined with plump, cuboidal endothelial cells. Unlike lymph nodes that trap antigens from local tissue spaces, the spleen filters blood and traps blood-borne antigens. Thus this lymphoid organ helps mount immune responses against systemic infections.

Lymphocytes are referred to as naïve when they have not interacted with antigen. They are small, inactive cells in the G_0 phase of the cell cycle, from 6 to 8 μm in diameter and contain a large nucleus surrounded by a thin layer of cytoplasm (Figure 1-3) [5]. Upon encountering antigen, these cells are activated and progress through the cell cycle. During this process, they enlarge into lymphoblasts that subsequently proliferate and differentiate into effector cells or memory cells. Effector cells are capable of mounting immune responses against infections. B lymphocytes, commonly referred to as B cells, display immunoglobulin on their surface that can directly recognize and bind antigens. Effector cells of the B-cell lineage are called plasma cells, which are capable of producing antibodies targeting the antigen. The antibody produced is structurally identical to the surface immunoglobulin except that the former is soluble and the latter is membrane-bound. T cells display TCR on their surface (Figure 1-4) [6] and can be subdivided into T_H

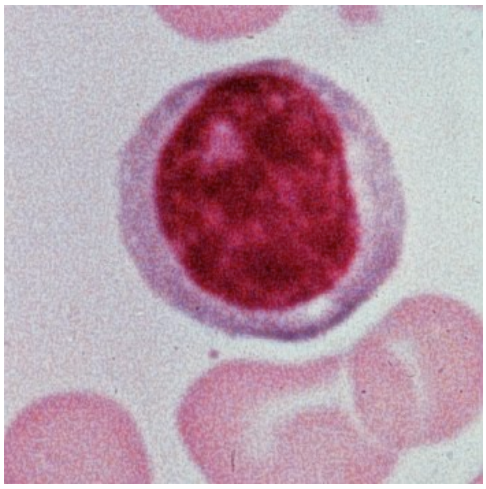

Figure 1-3: Cytostaining of a naïve T lymphocyte. The cell is mostly occupied by a nucleus (red) surrounded by a thin layer of cytoplasm (purple). Image from reference 5 [5].

and T_C (T cytotoxic) cells, depending on whether they possess the CD4 or the CD8 coreceptor, respectively. Effector cells of the T_H lineage secrete cytokines, biomolecules that activate other cell types also involved in immune responses, while those that arise from T_C cells, known as cytotoxic T lymphocytes (CTL), possess cytotoxic functions. Compared to the short lifespan of naïve and effector T cells, memory T cells are long-lived cells that can provide life-long immunity. The immune response induced the first time an antigen is encountered is called a primary immune response. When the same antigen invades again, memory cells generated during the first infection are able to mount a secondary immune response that is increased in intensity and proceeds faster than the primary response.

In order to reach their target lymphoid organs, T cells regardless of their activation state travel in the bloodstream and migrate across the blood vessel wall to reach

their destinations in the tissue space. This process, called extravasation, is multi-stage and involves sequential rolling and tethering, activation, arrest and adhesion, and finally transendothelial migration of the cells (Figure 1-5) [7]. Naïve and activated (effector) T cells selectively migrate to different lymphoid organs. The former recirculates to secondary lymphoid organs in quest of finding antigens, while the latter targets infected tissue sites.

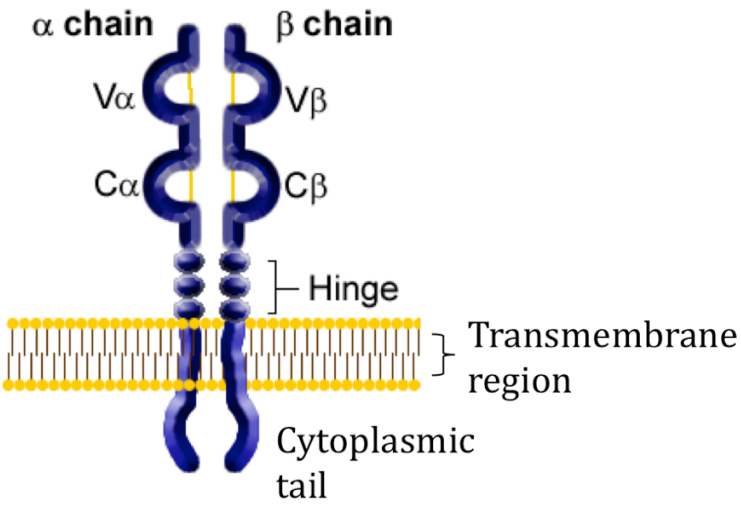

Figure 1-4: Structure of a TCR. TCR is a transmembrane heterodimer that is consisted of an alpha chain and a beta chain. Each chain has a variable region (Vα and Vβ) and a constant region (Cα and Cβ), followed by a hinge region, a membrane-bound sequence, and finally a short cytoplasmic tail. Illustration from reference 6 [6].

This differential travel pattern, governed by the expression of adhesion molecules on both T cells and the tissue endothelium, as well as by the localized chemoattractant sources, is called homing. Unlike naïve T cells that home indiscriminately to the various secondary lymphoid organs, activated T cells are recruited specifically to tissues that display inflammatory signals by recognizing on the inflamed endothelium inflammatory chemokines and special adhesion molecules. The rolling and tethering of T cells arise from

low-affinity binding of mucin-like cell-adhesion molecules (CAMs) to selectins, two families of leukocyte-specific CAMs. The weak attachment transiently tethers a T cell to the endothelium before the fluid shear force detaches the cell. As the cell advances, another tethering event can occur, and repetition of this procedure causes the cell to roll. The process of rolling slows down the T cells enough to allow them to

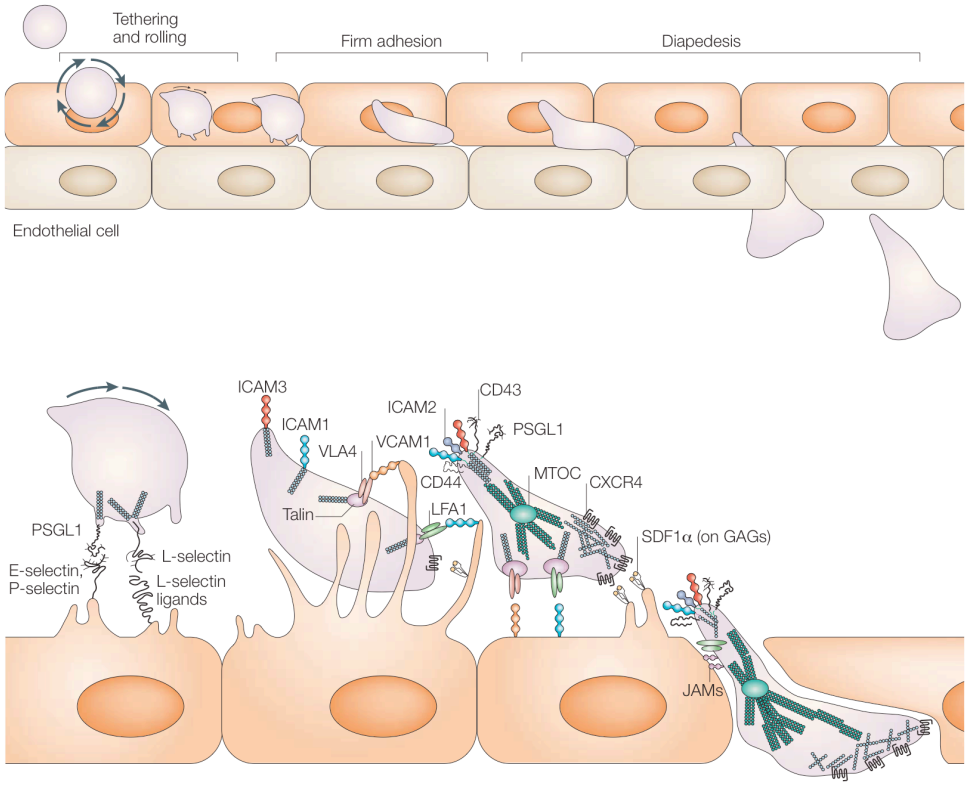

Figure 1-5: T cell extravasation. (Top) Extravasate of T cells across the blood vessel wall to enter the tissue space involves sequential steps of rolling and tethering, activation, adhesion and arrest, and transendothelial migration (diapedesis). (Bottom) T cell tethering and rolling is mediated by selectins and their binding partners on the moving T cell and the endothelium. Binding of chemokines on the endothelium by their receptors on the T cell activates the cell, promoting its firm adhesion and eventually arrest. The arrested cell then undergo diapedesis through the blood vessel wall to enter the tissue space. Illustration from Vicente-Manzanares and Sánchez-Madrid [7].

interact with chemokines both secreted by and displayed on the local endothelial cells. Chemokines are small polypeptides that facilitate leukocyte adhesion, chemotaxis, and extravasation, and can be either constitutively expressed for homeostatic purposes or temporally secreted in response to inflammation. Binding of chemokines by their receptors on T cells activates the cells, raising the affinity and promoting clustering of their surface integrins that results in firm adhesion of the cells to the endothelium. The arrested cells then begin to transmigrate the blood vessel wall to enter the tissue space, a process termed diapedesis (Figure 1-5). This movement is likely mediated by homotypic binding of platelet-endothelial-cell adhesion molecule-1 (PECAM-1) on the T cell with PECAM-1 on the endothelium. PECAM-1 is normally found in an intercellular junction, thus such binding preserves the integrity of the endothelial barrier while permitting cell passage. Once in the tissue, T cells advance via amoeboid movement.

As T cells travel in the circulation to reach their target tissues, they need appropriate mechanical robustness to withstand the forces that their environments exert on them, such as the shear force in the bloodstream, as well as sufficient deformability to adapt to physical barriers, such as the vascular wall that separates the circulation from the tissue space, to continue their movement unimpeded. It has been demonstrated by a large number of studies that the mechanical integrity of a cell affects its mobility [8-12]. Based on these results, the reverse logic is that the migration pattern of a cell may be used to gauge its mechanical characteristics. The differential migration routes of T cells before and after activation expose these cells to varied shear forces due to disparate blood flow rates in distinct lymphoid organs. The dissimilar cellular arrangements present at the sites where

these cells exit the circulation [13] suggest that the two populations likely will not deform the same way upon their egress. These observations lead to the speculation that T cells probably undergo changes in their mechanical properties during the cell activation process.

Despite the extensive literature on the biological and biochemical aspects of T cell behaviors and functions, a much smaller body of work has been conducted to study their mechanical properties. However, this knowledge is important because it not only can provide a better understanding of the T cell migration process, but it may also provide insights to situations where normal migration is disturbed. One case that is specifically examined in this study is the genetic disease Wiskott-Aldrich syndrome (WAS), typically characterized by the triad eczema, thrombocytopaenia, and progressive immunodeficiency [14]. The affected individuals have a mutated WAS gene that either fails to express the WAS protein (WASp) or produces a truncated version of it. WASp participates in signal transduction from membrane receptors of T cells to their actin cytoskeleton and is an important regulator of actin polymerization and branching (Figure 1-6) [15-17]. Reduced cellularity, including thymocytes, T cells, and B cells, was found in all lymphoid organs of WASp-deficient mice [18]. In vivo homing experiments and in vitro chemotaxis assays showed impairment of both processes in T cells from WAS patients and mouse models [19, 20], suggesting that the observed immunodeficiency may arise partly from the cells' inability to migrate normally, possibly as a result of defective regulation of actin. However, it remains unclear how this abnormal migration pattern is translated into physical properties of T cells that govern their locomotion and deformability.

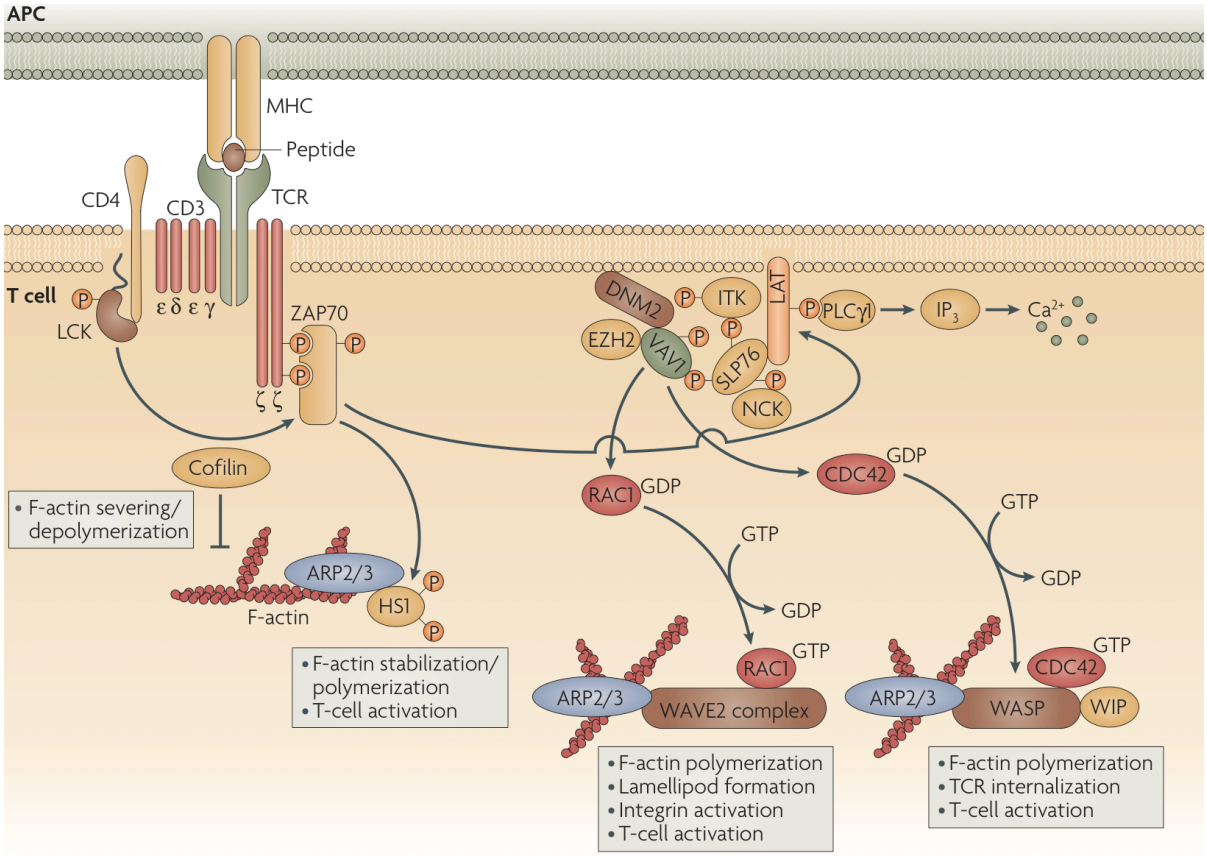

Figure 1-6: Actin polymerization resulting from TCR engagement. Binding of TCR to pMHC leads to activation of the membrane-associated molecules LCK and ZAP70. The activated ZAP70 then phosphorylates LAT, which helps to recruit SLP76. LAT and SLP76 act as a scaffold for actin-regulatory proteins including PLCγ1, NCK, ITK, and VAV1. VAV1 activates CDC42, which in turn activate WASp that polymerizes actin through its association with ARP2/3 and WIP. Actin polymerization can also be regulated through the ARP2/3-WAVE2-RAC1 and the ARP2/3-HS1 pathway. Illustration from Billadeau *et al.* [17].

One of the objectives of this work is to characterize the mechanical behavior of T cells, focusing specifically on their elastic and viscous responses. These two parameters are chosen because they affect the migration of T cells. A stiffer cell (higher elastic modulus) was found to roll faster than a more compliant one [21, 22], while a cell having a more viscous cytoplasm rolls more slowly compared to a cell with a less viscous interior [23]. Also, a treatment that reduced both the stiffness and the viscosity of a cell resulted in a

complete disruption of its tethering to substrates [24]. Investigation of T cell elasticity and viscosity was conducted using two techniques, micropipette aspiration and atomic force microscopy (AFM). Among the numerous methods that are available for studying the mechanical properties of cells [25-29], these two techniques were chosen for their ability to provide the information desired in this case, as well as for their compatibility with non-adherent cells. The elasticity of T cells, in terms of their apparent Young's modulus, was determined via micropipette aspiration. The viscous property of T cells was assessed through AFM cell indentation experiments, in which the variation of the cells' apparent Young's modulus with the indentation rate was examined.

These experimental procedures were applied to T cells from wildtype (WT, not genetically altered) and WASp-deficient (WAS-/-) mice, both in the naïve and the activated state, to test two hypotheses: 1) the elastic and viscous properties of T cells are altered as a result of the cell activation process, and 2) the absence of WASp results in altered elastic and viscous properties in WAS-/- T cells compared to the WT controls. Micropipette aspiration testing was also performed on chemokine-stimulated WT and WAS-/- T cells to investigate whether the defective chemotaxis displayed by the latter might be a result of these cells' having insufficient deformability. Results revealed that the apparent Young's modulus of naive WT T cells substantially decreased when they became activated. WAS-/- T cells were found to be more compliant than WT T cells and activated WAS-/- T cells were found to exhibit an impaired viscous response. Furthermore, even though the activation process also caused a modulus decrease in WAS-/- T cells, the magnitude of reduction was much smaller compared to that of WT T cells. Chemokine exposure drastically reduced the

apparent Young's modulus of naïve WT T cells but had little effect on their WAS-/- counterparts.

Unlike B cells that can directly recognize antigens through their surface immunoglobulins, T cells can only perceive antigenic information and mount immune responses if antigens are processed into short peptides and bound to major histocompatibility complex (MHC) molecules on the surface of antigen-presenting cells (APCs). The two T cell subsets recognize different classes of MHC molecules that present peptides from different sources. Class I MHC (Figure 1-7) [30] is expressed by almost all nucleated cells and presents peptides that are degraded via the cytosolic pathway (Figure 1-8) [31] from proteins produced by the host cell. These peptides can

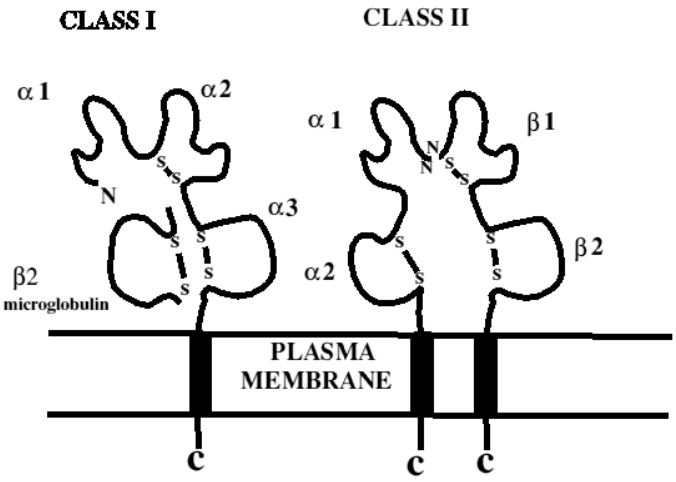

Figure 1-7: Structure of class I (left) and class II (right) MHC complex. Class I MHC consists of a transmembrane α chain noncovalently associated with a β_2-microglubulin. The α chain has three domains, with the α1 and α2 domains forming the peptide-binding cleft. Class II MHC consists of a α chain and a β chain, with each chain having two domains. The α1 and β1 domains act together to bind a peptide. Illustration from reference 30 [30].

come from proteins required for normal cell metabolism and functions, referred to as self-peptides or endogenous peptides, or they can be fragments of viral proteins produced by a virus-infected host cell. Peptide-MHC complexes (pMHC) formed with class I MHC are typically recognized and bound by TCR on CD8-positive T_C cells. Class II MHC (Figure 1-7) is constitutively expressed only on professional APCs, including dendritic cells (DCs), macrophages, and B cells. Class II MHC presents peptides that are components of entities ingested by the APC, enclosed in endosomes, and subsequently transported to the intracellular endocytic pathway to be degraded (Figure 1-8). The pMHC complexes thus generated are recognized and bound by TCR on CD4-positive T_H cells. Class I and II MHC complexes are products of a cluster of tightly linked genes, which in mice is called the H-2 complex [1]. This complex is organized into different regions that encode class I products of the types H-2K, H-2D and H-2L, and class II products of the types IA and IE. MHC genes are polymorphic (many alternative types) and give rise to different MHC haplotypes. For example, a few possible class I H-2K products are H2-K^b, H2-K^d, and H2-K^k.

At the molecular level, T cell activation is a combined effort of various receptors and their ligands. The activation process is triggered when TCR binds to antigenic pMHC, but this process requires the participation of coreceptors and accessory molecules for stabilization and enhancement. A TCR is a transmembrane heterodimer consisted of a α chain and a β chain joined together by a disulfide bond (Figure 1-4). Each chain has an extracellular portion that contains a variable and a constant domain, a transmembrane region, as well as a short cytoplasmic tail. The V_α and V_β domains together form the pMHC

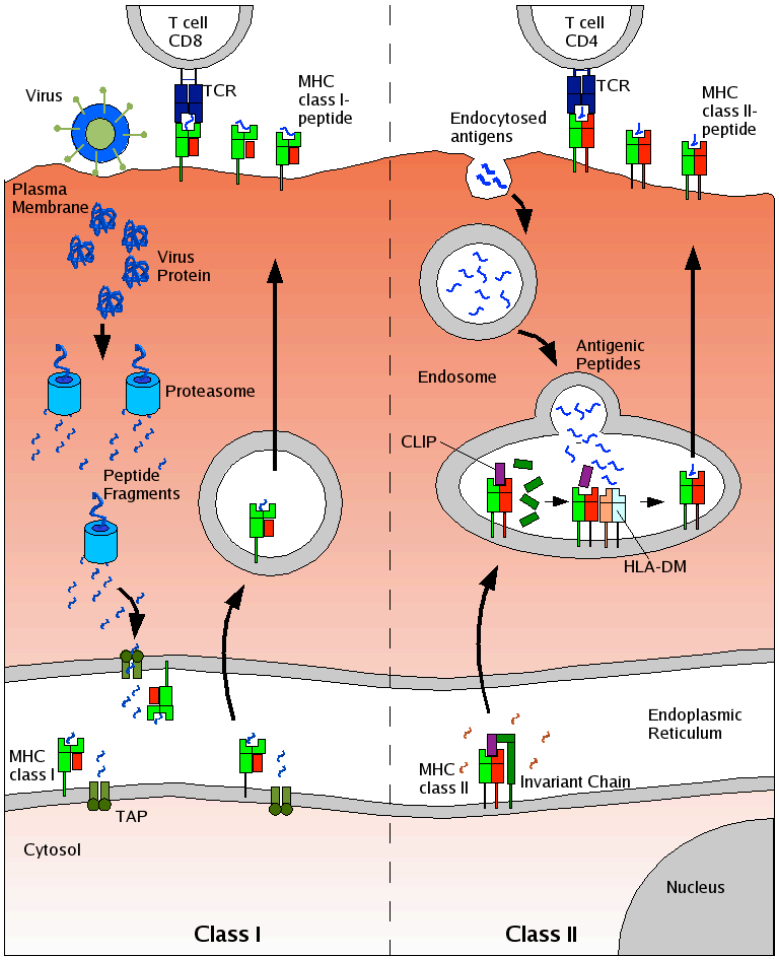

Figure 1-8: MHC antigen presentation. A cell infected by a virus produces viral proteins, which are degraded into peptide through the cytosolic pathway. The viral peptides are bound to class I MHC molecules in the endoplasmic reticulum, and the pMHC complexes are subsequently transported to the surface of the infected host cell, where they can be recognized by $CD8^+$ T_C cells. Antigens that are endocytosed are degraded into peptides via the endocytic pathway. These peptides bind class II MHC molecules, and the resultant pMHC complexes are transported to and inserted into the cell membrane, where they can be recognized by $CD4^+$ T_H cells. Illustration from reference 31 [31].

recognition site. Every TCR is associated with a CD3 complex, a multipeptide structure that transduces signals from the TCR to the cell interior via the immunoreceptor tyrosine-based activation motif (ITAM) in the cytoplasmic tails of the CD3 chains. Class I MHC is structurally different from class II MHC (Figure 1-7). Class I MHC is composed of a

transmembrane α chain that is noncovalently associated with a β_2-microglobulin molecule. The α chain can be subdivided into three domains, the α1 and α2 domains that form the peptide-binding cleft, and the membrane proximal α3 domain. In contrast, class II MHC consists of a α chain and a β chain. Each chain has two domains, with the α1 and β1 domains acting together to bind a peptide. When a TCR complexes a pMHC, the CD4 or CD8 coreceptor on the T cell surface also binds to the same MHC and helps to increase the duration of TCR-pMHC engagement (Figure 1-9) [32]. T cells also have membrane-bound accessory molecules, such as LFA-1, CD28, CD2, and CD45R, that conjugate molecules on APCs and help stabilize TCR-pMHC binding to allow the T cells more time to scan the APC

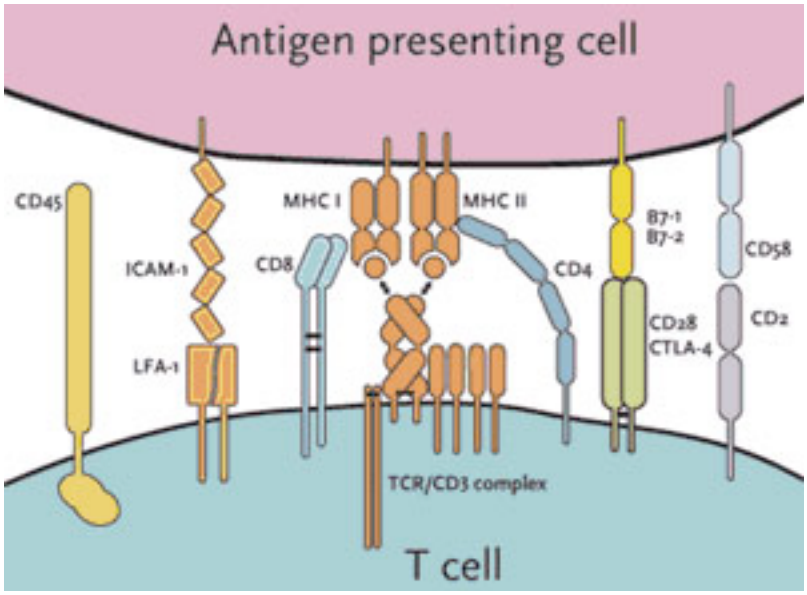

Figure 1-9: Binding of TCR to pMHC. A TCR binds to the peptide and the variable region of a pMHC, while the T cell coreceptor CD8 (T_C cell) or CD4 (T_H cell) binds to the constant region of the same MHC molecule. Accessory molecules on the surface of the T cell and the APC also pair to help stabilize the TCR-pMHC binding. These interacting pairs include LFA-1/ICAM, CD28/B7, CD2/CD58, and CD45R/CD45. Illustration from reference 32 [32].

surface. Engagement of TCR by antigenic pMHC generates an activating signal that induces actin accumulation at the engagement site by bringing the tyrosine kinase Lck associated with the cytoplasmic tail of the CD4 or CD8 coreceptor into proximity of the cytoplasmic tails of the CD3 chains (Figure 1-6) [17]. Lck phosphorylates the ITAMs on the CD3 chains, and the phosphorylated tyrosines in the ITAMs serve as docking sites for the tyrosinekinase ZAP-70, activating it as a result. The activated ZAP-70 then phosphorylates linker for activation of T cells (LAT), which in turn recruits SRC homology-2 (SH2)-domain-containing leukocyte protein of 76 kDa (SLP76). LAT and SLP76 act as a scaffold for various proteins that regulate actin, including PLCγ1, NCK, ITK and VAV1. PLCγ1 helps to increase the calcium level in T cells, which is needed for F-actin remodeling. VAV1 activates CDC42, which in turn activates WASp to allow initiation of actin polymerization through association with ARP2/3 and WIP (WASP-interacting protein).

At the cell level, binding of a T cell to an APC leads to the formation of a structure called an immunological synapse (IS) at the cell-cell interface (Figure 1-10) [33]. This structure consists of concentric circular regions referred to as supramolecular activation complexes (SMACs) where signaling molecules are segregated. The central SMAC on the T cell side is enriched in TCR, CD28, CTLA4, and protein kinase C-θ, one of the downstream signaling effectors of the activation process. The complementary molecules on the APC side are pMHC complex and CD80 or CD86. Surrounding the central SMAC is the peripheral SMAC, which is concentrated with mainly adhesion molecules including LFA-1 interacting with ICAM1 and the cytoskeletal linker talin, but also with CD4/8, CD2 that interacts with

CD48 or CD59, and LCK. The outermost region is the distal SMAC, which contains bulky molecules such as CD43 and CD45.

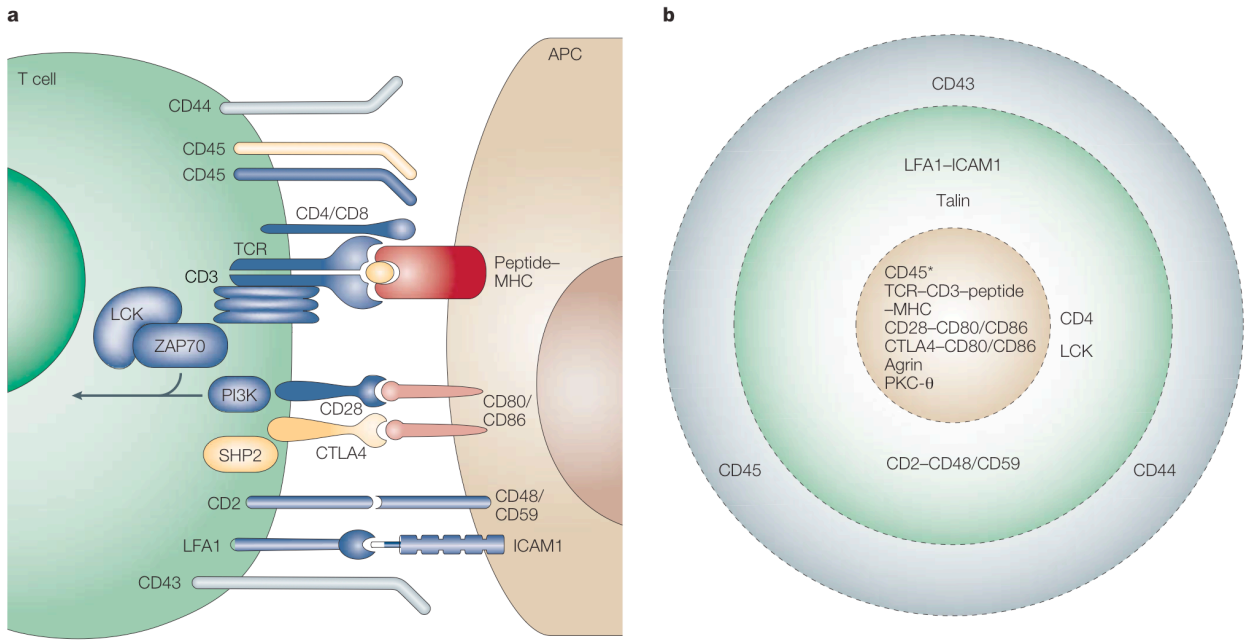

Figure 1-10: Structure of an immunological synapse (IS). A IS is composed of concentric regions of SMACs containing segregated molecular species. The cSMAC is enriched in pairs of TCR/pMHC, CD28/CD80, CTLA4/CD86, and protein kinase C-θ, one of the downstream signaling effectors of the activation process. The pSMAC is concentrated with mainly adhesion molecules including pairs of LFA-1/ICAM-1, as well as the cytoskeletal linker talin and the coreceptor CD4 or CD8. The outermost region is the dSMAC, which contains bulky molecules such as CD43 and CD45. Illustration from Huppa and Davis [33].

The recognition and binding of TCR to pMHC is key in many biological processes of T cells, including their development, activation, and homeostatic maintenance in the periphery [33-35]. Since a critical determinant of immunity depends on whether T cells can be activated to carry out effector functions and combat infections, much effort has been devoted to understanding how TCR engagement by pMHC generates signals for T cell activation and how these signals are transmitted to the T cell interior to induce a biological

response in the T cell. Specifically, it is desirable to determine how these mechanisms accomplish the high specificity and sensitivity that characterize TCR recognition of antigen. Studies showed that the interaction strength between TCR and pMHC governs whether an activating signal would be formed [36-41]. The TCR-pMHC binding strength is conventionally characterized in terms of the affinity between the molecules, K_D, defined as the ratio of the dissociation rate of the conjugate, k_{off}, to the association rate, k_{on} (see Section 3.1 for more detail). Whether the biological outcome induced by a pMHC ligand depends on the K_D [36-38] or the k_{off} [39-41] of the resultant TCR-pMHC conjugate remains a controversial issue that is not completely resolved. Studies supporting the former observed high affinity to correlate with successful activation of a T cell, while evidence for the latter found a long half-life, $t_{1/2}$ ($k_{off} = \ln 2/t_{1/2}$), corresponding to a small dissociation rate, to produce a positive activation outcome. In the latter case, specificity of TCR binding to pMHC is widely explained through the kinetic proofreading model [42], which views the triggering of a TCR to 'fire' a productive signal as a multi-stage process that requires the receptor-ligand pair to stay engaged for a sufficient amount of time. This way, agonist pMHC ligands that stay bound to TCR longer and elicit T cell activation can be distinguished from spMHC ligands that quickly dissociate from TCR and fail to trigger a response.

In the T cell-APC contact region the TCR needs to find rare agonist pMHC complexes among a sea of endogenous pMHC ligands. Despite the scarcity of the former ligand type, both CD4+ and CD8+ T cells were found to be able to detect as few as one agonist ligand [43, 44]. Sustained signaling was seen in the CD4+ population with about ten ligands [43], and target cell lysis could be achieved by CD8+ T cells with stimulation from

only three ligands [44]. Research into this surprisingly high sensitivity revealed that spMHC complexes, in contrast to the previous assumption of not playing a role in antigen detection due to their very weak interactions with TCR, participate in this process by forming pseudodimers with agonist ligands that result in enhancement of signal propagation [45, 46] (see Section 3.1 for more detail). This discovery makes studying the biophysical properties, namely the K_D and the k_{off}, of spMHC complexes important, since signals from these complexes can contribute to T cell activation. Therefore, a thorough understanding of the T cell activation process requires detailed information on TCR-spMHC binding.

Endogenous pMHC ligands also play a critical role in the process of T cell development. Thymocytes are selected for maturation by the spectrum of endogenous pMHC ligands displayed on thymic stromal cells and must integrate all the TCR-spMHC interaction they sense. Those cells that are able to recognize and bind self MHC, but simultaneous do not bind strongly to self pMHC ligands, are retained for development into mature T cells [34]. In the latter process, cells that are allowed to survive are referred to as being positively selected, while those that are deleted are said to be negatively selected [34]. A model called the occupancy model [47-49] has been introduced to explain how avidity (binding strength from multiple TCR-pMHC pairs) of TCR interaction with pMHC at the cell level governs the outcome of thymocyte selection. In this model, a threshold exists to divide positive selection from negative selection, and both high-affinity ligands at low concentrations and low-affinity ligands at high dosage can positively select a thymocyte [50-52] as long as the cumulative signal is below the threshold. This cumulative nature

means that at the selection boundary, a few low-affinity spMHC complexes could nudge a survival signal into a deleting one. This possibility again emphasizes the need to examine and determine the binding parameters of endogenous pMHC ligands.

Even though the K_D and k_{off} values for some TCR-spMHC conjugates have been reported [53-55], measurements involving endogenous ligands tend to be challenging for currently available methods, such as surface plasmon resonance (SPR) [56], since the K_D and k_{off} values in these cases can be beyond the range that these methods can confidently detect. For example, SPR can comfortably measure affinities between 10^{-11} and 10^{-4} M^{-1} [57] but some spMHC complexes can have affinities larger than 300 μM [36, 58]. Observing this limitation, a goal of this work was to explore an alternative technique that could probe very weak molecular binding. Specifically, dynamic force spectroscopy (DFS) [59], a procedure based on atomic force microscopy, was investigated. By measuring the unbinding force of a single pair of receptor and ligand at different unbinding rates and fitting these forces to an appropriate mathematical model, a k_{off} value for the pair can be derived. DFS has been successfully used to characterize the dissociation process of various ligand-receptor systems [59-63], with some of them having K_D values comparable to those of TCR-pMHC interactions [61, 64].

In this study, a DFS procedure was developed to measure the unbinding forces between dimeric 2C TCR or 2C* TCR, a high affinity variant of the former [65], and MHC class I K^b conjugated to two peptides, SIRGL and p2Ca. These two peptide were chosen to represent the two ends of a peptide potency spectrum, with SIRGL inducing strong 2C*

TCR-K^b binding and the self-peptide p2Ca inducing very weak binding between 2C TCR and K^b. Preliminary results suggest successful application of DFS to studying TCR-pMHC interaction, with a k_{off} value derived for both TCR-pMHC combinations. Therefore, this technique demonstrates potential for investigating TCR-pMHC systems with high dissociation rates and may help raise the upper bound of the k_{off} range measurable by currently available methods.

Chapter 2 Characterization of T Cell Mechanical Properties

2.1 Background

The homeostatic operation of the immune system requires T cells to home to distinct lymphoid organs in the body. During this journey, T cells are acted on by a myriad of forces that change their shape and challenge their mechanical integrity. While traveling in the bloodstream, they are sheared by the blood flow. Once tethered, they experience adhesive forces at the anchor sites that oppose the shearing forces. T cell transendothelial migration, called diapedesis, takes place through either the transcellular pathway or the paracellular pathway [66]. The former case requires a T cell to physically penetrate an endothelial cell, while the latter case involves the T cell squeezing through an intercellular junction in the endothelium. In both scenarios, a T cell must undergo substantial mechanical deformation and be able to rapidly recover its original shape. Once in the tissue space, T cells are impacted by objects in their environment. The migration pattern of naïve T cells in a lymph node was proposed [67] and later demonstrated [68] to be a result of the cells physically colliding with obstacles in their pathways. These findings suggest that in order to migrate unimpeded, T cells need mechanical properties that are compatible with their surrounding.

It is known that T cells home to different lymphoid organs before and after cell activation [69]. Naïve T cells selectively enter secondary lymphoid organs (Figure 2-1),

where upon encountering antigens displayed on antigen-presenting cells (APCs), they proliferate and differentiate to acquire effector functions that facilitate the removal of infectious agents. In contrast to their naïve counterparts, activated T cells preferentially target tissues that emit inflammatory signals. T cell homing and extravasation into the appropriate tissues has traditionally been attributed to the interplay between homing receptors on T cells and expression patterns of chemokines and adhesion molecules at the target tissues [13, 69]. However, a study

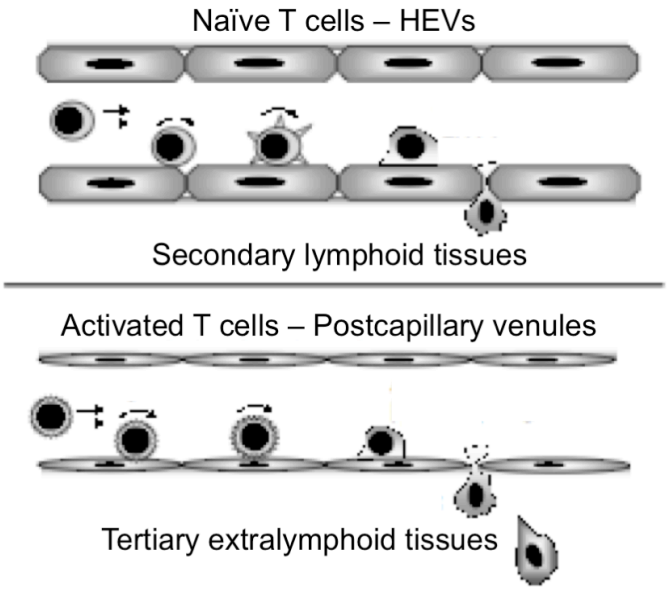

Figure 2-1: Extravasation of naïve (top) and activated (bottom) T cells. Naïve T cells circulate to secondary lymphoid tissues and egress via high endothelial venules (HEVs), while activated T cells travel to tertiary extralymphoid tissues and enter which through postcapillary venules. Endothelial cells at the two exit sites have dissimilar shapes, as depicted above, being cuboidal and flattened at the HEVs and the postcapillary venules, respectively. Despite these differences, both naïve and activated T cells extravasate the vessel wall to enter the tissue space. Illustration from Norman *et al.* [13]

revealed the importance of mechanical stimuli in this process by showing suspension of T cell transmigration upon the removal of the fluid flow in their environment despite the

presence of chemokines [70]. The differential migration routes and target tissues of naïve and activated T cells expose these two populations to varied blood flow rates and thus dissimilar shear forces [2]. In addition, differential cellular arrangements are observed at the sites where the cells exit the circulation (Figure 2-1) [13], suggesting that the two populations may not have the same deformation requirements during the transmigration step. Together, these observations generate the hypothesis that T cells alter their mechanical properties upon activation. This phenomenon has been observed previously in other cell types. Lautenschlager *et al.* showed that differentiated acute promyelocytic leukemia cells were about 45% more compliant than the control [11]. Titushkin *et al.* discovered a reduction in the average Young's modulus from 3.2 kPa to 1.7 kPa as human mesenchymal stem cells differentiated into osteoblasts [27].

Knowledge of the mechanical properties of immune cells and a comparison of this information to that obtained from their diseased counterparts may lead to a better understanding of the pathophysiology of the disease. For example, in leukocyte adhesion deficiency type I and II [71, 72], defective neutrophil adhesion results in poor neutrophil chemotaxis and phagocytosis. The present work specifically examined the rare genetic disease Wiskott-Aldrich syndrome (WAS), clinically characterized by thrombocytopaenia, eczema, and progressive immunodeficiency [14]. The affected individuals have a mutated WAS gene, whose product, the WAS protein (WASp), has been shown to participate in signal transduction from cell membrane receptors to the actin cytoskeleton (Figure 1-6) [15, 73]. Although the biological and biochemical aspects of WAS is well documented, the mechanism behind the clinically observed immunodeficiency is not well understood.

Reduced cellularity, including thymocytes, T cells, and B cells, was observed in all lymphoid organs of WAS-/- mice [18]. Examination of this phenomenon identified impaired T cell development, with hindered progression of thymocytes from the $CD4^-CD8^-$ double-negative stage to the $CD4^+CD8^+$ double-positive stage. This result led to the proposal that a reduced output of mature immune cells may partly account for the pathogenesis behind the immunodeficiency. Studies focusing on the migration of WASp-deficient immune cells uncovered that T cells, macrophages, monocytes, neutrophils, and dendritic cells from WAS patients exhibited either impaired chemotaxis in vitro, impaired homing in vivo, or both [19, 20, 74-78]. These findings suggest that defective migration may also contribute to the WAS-specific immunodeficiency. Since the expressions of adhesion molecules (L-selectin, E-selectin ligand, LFA-1, $\alpha 4$ and $\beta 7$ integrins, CD43, and CD44) [19, 20] and chemokine receptors [20] appeared normal on WAS-/- T cells, the impaired migration does not seem to stem from deficiency of these molecules. Inspection of the extravasation capability of WAS-/- T cells showed normal rolling and tethering [19, 20], although the latter seemed to be ligand-dependent. This outcome suggests that diapedesis may be the step most affected by the WAS disease.

Despite the substantial information available on the biological and biochemical aspects of T cell migration, few studies have specifically investigated their mechanical properties, even though their deformability critically affects the success of their migration. Among these works, numerical results are scarce. However, quantitative characterization is useful because it allows a systematic comparison of T cell deformability under different

conditions, such as alterations that arise as a result of diseases. An application of such comparison may be evaluation of the efficacy of potential drugs or therapies.

Attempting to better understand the rheological properties of leukocytes, Schmid-Schonbein *et al.* applied a step pressure to them using the micropipette aspiration technique and observed how cell displacement varied with time (ie, creep response) [79]. They mathematically modeled these cells as homogeneous viscoelastic solid spheres and found the mechanical responses of the cells accurately described by the standard solid model [79]. Using this model, K_1, K_2 and μ were determined to be 275 dyn/cm^2, 737 dyn/cm^2, and 130 dyn-sec/cm^2. Aspiration at different locations of a cell generated similar deformation history, which suggests relatively homogeneous elastic properties of the cell on the scale of micropipette testing. Pasternak and Elson used a cell poker to investigate changes in the deformability of B lymphocytes after their surface proteins had been cross-linked by Concanavalin A (ConA) or anti-lgM antibodies [80]. Lymphocytes roughly 6 μm in diameter were compressed about 1 μm with a poker about 4 μm in diameter. Stiffening of the cells resulted from the treatment, with a stiffness (amount of increase in compressive force with respect to cell displacement) increase from ~0.15 mdyne/μm to respectively ~0.4 and ~0.6 mdyne/μm for ConA- and antibody-treated cells. This increase could be variably reversed by cytochalasin D and colchicine that respectively interferes with the function of actin microfilaments and microtubules, indicating that the observed stiffening is mediated by the cell cytoskeleton. Since lymphocytes have a thin cytoplasm around the nucleus, it was proposed that the observed stiffness was dominated by the response of the cytoskeletal cortex that lies immediately beneath the cell membrane. More recently, Wu *et*

al. used AFM to probe the adhesion force of T lymphocytes as a result of cell activation and discovered that the force decreased upon activation, reducing from roughly 600 pN to about 400 pN 48 hours after the activation procedure started [81]. Cai and coworkers performed cell indentation on lymphocytes and Jurkat cells using AFM to probe their stiffness and determined an average elastic modulus of 1.24 +/- 0.09 and 0.51 +/- 0.06 kPa for the two cell types, respectively [82]. The higher stiffness of lymphocytes was attributed to their possessing more abundant and thicker actin bundles, as revealed in confocal microscopy images. Treatment of the cells with the actin-disrupting agent cytochalasin B destabilized the actin structure in both cell types, reducing their elastic modulus to 0.34 +/- 0.04 and 0.23 +/- 0.04 kPa, respectively, for lymphocytes and Jurkat cells.

Other members of the leukocyte family are also poorly characterized in terms of their mechanical characteristics except neutrophils. However, despite being both in this family, T cells and neutrophils have substantially different nucleus to cytoplasm ratios that likely confer them with dissimilar mechanical characteristics. Nevertheless, findings from neutrophil studies may still help gauge and predict the same properties in T cells. It has been established that a neutrophil is best described as a viscous liquid drop enveloped in a membrane with constant cortical tension that helps maintain the spherical shape of the cell [83, 84]. This cortical tension is mediated by the actin cytoskeleton, as exposure to the actin-disrutping agent cytochalasin B reduced its value [85]. Evens and Young modeled a neutrophil as a Newtonian liquid drop surrounded by a membrane of constant cortical tension and measured a value of 0.035 mN/m and 200 Pa·s for the neutrophil cortical tension and cytoplasmic viscosity, respectively [84]. This result is comparable to the 0.024

mN/m determined in a similar study by Needham and Hochmuth [86]. However, the latter study unveiled a cytoplasmic viscosity of 135 Pa·s [86], much smaller than that reported by Evans and Young. This discrepancy was attributed to the larger aspiration pressure used in the latter case, leading to the proposal that the neutrophil cytoplasm behaves like a power law fluid [87], exhibiting decreasing viscosity with increasing deformation rate. Neutrophil viscosity appears to depend on the magnitude of deformation as well, with larger cellular viscosity values obtained from cells that had been deformed by a micropipette to a greater extent [88, 89]. Further probing of the membrane of neutrophils revealed its possession of an area expansion modulus about 0.04 mN/m, based on a series of experiments aspirating neutrophils into a micropipette to various equilibrium positions (cell length inside micropipette). The bending stiffness of the neutrophil plasma membrane, conferred by the underlying cortex estimated at 0.24 μm thick, was found to be 1 to 2 × 10^{-18} J [90]. Compared to the red blood cell, the neutrophil has a bending modulus that is 5-50 times higher, indicating the reduced capacity of the latter to deform. Since both the Newtoninan liquid drop model and the power law fluid model do not account for all features of the mechanical behaviors of neutrophils, other more complex models have been proposed to capture more of these features. These models have been reviewed by Lim *et al.* [91].

Despite the paucity of quantitative knowledge on T cell mechanical responses, a body of literature on the contributions of the different cytoskeletal components to the deformability of leukocytes provides valuable qualitative information on T cell biomechanical behaviors. The motility and deformability of a cell is governed by its cytoskeletal components - actin microfilaments, microtubules, and intermediate filaments.

Actin microfilaments regulate the morphology and motility of leukocytes by undergoing dynamic contraction and relaxation that together with motor proteins such as myosin, generate mechanical forces required for membrane protrusion during cell movement [92, 93]. Reconstituted actin networks demonstrated the highest rigidity among the three components but fluidized at high strains, thereby allowing a cell to rapidly extend and retract actin filaments during migration [94]. The ability of a leukocyte to transit a constriction and the entry rate appear to depend on the rearrangement of actin [95, 96], but the subsequent cell recovery seems independent of it [96]. Various capping proteins, nucleator proteins, and adaptor proteins, regulate the polymerization and depolarization of actin filaments to allow speedy formation and breakdown of actin-based structures [7]. In leukocytes, actin regulatory genes include WAS, WIP, Vav1, Rac1, Rac2, and RhoA. Defects in these genes can lead to deficient T cell activation, inappropriate adhesiveness, and impaired migration and phagocytosis [7].

While the forward motion of leukocytes relies on the extension of actin filaments, the retraction of the cell rear end requires the collaboration of actin and myosin. Jacobelli *et al.* discovered that T cells could adopt two modes of motility - a fast amoeboid-like mode that relies on sequential, discontinuous contacts with the substrate, as well as a slower mode that involves a single continuously translating adhesion [10]. Myosin-IIA, the only form of myosin expressed in T cells [97], was found to participate in the fast mode by generating repetitive compressions in the rear end of a migrating cell that eliminated existing adhesive contacts while new contacts were forming in the front end [10]. Therefore, by regulating myosin-IIA, the contact area between a T cell and its substrate and

the cell's crawling velocity could potentially be modulated. Myosin-IIA was also found to be essential for maintaining the uropod structure of a motile T cell but unnecessary for immunological synapse formation [97].

Microtubules do not seem to have a significant mechanical function in leukocytes. Instead, they principally mediate cell division and participate in motor protein-based intracellular cargo transport [7]. Microtubules normally radiate outward from microtubule organizing centers (MTOCs) and surround the nucleus of a non-polarized T cell [98]. When T cells polarize in preparation for their imminent migration, microtubules undergo a dramatic rearrangement and collapse into a compact sheath. The MTOCs subsequently retract to the lumen of the cell uropod [7, 98]. Administration of microtubule inhibitors showed that the retracted microtubules were unnecessary to support uropod formation or to generate motive force. This result suggests that the retraction process may be a strategy to allow fast increase in cell deformability during T cell extravasation without disassembling the microtubule-based transport system.

Intermediate filaments generally confer structural support to a cell [99]. They are usually vimentin in leukocytes and are implicated in the rigidity and structural integrity of lymphocytes during extravasation [100, 101]. Reconstituted vimentin networks were found to be compliant (low shear modulus) at low strains but harden at high strains to resist breakage [94], a behavior opposite of that of actin filaments. Therefore, these two cytoskeletal components complement each other and generate a range of mechanical properties in leukocytes. One study showed a reduced capacity to home, as well as an

abnormal pattern of surface molecules critical for homing, in lymphocytes lacking the intermediate filament vimentin [102]. Further examination unveiled that the disrupted homing might stem from defective adhesion, as vimentin was needed to form a highly dynamic anchoring structure at the contact site of a lymphocyte and an endothelial cell [102].

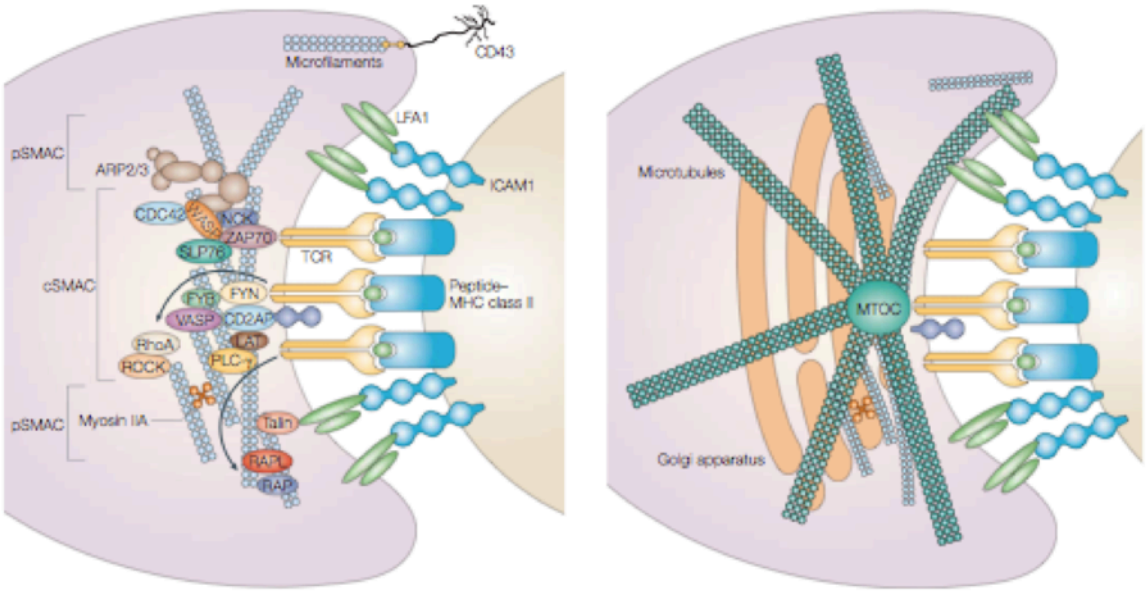

Figure 2-2: Arrangement of actin microfilaments and microtubles at the site of TCR ligation. (Left) Actin polarizes and polymerizes at the site to form a platform that helps recruit cell activation signaling molecules and faciliates their interactions. (Right) The MTOC also translocates to the TCR engagement site to form a delivery system that traffics granules to be secreted to the T cell-APC interface. Illustration from Vicente-Manzanares and Sánchez-Madrid [34].

A hypothesis that this work aimed to test is that the activation process of T cells changes their mechanical properties as means to accomodate the different forces and physical barriers that activated T cells may encounter while traversing their new migration route. This alteration in the cells' deformability is suggested by the substantial cytoskeletal

reorganization in naïve T cells upon recognition of antigenic pMHC presented on APCs. TCR ligation induces reorganization and polarization of the actin microfilaments to a location below the immunological synapse (IS) [17, 80, 103] (Figure 2-2), which helps to recruit essential kinases and molecular species involved in actin polymerization to the engagement site [104]. WASp is also recruited to the site, where it interacts with the ARP2/3 complex to regulate the polymerization and branching of actin [104]. Surface molecules on the interacting T cell and APC undergo actin-dependent redistribution and form supramolecular activation clusters that together compose an IS. The cell activation process also translocates microtubule-organizing centers (MTOCs) from the rear of the T cell to the IS to facilitate construction of a delivery system to traffic granules to be secreted to the interface [105-107] (Figure 2-3). Binding of TCR to cognate pMHC triggers LFA-1 (leukocyte function-associated antigen 1) -dependent adhesion, helping to stabilize the T cell-APC conjugate, while T cells extend actin-rich, exploratory protrusions to scan the surface of APCs [103, 108]. Faure discovered rapid inactivation of the ezrin-radixin-moesin (ERM) family proteins upon TCR ligation [109], resulting in the release of anchors that normally bind the cell plasma membrane to the underlying cortical actin cytoskeleton. This leads to increased membrane fluidity that allows a larger contact area to form between a T cell and a APC, thereby promoting more efficient antigen recognition by the former.

Cell migration is paramount in many biological processes, such as tissue formation during development and lymphocyte recirculation for immunosurveillance. Dynamic rearrangements of the leukocyte cytoskeleton durig migration have been qualitatively examined and may help identify possible causes underlying the impaired

migration exhibited by WAS-/- T cells. Leukocytes traveling in the blood are spherical in shape and display a high density of microvilli supported by parallel actin bundles that are anchored to the cortical actin network [109, 110] (Figure 2-3). These microvilli are enriched with adhesion molecules that participate in the initial adhesion and deceleration of leukocytes in the bloodstream during extravasation. Leukocytes rolling proximally to the vascular endothelium are activated by the chemoattractants displayed on the endothelial

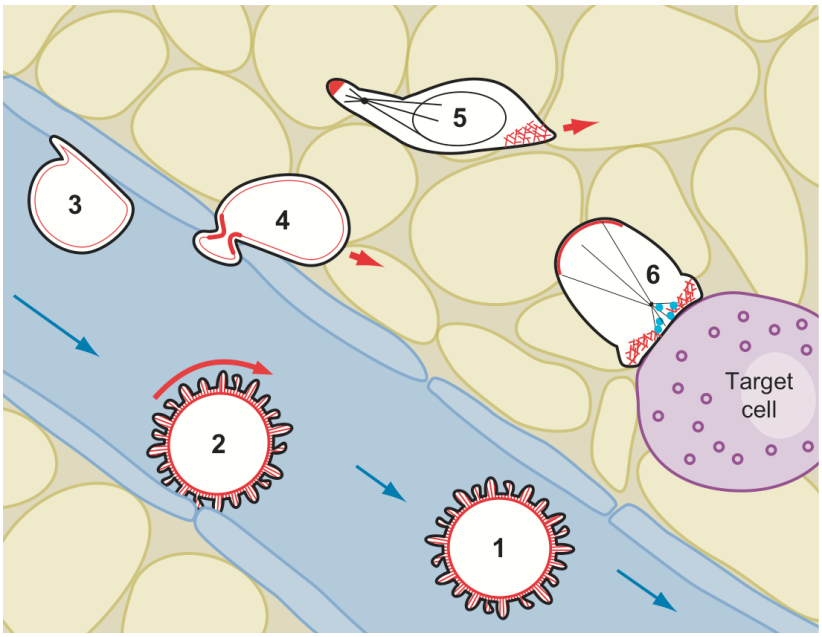

Figure 2-3: Actin rearrangement during leukocyte migration. Circulating T cells (1) display actin-rich microvilli whose tips are enriched in adhesion molecules that facilitate leukocyte tethering and rolling (2) on the vascular endothelium. Chemokine stimulation triggers the collapse of the microvilli (3) and results in tight adhesion of the cell to the endothelium mediated by high-affinity integrins on the chemokine-activated cell. Chemokine exposure also polarizes the leukocyte, which subsequently initiates transendothelial migration (4). Once in the tissue space, the cell advances via amoeboid movement, extending an actin-rich lamellapodium at the leading edge while retracting the uropod at the rear end (5). Recognition of a target cell induces the formation of a IS at the cell-cell interface. Both actin filaments and MTOCs polarize to a location below the IS, where they help redistribute cell surface molecules and traffic granules in the leukocyte to the interface (6). A distal pole opposite of the IS contains an actin network that aids sequestration of unused surface molecules. Illustration from Burkhardt *et al.* [109]

cells, which cause a collapse of the surface microvilli [109, 111]. This process consequently exposes the chemokine receptors and adhesion molecules modulating the later cell attachment and movement that are normally sequestered to pits on the leukocyte surface [109]. In response to the local adhesion molecules and apical chemokines, leukocytes flatten in shape [109, 112] by reorganizing their actin structure and undergoing polarization, resulting in redistribution of surface receptors, adhesion molecules, and intracellular signaling molecules [113] (Figure 2-3). A polarized leukocyte exhibits protrusive filopodia at the leading edge [114, 115]. These filopodia are concentrated with the adhesion receptor LFA1 that interacts with intercellular adhesion molecule 1 (ICAM1) displayed on endothelial cells to facilitate the crawling of leukocyte to search for potential transepithelial migration sites [116, 117]. Interaction with leukocyte filopodia induces in endothelial cells development of membrane protrusions that are shaped like docking structures for the filopodia [118, 119]. Fluid shear stress was shown to be essential for leukocyte diapedesis [70, 120] and promotes this process by stimulating the formation of membrane protrusions [121] that can grow into actin-rich lamellipodia (Figure 2-4), which are capable of exerting a force to break down an endothelial cell junction [122]. A polarized leukocyte also possesses a uropod in the trailing end that contains most of its cytoplasm, into which both the microtubule and intermediate filament networks are retracted during migration [7]. The uropod is enriched in adhesion molecules, such as ICAMs, CD43, CD44 and PSGL1. This molecular aggregation is actively maintained by ERM proteins [7] and may be a mechanism that leukocytes use to store unused molecules during migration while allowing quick mobilization of these molecules when they are needed for effector functions.

Once in the tissue space, leukocytes adopt amoeboid movement [123] and rely on chemokines and lipid mediators to maintain their directed movement and motility [124].

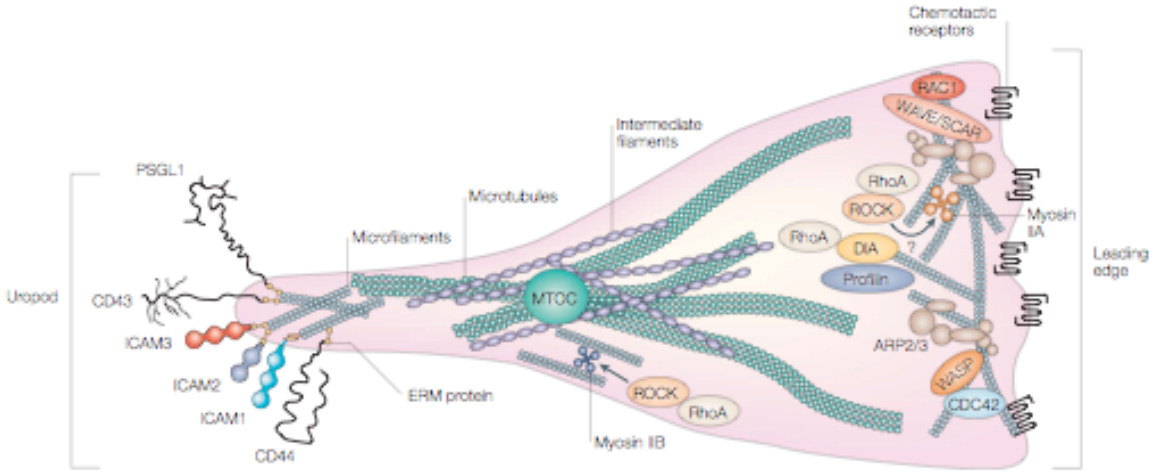

Figure 2-4: Cytostructure of a migrating leukocyte. A chemokine-stimulated leukocyte migrates by extending an actin-rich lamellipodium in the leading edge and contracting an uropod in the rear end. Actin polymerization in the leading edge is regulated by multiple pathways, such as the CDC42–WASP–ARP2/3, RAC–WAVE–ARP2/3 and RhoA–DIA1 pathways. Myosin IIA in the cell anterior can cross-link actin and help expand and shrink the actin network through the regulation of RhoA. The uropod contains the retracted MTOCs and intermediate filaments. Actin mediates the clustering of adhesion molecules, such as ICAMs, CD43, CD44, and PSGL1, through ERM proteins that link the intracellular domains of these molecules to the actin cytoskeleton. Illustration from Vicente-Manzanares and Sánchez-Madrid [7].

Chemokines are indispensible for lymphocyte homing, guiding the different lymphocyte subsets to extravasate into appropriate lymphoid tissues and directing them to appropriate compartments within these tissues (e.g. inflammatory sites, sites enriched with APCs) [125]. Chemokines also contribute to the development of T cells by promoting the movement of cells in different developmental stages to proper regions in the thymus [126-128], such as the transport of thymocytes of increasing maturity from the thymic

cortex to the medulla, and the egress of thymocytes that survive both positive and negative selection from the thymus into the circulation [128]. Studies conducted by Foxman on the chemotaxis of neutrophils revealed that these cells integrated multiple competing chemoattractant stimuli by undergoing chemotaxis in the direction of the vector sum of the signals [129]. Chemotactic stimulus from an agonist source, such as a phagocytic target, was prioritized over the more general chemotactic signals that recruit cells into tissues [129, 130]. Moreover, these cells appeared to 'remember' their recent chemical environment and prioritize the chemoattractant signals they received based on the chronological receipt of the signals, with the newest ones predominating the direction of cell migration [129].

The mechanical behaviors of cells can be studied using a variety of methods, including micropipette aspiration, atomic force microscopy (AFM), optical tweezers, magnetic twisting cytometry, microplates, and the cell poker [131-136]. Most of these methods have not been applied to T cells. However, from the point of view of instrument capabilities, AFM and micropipette aspiration are probably the most suitable choices for investigating the mechanical properties of T cells. An AFM allows the measurement of sub-nanometer displacements and forces from a few picoNewtons (10^{-12}) up to the microNewton (10^{-6}) range [137]. It has been used to determine the stiffness, viscosity, and adhesion force of a cell [81, 82, 132]. Depending on the size of the AFM probe, localized or global cellular characteristics can be revealed. Direct application of this technique to non-adherent cells is not straightforward since they tend to escape from underneath an AFM probe. However, this problem has been overcome by trapping the cells using physical

structures including microwell arrays [138] and porous membranes [139, 140]. One drawback of a typical AFM setup is the inability to view the cell subject from the side, thus providing only a ventral view of cellular changes during testing. This deficiency can be compensated by the micropipette aspiration technique, which utilizes transparent micropipettes that allow real-time viewing of cellular changes in the longitudinal direction (along the micropipette). Micropipette aspiration is traditionally used to study the biomechanics of neutrophils but has been more recently applied to adherent cell types [141, 142]. This method is ideal for investigating cells that do not need adhesion for survival, such as neutrophils and erythrocytes. Depending on the portion of a cell aspirated, membrane properties such as the apparent membrane tension, or whole-cell responses such as the cell elastic modulus and cytoplasmic viscosity, can be evaluated [84, 88, 89, 143]. The cell poker and microplates may also be used to study T cell mechanics, but both techniques require the cell subject to firmly adhere to the substrate, as the former probes the cell inverted and the latter pushes or pulls on the cell during testing [135, 136]. Cell adhesives may be used to immobilize the cell subject, but the attachment can change the natural morphology of the cell and thus may already alter its mechanical properties [144] before the actual testing begins. Optical traps and magnetic twisting cytometry can offer a sub-picoNewton force resolution and are especially suited for systems that involve minute forces [145]. The former has been applied to deform erythrocytes [146, 147], although the force magnitude can be too small to cause large-scale deformation in nucleated cells, while the latter cannot induce whole-cell deformation but creates local deformation that allows the property of the cell membrane to be assessed [145, 148].

In this work, two important mechanical properties of T cells were investigated - elasticity and viscosity. These two parameters were chosen for their intimate involvement in the migration of non-adherent cells. Cell stiffness was found to affect the rolling of leukocytes, with those stiffened by formaldehyde [149] and softened by cytochalasins [150] moving faster and slower, respectively, than the control. A simulation experiment showed that cell deformability affected both the tethering and the rolling of leukocytes in shear flow [151]. The viscosity of a cell also affects these processes. At the same fluid shear rate, a cell with a highly viscous cytoplasm dissipates more energy and thus rolls more slowly than a cell with a lower cytoplasmic viscosity [152]. Neutrophils treated with cytochalasin B that reduces the prestress in the cortical cytoskeleton and the intracellular viscosity of leukocytes [153] showed a complete disruption of tethering to E- and P-selectin coated surfaces.

The hypothesis that the cell activation process alters the elastic and viscous properties of T cells was systematically tested in this work. The apparent Young's modulus of T cells before and after activation was determined using micropipette aspiration to assess their elasticity. To gauge the viscous property of T cells, AFM cell indentation experiments were conducted at different indentation rates to yield a corresponding apparent Young's modulus, and the variation of this modulus with the rate was examined. The same experimental procedures were repeated for T cells obtained from WAS-/- mice to investigate whether the absence of the WAS protein resulted in altered elastic and viscous properties, and if so, how they compared with values from wildtype (WT, not genetically altered) T cells. Because WAS-/- T cells show impaired chemotaxis, it was desirable to

understand whether this behavior might be linked to the cells' change in deformability. To do so, both WT and WAS-/- T cells were induced to migrate by a chemoattractant, and the migrated cells were subsequently probed using micropipette aspiration to reveal their elastic property. Results from these experiments showed a more than two folds reduction in the apparent Young's modulus in WT T cells upon activation. The viscous resistance to deformation increased steadily for both naïve and activated WT T cells but abruptly rose for the former at high indentation speeds. Compared to their WT counterparts, naïve WAS-/- T cells were approximately 53% more compliant, but activated WT and WAS-/- T cells exhibited a similar stiffness. Viscosity studies revealed an impaired viscous response in activated WAS-/- T cells compared to WT T cells, which suggests that the components and/or pathways regulating cellular viscosity may be deficient or defective in the former.

2.2 Methods

2.2.1 Cell Sample Preparation

Naïve T Cell Preparation

Cells were harvested from the peripheral lymph nodes and the spleen of Balb/c mice. After red blood cells were lysed, the cell suspension was subjected to a CD8+ T cell enrichment procedure using an EasySep Mouse CD8+ T Cell Enrichment Kit from STEMCELL Technologies (British Columbia, Canada), following the manufacturer's protocol. Post-

enrichment cells were washed twice, each time with 10 mL PBS containing 10% FBS and 1% HEPES to remove debris, and finally stored at 4°C until usage. The purity of the post-enrichment cells was determined using fluorescence-activated cell sorting (FACS). This was done by exchanging approximately $5x10^5$ cells into the FACS buffer (PBS with 2% FBS and 1% Pen/Strep) and double-staining them with mono-clonal FITC-conjugated anti-Thy1 and PE-conjugated anti-CD8α antibodies for 10 minutes at room temperature, protected from light with aluminum foil. The control was pre-enrichment cells, which were stained parallel with the sample. After washing once with FACS buffer, the stained cells were resuspended in 100 μL FACS buffer containing PI and immediately analyzed using FACS. FACS plots were inspected using the software FlowJo by first gating on cells with low PI staining, then gating on cells stained high for both Thy1 and CD8α expression.

Activated T Cell Preparation

T cells were activated in 6-well plates. Anti-CD3 antibody was diluted to a final concentration of 50 mg/mL in sterile PBS, 3 mL of this solution was added to each well, and the plates were placed in a 37°C cell-culture incubator and incubated for 2 hours. Afterward, each well was washed 3 times with sterile PBS and seeded with 1.5 x 10^6 post-enrichment T cells in 3 mL of a T cell activation medium, which consisted of RPMI with 10% FBS, 10mM HEPES (1M), 1% NEAA, 1% sodium pyruvate (100 mM), 50μM β-mercaptoethanol, 4mM L-glutamine, and 100μg/mL Pen/Strep. The activation medium was also supplemented with 100 units/mL IL-2 and 5 μg/mL anti-CD28 anti-body. Cells were activated in a 37°C cell-culture incubator and their activation was determined using FACS.

Cells were processed following the same procedure described above except now the cells were also stained with monoclonal APC-conjugated anti-CD25 antibodies, in addition to the antibodies against Thy1 and CD8α chain. The control was inactivated, post-enrichment T cells obtained as described above. The activated T cell population was identified by first gating on FACS plots cells with low PI staining, then gating on cells stained high for both Thy1 and CD8α expression, and finally gating on cells stained high for CD25 expression.

2.2.2 Micropipette Aspiration System

Synthesis of Micropipettes

Borosilicate glass tubes were melted at their midpoints and immediately pulled into micropipettes using a micropipette puller. The resultant micropipettes were trimmed using a microforge to an inner diameter that was appropriate for the cell subject. This was done by examining the tapered portion of a micropipette under the microforge with a 20x objective lens and aligning it with the built-in ruler to estimate its inner diameter. A heated glass bead that was part of the microforge was then brought into contact with the micropipette at the point of the desired inner diameter to truncate it. Since naïve and activated T cells are roughly 7-9 and 11-13 μm, respectively, different pipette sizes had to be manufactured to test them. The resultant inner diameter ranges used for naïve and activated cells were 2.5-4 μm and 4-5.5 μm in that order.

Synthesis of Cell Sample Holders

Four sheets of 30 mm x 30 mm parafilm were stacked and cut into four stakes of smaller squares with scissors. The smaller squares were stacked, and a U-shaped spacer was cut out from them. The spacer was then laid on top of a 24 mm x 60 mm glass coverslip before a 22 mm x 22 mm glass coverslip was lightly pressed against it. The resultant assembly is a U-shaped chamber in which T cells to be tested were contained. The assembly was transferred to a 80^{o}C oven and incubated for two hours to enhance sealing of the parafilm spacer against the glass surfaces.

The Micropipette Aspiration Device

The micropipette aspiration setup used is a home-built device. A micropipette was inserted into a micromanipulator arm, which provided the micropipette movement in x-, y-, and z-direction. The tapered part of the micropipette was inserted into a sample chamber, while the base of the micropipette was connected to a water column that provided a pressure differential between the interior of the pipette and the sample chamber to aspirate a cell (Figure 2-5). The pressure differential was tailored by adjusting the fluid level in the water column, and this could be achieved through either manually withdrawing water from tubing that connected the water column to a reservoir inside a 50 mL syringe, or withdrawing water from the tubing connecting the water column to an automated syringe pump. Valves were used to switch between the two pathways. The sample holder sat on a Carl Zeiss inverted microscope, and cells were viewed with a 120x oil-immersion objective

lens in bright field. The rate at which fluid was removed ('aspiration rate') as well as the total volume removed ('aspiration volume') by the syringe pump fixed the aspiration pressure exerted on the cell. Cell advancement during an experiment was recorded with a CCD camera that was connected to the base of the microscope.

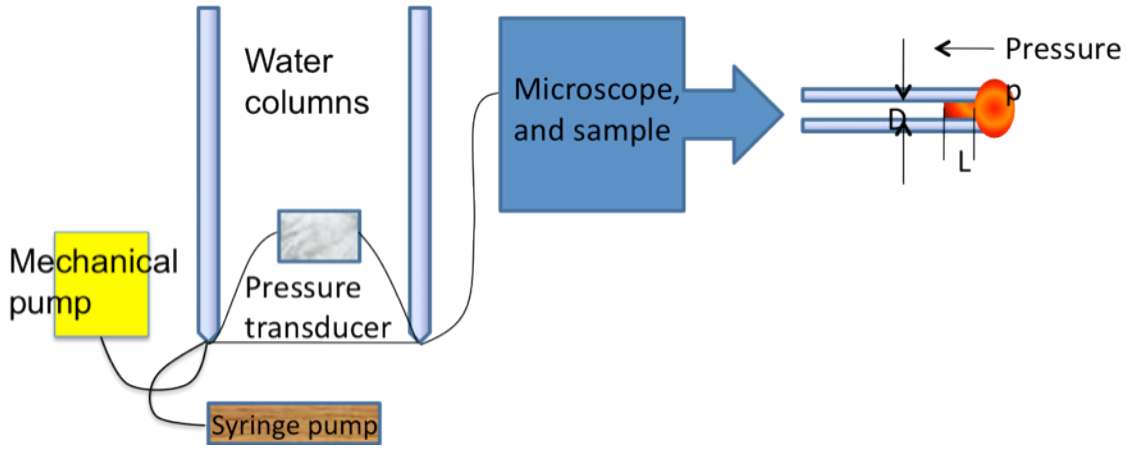

Figure 2-5: Schematic of the micropipette aspiration device. The micropipette is connected to a water column, whose fluid level can be modulated both manually or by a syringe pump to create a negative pressure inside the micropipette to aspirate a cell.

2.2.3 AFM System

Synthesis of Microwell Array Masters and Templates

A mask containing 10 mm x 10 mm dies with the desired microwell array pattern was used to create masters of the microwell array on 4" silicon wafers following the steps outlined below:

1) Spin-coated 5 mL of SU8-5 photoresist onto 4" silicon wafers at 3,000 rpm for 30 seconds

2) Baked the coated wafers for 5 minutes on a 95^{o}C hotplate

3) Transferred the wafers to a 65^{o}C hotplate and baked for roughly 30 seconds

4) Transferred the microwell array pattern from the mask to the treated wafers using a mask aligner (Karl Suss, Model MJB-3). This was done by exposing the wafers to the UV light source for 80 seconds

5) Baked the exposed wafers for 1 minute on a 65^{o}C hotplate

6) Transferred the wafers to a 95^{o}C hotplate and baked for 3 minutes

7) Developed the microwell array pattern by squirting acetate onto the wafers in a circular motion, letting the acetate sit for roughly 1 minute, then spin-washed the wafers for 30 seconds with acetate

8) Baked the wafers for 5 minutes on a 150^{o}C hotplate, then 1 minute on a 95^{o}C hotplate, and finally 1 minute on a 65^{o}C hotplate

The height of the resultant microwell array structure on the silicon masters was measured to be approximately 4.3 μm using a Dektak.

Microwell array templates, which contained the inverse pattern of the actual array (that is, posts on a template become wells on the final array), were made of polydimethylsiloxane (PDMS). Masters of the arrays had to be silanized first before they were used to generate templates. This was done by placing the masters in a dessicator, together with an uncovered petri dish containing 3 drops of trichlorosilane from a

disposable dropper. The vacuum source connected to the dessi-cator was turned on, and the wafers were silanized overnight. A PDMS solution was prepared from a kit. The solution was made by combining a base and a crosslinker at a 10:1 weight ratio. After mixing vigorously and thoroughly, the solution was degassed in a dessicator for roughly 30 minutes to remove air bubbles trapped in it. The degassed mixture was then carefully poured onto silanized wafers that were taped to the inside of large petri dishes to minimize air bubble formation. Any bubbles formed were later removed using a needle. This assembly was carefully transferred to a 80^{o}C oven and baked for at least 2 hours. The crosslinked PDMS was then allowed to cool down to room temperature before it was cut out from the petri dishes using a scalpal. The microwell array features on the PDMS templates were examined under a microscope to ensure fidelity of the pattern transfer.

Synthesis of Microwell Arrays

Glass discs were briefly cleaned with a Kimwipe to remove dust particles, placed in a plasma cleaner and cleaned for 5 minutes, then transferred to beakers containing a bath of a 3-(trimethoxysilyl) propyl methacrylate (Sigma) solution. This solution was prepared by first adding 600 μL of 3-(trimethoxysilyl) propyl methacrylate to 20 mL ethanol, then adding to this mixture 100 μL of 1% glacial acetic acid in PBS immediately before disc immersion. 3-(trimethoxysilyl) propyl methacrylate served as an adhesion promoter that helped bind the glass to the body of the microwell array, which was made of a polymer. The discs were treated for 5 minutes at room temperature and subsequently washed 3 times with ethanol, dried with nitrogen gas, and baked in a 80^{o}C oven for 1 hour.

These treated glass discs were substrates on which microwell arrays were built. The body of the array was made of polyethyleneglycol diacrylate (PEG DA) of MW1000. The polymer solution was prepared by first dissolving PEG DA in PBS to form a 20% solution, then adding to this solution the photoinitiator 2-hydroxy-2 methyl propiophenone (Sigma) an amount equivalent to 10wt% of the polymer. 50 μL of the polymer solution was used to evenly coat a microwell array template, which had dimensions of roughly 10 mm x 10 mm, before the template was inverted and

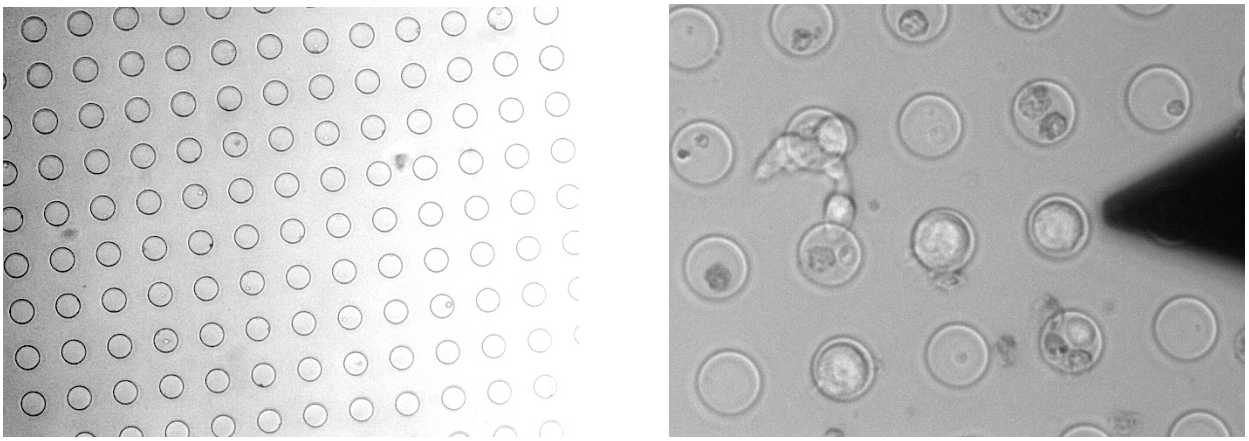

Figure 2-6: Microwell arrays with wells 8 μm (left) and 16 μm (right) in diameter. The image on the right shows three activated T cells confined by the wells. The dark triangle is an AFM probe.

finger-pressed against a treated disc for 60 seconds. Residual liquid was removed with a Kimwipe, and the assembly was carefully placed in a 35-mm petri dish and placed under a hand-held UV light source for 30 minutes to cross-link the polymer. Afterward, the PDMS template was carefully removed with tweezers, starting from a corner of the template, and

the resultant microwell array structure was inspected under a microscope for its structural fidelity and integrity (Figure 2-6).

The AFM Device

The AFM system used in this work consists of a MFP-3D-BIO from Asylum Research that is integrated with a Carl Zeiss inverted microscope. The microscope sits on a vibration-isolation table, and this entire assembly is enclosed in a vibration-isolation chamber. The AFM headpiece and the sample stage respectively control the movement of the probe in the z-direction and the movement of the sample in the x- and y-directions. Precise distance increments are possible through the use of piezoelectric crystals. The sample stage allows manual control of the sample position when large translations are desired. Data acquisition and storage were done through the AFM software that is based on the software IgorPro. A CCD camera, controlled by the software AxioVision from Carl Zeiss, is attached to the side of the microscope to provide image-capturing capability. Real-time images of an experiment could be displayed both in the microscopy software and on a separate monitor.

2.2.4 Elasticity Study of T Cells

Experimental Procedure

Approximately 3 x 10^5 of T cells were transferred to an eppendorf and spun down at 2,000 rpm for 5 minutes at room temperature. All except about 100 μL of supernatant was removed before the cell pellet was resuspended in the remaining liquid. 10 μL of trypan blue was added to the cell sus-pension, and the resultant mixture was immediately diluted by adding to it 600 μL of the medium that the cells would be tested in. Approximately 450-550 μL of this mixture was subsequently injected into a micropipette aspiration sample chamber. Since live and dead cells could not be distinguished under bright-field microscopy, trypan blue was used to label dead cells to prevent them from being included in the sample pool.

Before cell testing could start, the fluid level in the water column corresponding to zero pressure was estimated (Figure 2-6). This was achieved by manually adding or withdrawing water from the water column via the reservoir in the 50-mL syringe and observing the movement of a cell next to the opening of the micropipette. Zero pressure was assumed when the cell neither moved toward or away from the micropipette opening. The fluid level at this instant was used as the zero-pressure level for subsequent testing.

Round, shiny cells, indicative of healthy cells, were identified by eye under a microscope and selected for aspiration. The micropipette at zero pressure was brought into contact with the cell, and cell aspiration was initiated by starting the syringe pump. For all experiments, the aspiration rate and volume were set to 36 mL/hour and 2 mL. This combination was chosen because it yielded obvious cell length increments with increasing pressure and resulted in sufficient data points for proper data analysis. The values

corresponded to a total pressure of approximately 400 Pa that was applied in 200 seconds. At the moment cell aspiration instigated the image capturing software was started in parallel to record the progression of the cell into the micropipette during the whole testing period.

Data Analysis

The advancement of a cell into a micropipette was manually tracked on images taken during an experiment using the ImageJ software (NIH). The change in cell length inside the micropipette with respect to the pressure increment was determined, and this information was fitted using the half-space model [154], which makes the assumption that a cell behaves like a linearly elastic, homogeneous, and isotropic semi-infinite solid, whose apparent Young's modulus is described by the relationship:

$$E = \varphi(\eta)\frac{3r_i}{2\pi}\left(\frac{\Delta p}{L}\right) \qquad \eta = \frac{r_o - r_i}{r_i} \qquad (2.1, 2.2)$$

where E is the apparent Young's modulus of the cell, Δp is the pressure differential, L is the cell length in the micropipette including the cell cap, r_i and r_o are the inner and outer diameter of the micropipette, and φ is the wall function, which is a function of the wall thickness of the micropipette and was assumed to be 2 for this work [154]. The total pressure exerted on the cell can be calculated from the total volume of liquid that is removed from the water column:

$$p = \rho g h \quad (2.3)$$

where ρ is the density of water, g is the gravitational acceleration, and h is the chainge in height of the water level in the column. Rearrangement of this equation results in a linear increase of Δp with respect to the ratio L/r_i, and the slope of the linear line allows E to be calculated. Therefore, experimental data for every cell were converted into a Δp vs L/r_i plot, and the linear line that best fit the plot was determined. The slope of this linear fit allowed an apparent Young's modulus to be calculated.

2.2.5 Viscosity Study of T Cells

Experimental Procedure

Approximately 1 x 10^6 cells were transferred to an eppendorf and spun down at 2,000 rpm for 5 minutes at room temperature. All except about 100 μL supernatant was removed, then the cell pellet was resuspended in this remaining liquid. 10 μL trypan blue was added to the cell suspension, and the resultant mixture was immediately diluted by adding to it 3 mL of a medium that the cells would be tested in. 2.5 mL of this mixture was subsequently transferred to a fluid cell containing a microwell array of the appropriate well diameter.

AFM probes (Olympus, Model# TR400PSA) were individually tested in air for their spring constants before they were used. After loading a probe into the AFM system,

the laser spot was positioned on the larger triangular cantilever, and its position was tweeked until the sum signal was maximized. The tip was then engaged, through the AFM software, on a clean microscope slide sitting on the AFM stage, before it was disengaged and physically retracted from the glass surface by turning the thumbwheel 5-6 turns on the AFM head. The system was left in this condition for 30 minutes to stabilize the cantilever deflection signal. Afterward, the deflection signal was zeroed and the AFM tip was again engaged on the slide. A force-displacement curve was obtained to determine the sensitivity of the tip. The non-contact portion of the curve was used to correct for virtual deflection. At this point, the tip was retracted from the glass surface, and a thermal spectrum was collected via the AFM software. By selecting the correct resonance peak from the spectrum, the software used this information, together with the sensitivity value determined earlier, to calculate a spring constant for the AFM probe. The range of spring constants used for this work was 0.017-0.024 N/m. (manufacturer quotes 0.02 N/m).

The instrument was operated in contact mode to perform cell indentation. After loading a pre-calibrated AFM probe and a sample into the instrument, the probe was lowered to engage the sample substrate, raised 5-6 turns by turning the thumbwheel on the AFM head, and the expe-rimental system was allowed to equlibrate for about 30 minutes at room temperature to stabilize the cantilever deflection. After zeroing the deflection signal, the sensitivity of the probe was determined from a force-displacement curve obtained from the glass substrate that contained the microwell array. The probe was then retracted, raised 10 turns, and the microscope stage was translated to position the cell-seeded microwell array directly below the probe. A speed range spanning about 3

orders of magnitude was used to indent cells. For each speed, the force exerted by the AFM tip on the cell was tailored, by adjusting the trigger point, to result in an indentation depth of 1-1.5 μm. Five to ten deflection-displacement curves were obtained at the center of a cell. Every experiment was limited to not more than 3 hours.

Data Analysis

The variation of the apparent Young's modulus of naïve and activated T cells with indentation rate was used to compare their viscous property. The deflection v.s. displacement curves collected were first converted into force v.s. indentation curves, then the contact portion of the approach curve of an experiment was fitted to the Hertz model [155], described by the relationship:

$$\delta^2 = \frac{4F(1-\nu^2)}{3E\tan\alpha} \qquad (2.4)$$

where E is the apparent Young's modulus of the cell, δ is the indentation depth, F is the indentation force, α is the half-angle of the pyramidal probe and was approximated as 35° as quoted by the manufacturer, and ν is Poisson's ratio of the cell, which was assumed to be 0.5 for an incom-pressible solid. This model assumes a cell behaves like a linearly elastic, homogeneous, and isotropic semi-infinite solid. The equation given here is formulated specifically for pyramidal indenters.

A MATLAB program based on the work of Costa [156] was written to perform least-square fitting of the experimental data, and two parameters were fitted for, the apparent Young's modulus and the point of contact. In order to do so, indentation depth was expressed in terms of cell displacement:

$$\delta = s - s_0, \qquad s = z - d \qquad (2.5, 2.6)$$

where s is the displacement of the cell , s_o is the point at which the AFM indenter contacts the cell, z is the position of the piezoelectric unit that moves the indenter, and d is the deflection of the indenter. Combining equations 2.4 to 2.6 yields the final equation used for fitting:

$$(z - d - s_0)^2 = \frac{4F(1-\nu^2)}{3E\tan\alpha} \qquad (2.7)$$

2.2.6 Migration Study of T Cells

Enriched WT and WAS-/- T cells, prepared following the procedure delineated in Chapter 2, section 2.1, were exchanged into DMEM with 1% BSA and 0.1% Pen/Strep and subsequently induced to migrate through polycarbonate Transwell inserts (Costar) containing 5-μm pores. The inserts were placed in 24-well plates, and each insert divided a well into a top compartment that was seeded with 5 x 10^5 T cells in 100 μL of the DMEM medium, as well as a bottom compartment that contained 1 mL of the DMEM medium with

either no chemokine or 100 ng/mL of the chemo-kine CCL19 (R&D Systems). Cells were allowed to migrate for approximately 7 hours in a 37^{o}C incubator, and those that successfully crossed the membrane to the bottom compartment were collected and immediately tested using micropipette aspiration.

Micropipette aspiration experiments were conducted on WT and WAS-/- T cells that migrated in response to the chemokine source to determine their apparent Young's modulus values following the procedure outlined in section 2.2.3. The micropipettes used had the same inner diameter range, 2.5-4 μm, as those used for naïve T cells. The testing medium was the medium from the bottom of the well from which the cells were originally retrieved. As described in section 2.2.3, cells were aspirated at 36 mL/hour using a syringe pump, and the total volume aspirated was 2 mL. Micropipette aspiration data on migrating T cells were analyzed as previously described in this chapter, section 2.2.4. The movement of the cell leading edge into the micropipette with increasing pressure was tracked using the ImageJ software. This information, together with the pressure increment, was fitted using the half-space model to derive an apparent Young's modulus for the cell under study.

2.3 Results

2.3.1 Purity and Activation Status of T Cells

Since most splenocytes are not T cells, the cell extract from the lymph node and the spleen of mice was subjected to an enrichment procedure to separate T cells from unwanted cells. This procedure magnetically labeled and removed undesirable cell populations (such as B cells, macrophages, monocytes) while leaving T cells untouched. FACS analyses of the enriched T cell population confirmed an increase in purity from approximately 10% to 90% for cells harvested from both WT (in this case the Balb/c strain) and WAS-/- mice. To ensure the health of the cell subjects, which quickly deteriorates at room temperature (25^{o}C), naïve T cells were tested within 24 hours of their harvest, with every experiment lasting no longer than three hours.

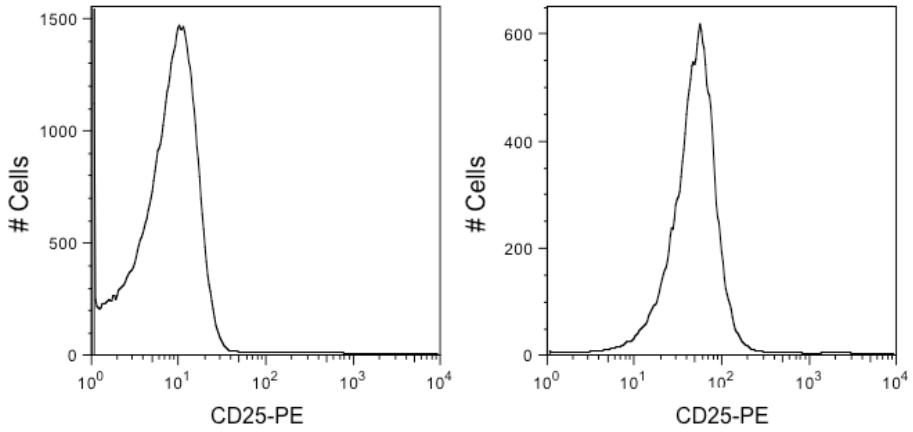

Figure 2-7: FACS analysis of the expression of the cell activation marker, CD25, before (left) and after (right) four days of activation of WT (Balb/c) T cells. The large shift in the peak of the PE fluorescence signal indicates successful activation.

Activated T cells were obtained by culturing naïve T cells at 37^{o}C in a 6-well plate that was pre-coated with anti-CD3 antibodies, with the cell culture medium supplemented with interleukin (IL)-2 and anti-CD28 antibodies. At various time points during the activation

process, cell samples were removed from the plate and tested for their expression of CD25, a T cell activation marker. These results showed that four days of activation was sufficient to induce a high expression of this marker on 90% of the cells (Figure 2-7). Therefore, for all the work in this thesis involving activated T cells, cells were tested at room temperature within the 24-hour period on their fourth day of activation. To make the testing condition consistent, activated T cells were also studied within three hours of their removal from the incubator. In contrast to the WT cells, only about 50% of the WAS-/- cells displayed a strong CD25 staining on day four under the same culture condition. This pattern of impaired cell activation through CD3 conjugation agrees with previous findings [19, 20]. Even though the activation efficiency of WAS-/- T cells was low, those that were successfully activated were much larger in size than their naive partners so could be easily identified by eye for testing. For both WT and WAS-/- T cells, regardless of their activation state, similar results were obtained from the beginning and the end of a three-hour experiment, as well as during the 24-hour testing period.

2.3.2 Influence of Cell Activation

Based on the assumption that cells possess mechanical properties that allow them to adjust to and accommodate their environments, the dissimilar homing routes of naïve and activated T cells leads one to speculate that the activation process alters the mechanical properties of these cells. Micropipette aspiration experiments were conducted to study their elastic responses. Most leukocyte studies utilize the liquid droplet model for data fitting, but these studies usually involve neutrophils, which have a small multi-lobed

nucleus surrounded by a large cytoplasm. In contrast, naïve T cells have a high nucleus to cytoplasm ratio that likely renders them more solid-like than liquid-like. Thus, the half-space linear elastic solid model (Equations 2.1-2.3) was chosen to describe their elastic behavior. Figure 2-8 shows some example fits obtained from naïve T cells.

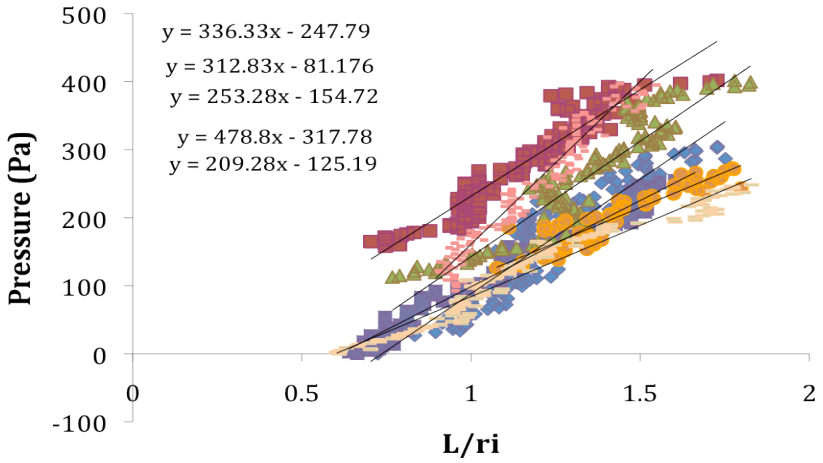

Figure 2-8: Fitting micropipette aspiration data using the half-space model to derive apparent Young's modulus values for T cells. Even though the data shown here were obtained from naïve WT (Balb/c) T cells, the linear fits (solid lines) are representative and characteristic of all the cell populations tested in this work. The equations for five of the liner fits are shown. The modulus is calculated from the slope of a linear fit as described in the text.

The reasonably good overlap of the linear fits and the experimental values indicates the appropriateness of the model. The equations of five of these fits, corresponding to five different cells, are displayed in the figure, where the slope of each line allows a modulus to be calculated for the particular cell. The average modulus of naïve T cells obtained this way was 290+/-102 Pa (mean +/- SD) (n=22) (Figure 2-9). Despite having a larger cytoplasm, activated T cells yielded fits of similar goodness as their naïve partners when modeled as a

solid (data not shown). Their modulus decreased more than two folds from that of naïve T cells to 94+/-49 Pa (n=26) (Figure 2-9).

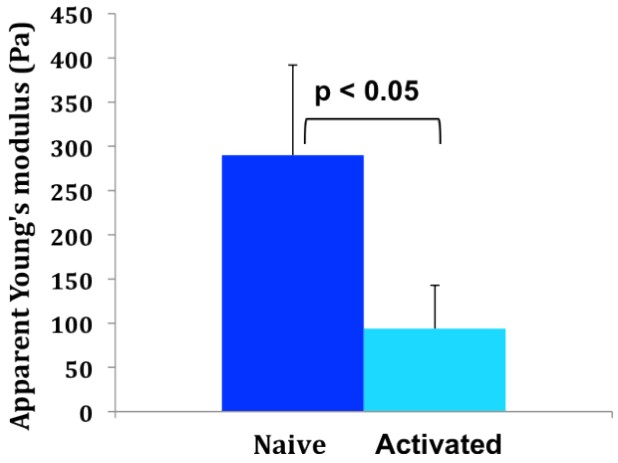

Figure 2-9: The average apparent Young's modulus of WT T cells before (naive) and after (activated) cell activation. The modulus is 290+/-102 Pa (n=22) and 94+/-49 Pa (n=26) for the naïve and activated WT T cells, respectively. The error bars designate the standard deviation. A Student's t test showed the difference between the two groups to be statistically significant ($p < 0.05$).

In order to investigate the viscous nature of T cells before and after activation, the variation of the cells' apparent Young's modulus with deformation rate was probed at 200 nm/sec, 1 μm/sec, 10 μm/sec, 20 μm/sec, and 50 μm/sec, using AFM. This range was selected as velocities lower than 200 nm/sec led to a severe drift in the cantilever position and yielded distorted indentation curves, while the AFM apparatus could not physically move the indenter faster than 50 μm/sec with the present setup. Based on the same consideration that a naïve T cell is composed of a large nucleus surrounded by a thin layer of cytoplasm, the approach curve of every indentation curve from T cells both before and after activation was fitted using the linear elastic Hertz model (Equations 2.4-2.6). A

MATLAB program written to execute the fitting routine yielded both the coordinate of the tip-cell contact point and the apparent Young's modulus of the cell. An example fit is shown in Figure 2-10 (left panel). The good overlap of the fit and the experimental data indicates the appropriateness of the model. The average modulus of naïve T cells at the five selected indentation speeds were determined as 264+/-87 (n=17), 293+/-119 (n=17), 358+/-120 (n=21), 454+/-116 (n=19), and 525+/-99 (n=22) Pa.

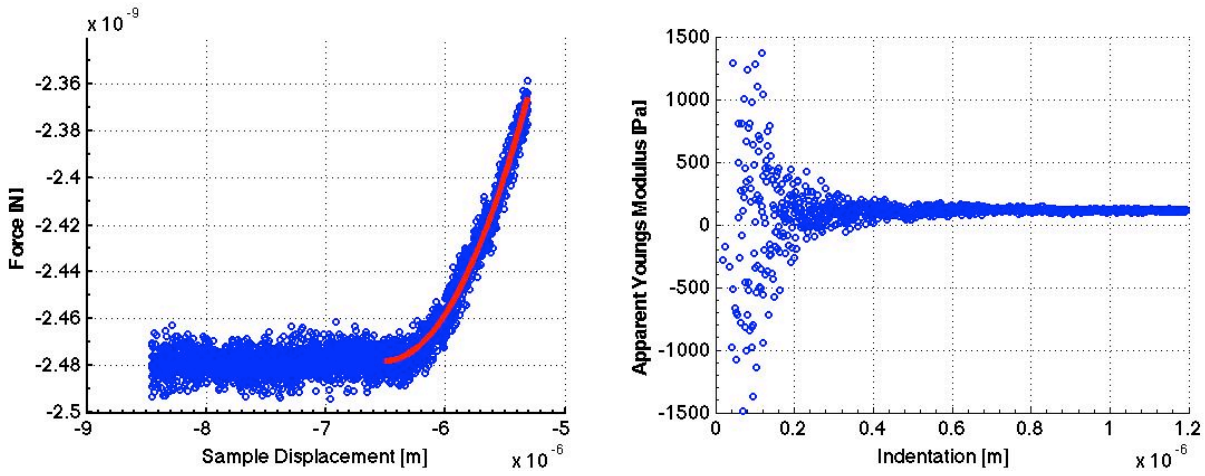

Figure 2-10: (Left) A representative approach curve from an AFM cell indentation experiment fitted with the linear elastic Hertz model. The Hertzian fit is shown in red and the experimental data are shown in blue. (Right) Variation of the apparent Young's modulus of a T cell with cell indentation depth. The shape of the plot is characteristic of both naïve and activated T cells.

A concern of indenting a small cell, such as a T cell, is the accidental probing of the underlying substrate, which would lead to an overestimation of the cell stiffness. In order to identify such an occurrence, variation of the modulus of each cell was plotted against cell indentation depth (Figure 2-10, right panel). Large fluctuations were typically observed at the beginning of a plot. This noise probably arose from the uncertain contact

geometry of the pyramidal indenter with the cell, as well as from the cell being pushed away by the indenter before a stable contact could form. The modulus quickly stabilized and became constant between zero and a few hundred Pascals, a value typical of a biological cell.

Figure 2-11 shows the variation of the modulus of T cells before and after activation with the indentation speed. A continuous increase of the cellular stiffness for both populations is observed at a similar rate (slope) up to about 10 μm/sec, at which point this trend is interrupted by a transition in the case of naïve T cells. Afterward, the modulus of these cells continues to rise but does so at a higher rate. In contrast, activated T cells do not appear to go through a transition in stiffness for the same range of indentation speeds. Examination of the AFM indentation curves

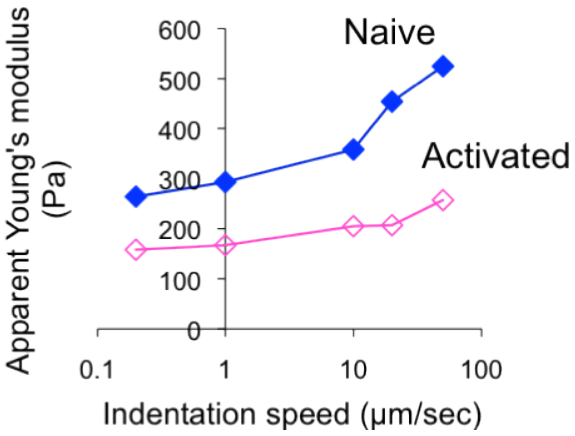

Figure 2-11: Variation of the apparent Young's modulus of naïve and activated WT T cells with AFM indentation speed. Cells were tested at 200 nm/sec, 1 μm/sec, 10 μm/sec, 20 μm/sec, and 50 μm/sec. The data points shown are the mean of the modulus values obtained at the indicated testing speeds. The modulus of naïve T cells at the five speeds were determined as 264+/-87 (n=17), 293+/-119 (n=17), 358+/-120 (n=21), 454+/-116

(n=19), and 525+/-99 (n=22) Pa. Similarly, the modulus for activated T cells were found to be 158+/-47 (n=23), 167+/-50 (n=30), 205+/-74 (n=29), 207+/-54 (n=23), and 257+/-91 (n=27) Pa.

from activated T cells revealed that about 30% of them did not conform to the Hertz model. Instead of a smooth transition from the non-contact to the contact portion of the curve, as seen in Figure 2-11, these non-conforming plots display an obvious 'kink' at the transition. This deviation from the Hertzian fit was also observed for naïve cells but was only manifested in a very small number of indentation curves. This feature was reported in a previous AFM study [138] as a characteristic of a fluid-like behavior (Figure 2-18) (see the Discussion section). Curves displaying this behavior were excluded from the data analyses that led to the results presented here. The resultant average moduli calculated this way for the five indentation speeds are 158+/-47 (n=23), 167+/-50 (n=30), 205+/-74 (n=29), 207+/-54 (n=23), and 257+/-91 (n=27) Pa.

2.3.3 Influence of WAS Genetic Defect

The phenotype of WAS-/- T cells, together with the actin-regulatory role of WASp, suggests a defective actin arrangement of these cells compared to their WT counterparts. This leads to the hypothesis that WAS-/- and WT T cells probably possess dissimilar mechanical properties. Micropipette aspiration experiments revealed that naïve WAS-/- T cells had a mean apparent Young's modulus of 190+/-69 Pa (Figure 2-12), about 53% less than the 290+/-102 Pa determined previously for naïve WT T cells. After activation, WAS-/- cells became less stiff and yielded an apparent Young's modulus of 121+/-41 Pa. This 57%

modulus reduction is smaller than the two-fold reduction observed for WT T cells upon activation. Student's t tests conducted showed that the stiffness difference both between naïve WT and naïve WAS-/- T cells, and between naïve and activated WAS-/- T cells, was significant ($p < 0.05$). In contrast, the disparity in modulus between activated WT and activated WAS-/- T cells did not pass the 95% significance level ($p > 0.05$). As before, the half-space model was used for data fitting and described both naïve and activated WAS-/- T cells well.

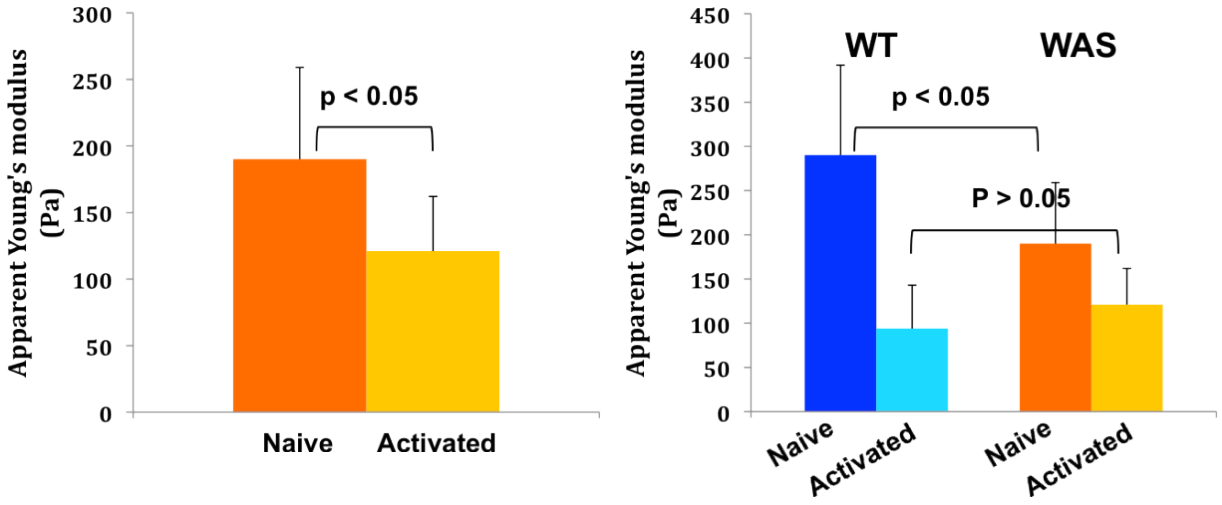

Figure 2-12: (Left) Average apparent Young's modulus of WAS-/- T cells before (naive) and after (activated) cell activation as determined by micropipette aspiration. The modulus is 190+/-69 Pa (mean +/- SD) and 121+/-41 Pa for naïve and activated WAS-/- T cells, respectively. (Right) The average moduli for WT and WAS-/- T cells before and after activation are shown side-by-side for comparison. The error bars designate the standard deviation. Student's t tests showed a statistically significant stiffness difference both between naïve WT and naïve WAS-/- T cells, and between naïve and activated WAS-/- T cells ($p < 0.05$), but not between activated WT and activated WAS-/- T cells ($p > 0.05$).

AFM experiments unveiled that the variation of the apparent Young' modulus with the indentation speed for naïve WAS-/- T cells was similar to that of naïve WT T cells (Figure 2-13), with the plot of the former always lying below that of the latter. The same

linear elastic Hertz model used before was also applied to naïve WAS-/- T cells to generate good fits similar to that shown in Figure 2-11. These cells were also tested at 200 nm/sec, 1 μm/sec, 10 μm/sec, 20 μm/sec, and 50 μm/sec, as described in the previous section, and the corresponding elastic moduli were 220+/-48 (n=17), 217+/-65 (n=43), 320+/-77 (n=22), 386+/-131 (n=21), and 525+/-150 (n=14) Pa. Comparing the AFM data of naïve WT and naïve WAS-/- T cells through Student's pair-wise t tests showed that the modulus difference was significant ($p < 0.05$) at the two lowest indentation speeds but insignificant ($p > 0.05$) at the three higher speeds. Even though not all the speeds tested yielded significantly different stiffness values for the two populations, the trend obtained in this case still agrees with that observed in micropipette aspiration studies, that the modulus of WAS-/- cells was lower.

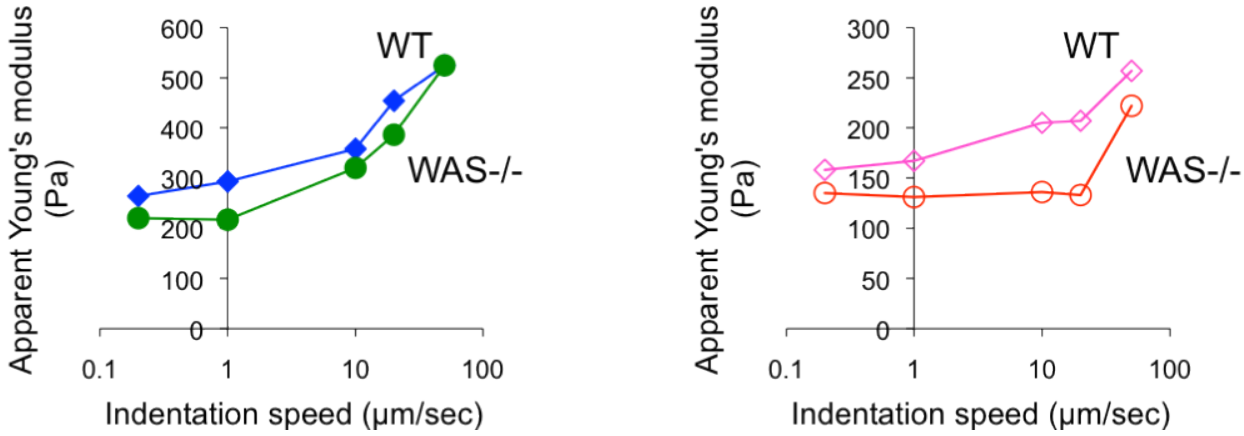

Figure 2-13: Variation of the apparent Young's modulus of WT and WAS-/- T cells in the naïve (left panel) and activated (right panel) state with the AFM indentation speed. Cells were tested at 200 nm/sec, 1 μm/sec, 10 μm/sec, 20 μm/sec, and 50 μm/sec. The data shown are the mean of the modulus values obtained at the indicated testing speeds. For naïve WAS-/- T cells, the elastic moduli corresponding to the tested speeds were 220+/-48 (n=17), 217+/-65 (n=43), 320+/-77 (n=22), 386+/-131 (n=21), and 525+/-150 (n=14) Pa. (Left panel) The shape similarity of the curves for the former suggests that naïve WT and

WAS-/- T cells respond to increased deformation rates with a similar resistance. (Right panel) Compared to the steady rise in the modulus observed for activated WT T cells, the unvarying stiffness in activated WAS-/- T cells below 20 μm/sec suggests an impaired viscous response. The elastic moduli for these cells are 135+/- 40 (n=17), 131+/-48 (n=27), 136+/-33 (n=20), 133+/-30 (n=20), and 222+/-53 (n=11) Pa.

In contrast to the naïve cell data, AFM indentation results from activated WAS-/- T cells indicate that the presence of WASp is necessary for T cells to generate a normal viscous response. Instead of the steady rise in the apparent Young's modulus with the indentation rate observed in activated WT T cells, activated WAS-/- T cells maintained their modulus around 130 Pa despite a two orders of magnitude increase in the indentation speed from 200 nm/sec to 20 μm/sec (Figure 2-13, right panel). At the highest indentation speed tested (50 μm/sec), the modulus abruptly jumped up to approximately 220 Pa. Similar to their WT counterparts, about 30% of the activated WAS-/- T cells also displayed a liquid-like nature, as characterized by the sharp (instead of smooth) transition in their force-indentation depth curves (see section 2.2.2). These anomalous curves were excluded from the data analyses that led to the results presented here. The elastic moduli thus determined are 135+/- 40 (n=17), 131+/-48 (n=27), 136+/-33 (n=20), 133+/-30 (n=20), and 222+/-53 (n=11) Pa for cell indentation at 200 nm/sec, 1 μm/sec, 10 μm/sec, 20 μm/sec, and 50 μm/sec.

2.3.4 Influence of Chemokines

It has been shown that WAS-/- T cells manifest impaired chemotaxis, but the mechanical origin of this behavior is unclear. Since WASp is a regulator of actin, the main cytoskeletal

component that confers a cell its stiffness, it was hypothesized in this work that the defective migration arose from the ineffective adjustment of the stiffness of these cells in response to chemical stimulation, which may stem from an improperly organized and cross-linked actin network. To evaluate this hypothesis, transwell migration experiments were conducted on naïve WT and WAS-/- T cells. Cells that responded to the chemokine CCL19 and migrated across the transwell insert were tested for their apparent Young's moduli using micropipette aspiration.

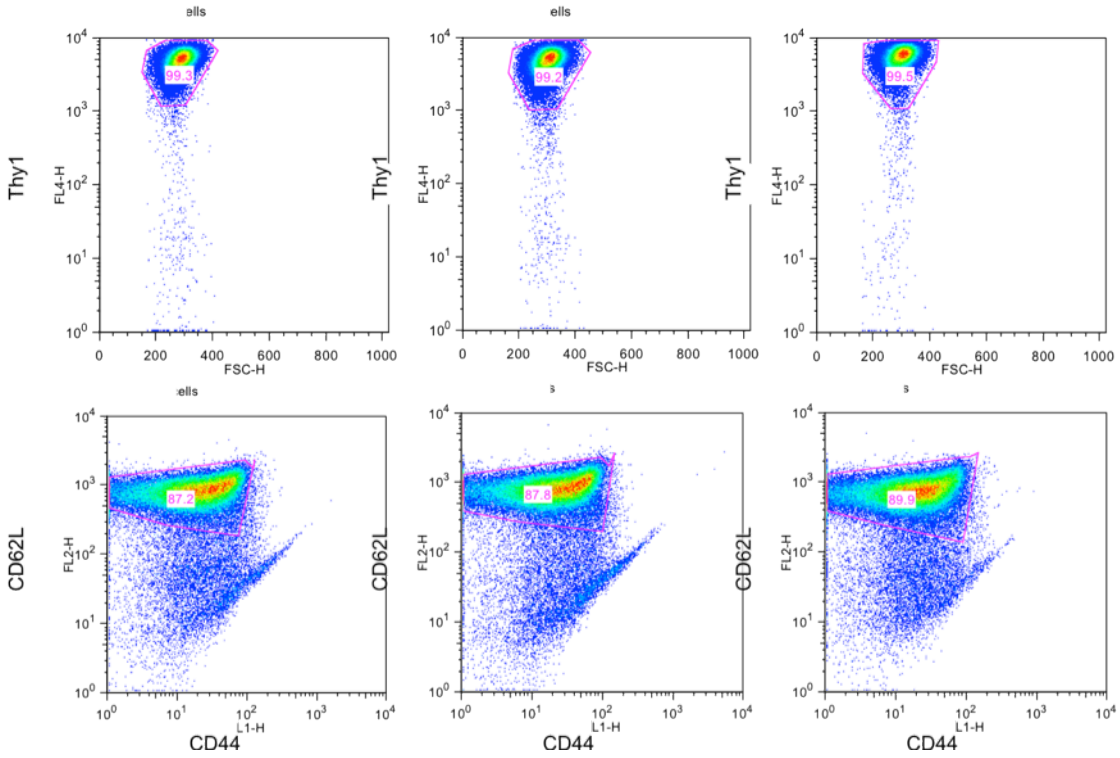

Figure 2-14: FACS analysis of the phenotype of naïve WT T cells induced to migrate by chemokine stimulation. T cells were first gated on PI to exclude dead cells (not shown). The cell samples tested were naïve T cells not exposed to CCL 19 (A, D), cells that remained in the insert after CCL19 exposure (100 ng/mL) for seven hours (B, E), and cells that migrated across the insert membrane after the same chemokine treatment (C, F). Gating on Thy1 (A-C), one marker that identifies T cells, revealed that more than 99% of the cells in all three samples were most likely T cells. Gating simultaneously on CD62L and CD44 (D-F) showed

that a similar percentage of cells stained CD62L high and CD44 low, indicative of the naïve phenotype.

About 18.5% of the naïve WT T cells migrated after seven hours of stimulation. The phenotype of these cells was analyzed to determine their activation state, as the 'naïve' cell population obtained from the mouse spleen and lymph nodes actually contains a very small percentage of memory T cells, which tend to respond more rapidly to immune stimulations than naïve T cells. Cells from both sides of a transwell insert at the end of a migration experiment, as well as cells that were not exposed to the chemokine (controls), were co-stained with fluorescent anti-CD62L and anti-CD44 antibodies. FACS analyses showed that approximately 90% of the cells from all three groups expressed a high level of CD62L and a low level of CD44 (Figure 2-14), indicative of the naïve phenotype. CCL19 stimulation reduced the apparent Young's modulus of naïve WT cells more than one fold from 290+/-102 Pa to 128+/-33 Pa (Figure 2-15). About 6.4% of the WAS-/- T cells migrated after seven hours of CCL19 exposure. CD62L and CD44 co-staining of these cells yielded a similar staining result, namely that close to 90% of the cells in all three groups had the naïve phenotype (data not shown). The apparent Young's modulus of naïve WAS-/- cells decreased from 190+/-69 Pa pre-stimulation to 152+/-102 Pa post-stimulation (Figure 2-15). A Student's t test showed that the difference between these values did not pass the 95% significance level ($p > 0.05$).

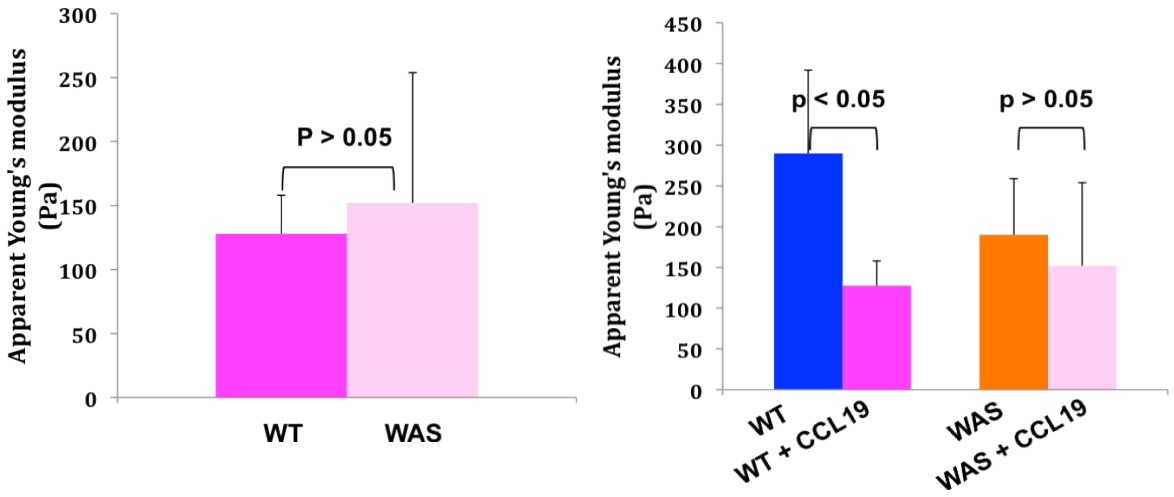

Figure 2-15: (Left) The average apparent Young's modulus of WT and WAS-/- T cells before and after stimulation with chemokine CCL19. The modulus is 128+/-33 Pa (mean +/- SD) and 152+/-102 Pa for the stimulated WT and WAS-/- T cells, respectively. (Right) The moduli for WT and WAS-/- T cells before and after chemokine exposure are shown side-by-side for comparison. The error bars designate the standard deviation. Student's t tests showed a statistically different modulus difference ($p < 0.05$) between untreated and CCL19-treated WT T cells but not between treated and untreated WAS-/- T cells ($p > 0.05$).

Cell type/Cell conditions	Modulus (Mean +/- SD) (Pa)	# Cells
WT/Naïve	290 +/- 102	22
WT/Activated	94 +/- 49	26
WT/Naïve, CCL19	128 +/- 33	31
WAS-/-/Naive	190 +/- 69	30
WAS-/-/Activated	121 +/- 41	24
WAS-/-/Naïve, CCL19	152 +/- 102	32

Table 2-1: Summary of the apparent Young's modulus values as determined by micropipette aspiration for the listed cell type, the treatment they received, and the number of cells tested for each category.

2.4 Discussion

Effect of activation on T cell elasticity and viscosity

Observing the differential migration patterns of naïve and activated T cells, we hypothesized that the cell activation process would change these cells' mechanical properties and showed a more than two-fold reduction in these cells' apparent Young's modulus from 290+/-102 Pa to 94+/-49 Pa. This result likely arises from the alteration of the T cell cytoskeleton upon activation. Fluorescence staining of naïve T cells revealed a cortical actin mesh lying below the plasma membrane, an intermediate filament cage that permeates the cytoplasm, and microtubules that radiate outward from the microtubule organizing center (Figure 2-16, a-c) [100]. Upon contacting an activating surface, the cytoskeleton of T cells undergoes substantial changes [17, 109]. Actin reorganizes and begins to polymerize immediately [17, 109], leading to T cell spreading and the formation of a ring of polymerized actin at the cell circumference over a period of 2-3 minutes [157]. Both the actin filaments and MTOCs also translocate to specific intracellular locations [121, 158]. Engagement of TCR results in the release of ezrin-radixin-moesin (ERM) family proteins that anchor the cytoplasmic portions of transmembrane proteins to the cortical actin cytoskeleton [108]. This process relaxes the cortical actin layer and consequently may contribute to the observed stiffness reduction.

A small collection of studies exists on the mechanical behaviors of T cells, but most of this work is only qualitative. The few experiments that tried to quantify the mechanical properties of T cells [81, 82, 136] yielded results not directly comparable to the present finding. In order to gain some insights into the accuracy of the present results, we

compared them to the elastic moduli of cell types close to T cells. Both lymphocytes and neutrophils belong to the leukocyte family and follow a similar migration procedure, although the latter has a larger cytoplasm to nucleus ratio. Two other possible comparisons

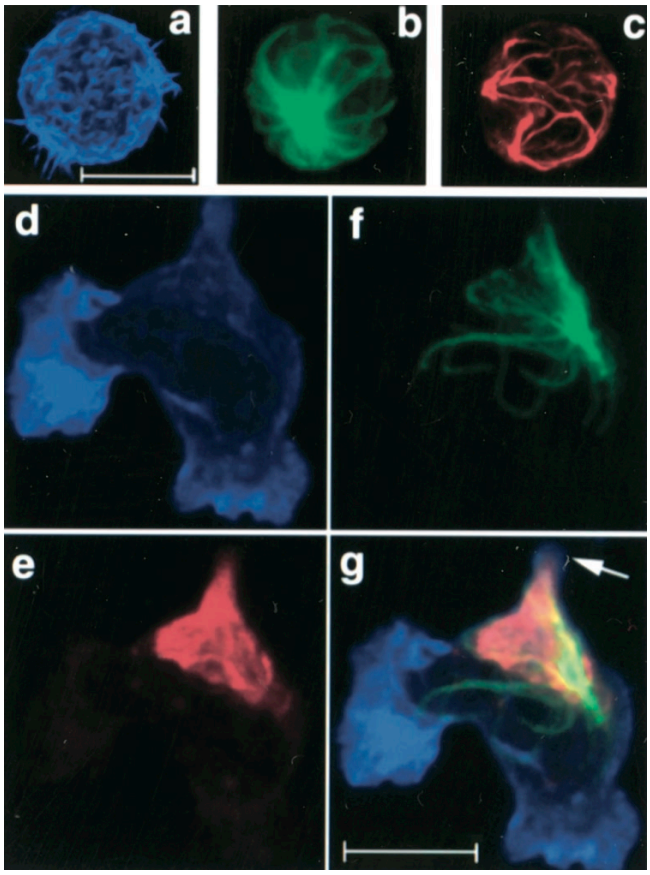

Figure 2-16: Confocal microscopy images of fluorescently labeled peripheral blood T lymphocytes (PBT) upon exposure to the chemokine SDF-1 showing cytoskeletal rearrangement and polarization. In a resting PBT, actin microfilaments form a shell that lies directly below the cell membrane (a, blue). Microtubules radiate outward from MTOCs (b, green), and vimentin intermediate filaments form a cage-like network that permeates the cytoplasm (c, red). After a 3-min exposure to 100 ng/mL of chemokine, a PBT polarizes and exhibit lamellapodia in the leading edge and an uropod in the cell rear (g). All three cytoskeletal elements undergo reorganization. Actin concentrates in the cell leading edge (d, blue), while both the microtubule (f, green) and intermediate filament (e, red) structures collapse and retract into the uropod. A composite image of the three stainings from d, e, and f, is shown in g. Scale bar = 5 μm. Figure from Brown *et al.* [100]

are the Jurkat cell, an acute leukemia cell line of the lymphoid origin, and the HL-60 cell, a cell line that expresses most of the adhesion molecules found on T cells [159]. The apparent Young's moduli of neutrophils, the Jurkat cell, and the HL-60 cell were determined to be 156 Pa, 48 Pa, and 855 Pa in an AFM study [138]. Compared to these values, the present findings of 290+/-102 Pa and 94+/-49 Pa for naïve and activated T cells are on the same order of magnitude. Activated T cells are probably more similar in nature to Jurkat cells since the patterns of cytochemical staining and membrane receptors of Jurkat cells are similar to those of lymphoblasts [160]. In addition, *Zahalak et. al.* showed in their calculations that naïve T cells are expected to be significantly stiffer than neutrophils [136], which is the trend observed here.

The stiffness reduction discovered in the current work is in agreement with other cell systems upon activation and differentiation. Lautenschlager *et al.* used a microfluidic optical stretcher to measure the creep compliance of acute promyelocytic leukemia cells induced to differentiate down the neutrophil lineage for three days [11]. The differentiated cells were found to be 45% more compliant than the control and similarly compliant to neutrophils. Electron microscopy of the differentiated population revealed an increase in the subcortical actin network size compared to the undifferentiated one. Since the network size is inversely related to its elastic shear modulus [11], this size increase explains the greater compliance of the differentiated cells. Titushkin *et al.* characterized the mechanical properties of human mesenchymal stem cells as they differentiated into osteoblasts and found a reduction in their average Young's modulus from 3.2 kPa to 1.7 kPa [161].

The change in the elastic property of T cells due to activation may be required to prepare them for their new biological role, which involves traversing a different circulation path to arrive at different lymphoid tissues, followed by extravasation and maneuvering in the tissues to reach inflamed sites. Correlation of the mechanical properties of a cell with its biological functions has been demonstrated by several studies. Mathur *et al.* hypothesized a higher stiffness for muscle cells than endothelial cells due to the contractile role of the former and confirmed this hypothesis by showing the apparent Young's modulus of endothelial, skeletal muscle cells, and cardiac muscle cells to be 1.4-6.8 kPa, 24.7 kPa, and 100.3 kPa, in that order [162]. Guilak and coworkers suspected that cells from the different zones of the intervertebral disc had varied mechanical properties to accommodate the complex pattern of mechanical loading in this tissue [163]. They unveiled that cells in the nucleus pulposus zone, which experience an isotropic stress-strain environment, were about three times stiffer and significantly more viscous than cells in the annulus fibrosus zone, which endure an anisotropic and heterogeneous state of tension, compression, and shear. Merryman *et al.* compared the stiffness and collagen content of heart valve interstitial cells from the left and the right side of the heart and discovered that those from the left side contained a significantly higher amount of smooth muscle α-actin and collagen, correlating with the much larger transvalvular pressure that cells on the left side must endure [25].

Cells are viscoelastic materials whose apparent stiffness depends on the rate at which they are deformed. As this rate increases, the viscous nature of the cells results in

their increasing resistance to deformation, causing them to appear stiffer. Biologically, the continuous rise of the T cell stiffness as seen in Figure 2-12 means that as a T cell tries to move faster, it will experience a larger resistance trying to propel its viscous content forward. In their study investigating the force a neutrophil generates during transmigration, Rabodzey *et al.* observed that the maximum opening between two endothelial cells during neutrophil passage was about 4 μm in diameter, with the transmigration process completed in 85+/-20 sec [122]. Knowing that the average diameter of a human neutrophil is approximately 8.3 μm [138] and assuming that the transmigrating neutrophil needs to squeeze through an intercellular opening 4 μm in diameter, the velocity of migration ranges from 0.23 to 0.37 μm/sec. This range is comparable to the migration velocity found for naïve T cells in an intact lymph node [97], 10 μm/min (0.17 μm/sec) on average and up to 25 μm/min (0.42 μm/sec). Inspection of the variation of the apparent Young's modulus of naïve and activated WT T cells with AFM indentation velocity (Figure 2-11) shows that at the calculated transmigration speeds, the stiffness of naïve and activated cells is 264-293 Pa and 158-167 Pa, respectively. It should be noted that the transmigration speeds discussed here are only rough estimations based on in vitro migration data of neutrophils. T cells in vivo may travel at different velocities depending on their stage of migration, for example, whether they are circulating in the blood and the lymph, transmigrating across a blood vessel, or maneuvering in tissues.

The transition observed at 10 μm/sec for naïve T cells (Figure 2-11) indicates increased cellular viscosity beyond this speed. This outcome suggests that if a naïve T cell hypothetically desires to move faster than 10 μm/sec, it will face a dramatically increased

resistance that may negatively impact its migration. The cellular components responsible for this altered viscous behavior cannot be identified from the current study. In fact, the sources of cell viscosity are not fully understood. The contributing cellular components can be of a flow-dependent origin, such as fluid viscosity and fluid-solid interactions, and/or of a flow-independent origin, such as the viscosity of the cytoskeleton and the membrane [142, 164, 165]. One or more of these factors could have contributed to the observed transition in this case.

One of the three characterizing symptoms of the WAS disease is systemic immunodeficiency. The ability of WAS-/- T cells to perform directed cell migration (chemotaxis) was shown to be impaired [19, 20, 166], but the physical origin of this behavior is unknown. This work provides evidence that the defective migration may be caused by a mismatch of the cells' mechanical properties with those of WT cells. We showed through micropipette aspiration studies that naïve WAS-/- T cells had an average apparent Young's modulus of 190+/-69 Pa, about 53% smaller than the 290+/-102 Pa determined (see the previous section) for their WT counterparts. After activation, the stiffness of WAS-/- T cells decreased to 121+/-41 Pa, roughly 57% lower than before. However, this reduction is less than half of the modulus reduction found previous for WT T cells upon activation.

AFM cell indentation experiments showed that the rise of the modulus with indentation speed for naïve WAS-/- T cells was similar to that for naïve WT T cells. This result may be interpreted as increasing the migration speed of these two populations will

lead to a similar increase in the viscous resistance they experience. Inspection of the viscous responses of activated WT and WAS-/-T cells unveiled a steady elastic modulus increase in the former, but the latter maintained its modulus around 130 Pa despite a two orders of magnitude rise in the deformation speed, then abruptly increased this value to approximately 220 Pa at the highest speed tested. As cells are viscoelastic materials whose viscous nature makes them appear stiffer at higher deformation rates, the lack of variation in the modulus of activated WAS-/- T cells indicates minimal viscous contribution to the measured cell stiffness. Since this pattern was not observed in activated WT T cells, the present finding suggests that the cellular components and/or mechanisms responsible for bringing forth normal viscous responses at low deformation rates may be deficient and/or defective in activated WAS-/- T cells.

Results from this work confirmed the hypothesis that WT and WAS-/- T cells have dissimilar mechanical properties. WASp is a multi-modular protein that contains binding sites for both actin monomers and the Arp2/3 complex, which attaches to existing actin filaments and acts as a nucleation site for actin branching [167], and thereby facilitates the interaction of these molecules. Thus, a possible explanation for the 53% modulus difference between naïve WT and naïve WAS-/- T cells is that WASp deficiency reduces and disrupts actin polymerization and branching, resulting in an incorrectly organized, insufficiently cross-linked actin network that is less stiff. This idea seems to be supported by the study of Gallego and colleagues [166], who compared the cytoskeletal responses of WT and WAS-/- T cells during cell activation. They observed that five minutes

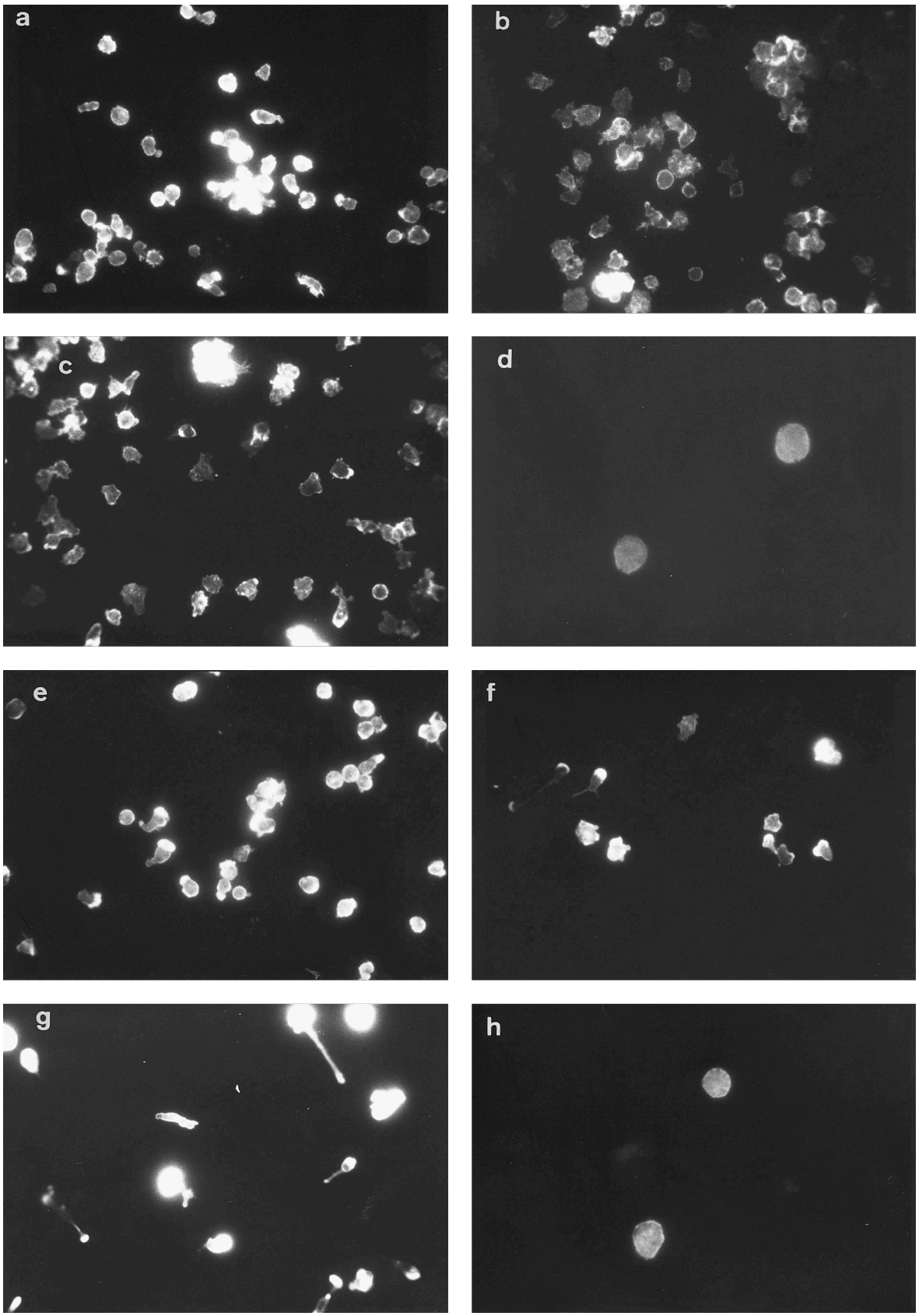
a
b
c
d
e
f
g
h

Figure 2-17: Actin reorganization in normal and WASp-deficient T cells in response to anti-CD3 antibody stimulation. After 5 minutes, F-actin both distributes throughtout the cytoplasm and concentrates in a ring next to the cell membrane of normal T cells (a). Actin remodeling proceeds gradually, resulting in the spreading of the cells and generation of attachment pseudopods 15 (b) and 30 (c) minutes after stimulation. In contrast, some WASp-deficient T cells begin to display cellular poles enriched in actin after 5 minutes of antibody treatment (e). After 15 minutes, this actin polarization is widely observed (f and g), and the cells adopt abnormal morphologies and are less able to spread. Cells pretreated with cytochalasin D show no CD3-mediated shape change (d and h). Figure from Gallego *et al.* [166].

after the application of the anti-CD3 antibody, F-actin was diffusely distributed throughout the cytoplasm of WT T cells although a much higher, ring-shaped expression was found next to the cell membrane (cortical actin) (Figure 2-17 a). Cell spreading progressed gradually, with appearance of pseudopods between 15 and 30 minutes into stimulation (Figure 2-17 b and c). In contrast, five minutes of antibody exposure induced actin-ring formation in some WAS-/- T cells but caused actin clustering and polarization in others (Figure 2-17 e). Generation of these cellular poles was widely observed after 15 minutes, and little cell spreading took place (Figure 2-17 f and g). Importantly, pretreatment of cells with cytochalasin D that inhibits actin polymerization abrogated all the above changes, demonstrating directly that the actin cytokeleton was responsible for the abnormal cell spreading and polarization observed in WAS-/- T cells (Figure 2-17 d and h).

Since actin is critically involved in T cell activation [17, 109], a defective actin network may also impede optimal activation of WAS-/- T cells and thus explain the presently observed smaller reduction in their apparent Young's modulus upon activation compared to their WT partners. A prior work showed that Vav1-deficient thymocytes exhibited impaired inactivation of ERM proteins, which anchor the plasma membrane to

the cortical actin cytoskeleton, upon T cell activation via CD3 conjugation [108]. The same experiment also correlated ERM protein inactivation with reduced T cell rigidity, supported by a separate study showing that a smaller contact area was formed between a Vav1-deficient T cell and an APC [168]. Since Vav1 is involved in modulating the reorganization of T cell actin cytoskeleton just like WASp, another possible explanation for the smaller modulus reduction in WAS-/- T cells upon activation may be reduced cytoskeletal relaxation as a result of partial inactivation of ERM proteins.

Assuming that in order to move normally to execute their biological functions WAS-/- T cells should travel in the same velocity range previously estimated for their WT counterparts, 0.23-0.37 μm/sec, naïve WAS-/- T cells would possess an apparent Young's modulus around 220 Pa regardless of the speed variation (Figure 2-13, left panel). In contrast, naïve WT T cells have a modulus of between 264 and 293 Pa. Examination of activated WAS-/- T cells revealed a similar pattern, that their elastic modulus remained around 130 Pa for the particular velocity range (Figure 2-13, right panel), but their WT counterparts exhibit a stiffness between 158 and 167 Pa. The lack of variation of the apparent Young's moduli of WAS-/- T cells in the biologically relevant speed range, regardless of their activation state, leads one to question whether the chemotactic defect of these cells may partly stem from their inability to dynamically change their stiffness during migration. Temporal and spatial variation of stiffness within migrating cells has been demonstrated [100, 169-174]. Microtubules radiating from MTOCs close up into a compact sheath and the cytoplasm-permeating intermediate filament network condenses into a juxtanuclear aggregate, before both components retract into the uropod [84]. A significant

stiffness decrease from 100 kPa to several kPa was estimated to occur in the nuclear region of a fibroblast upon migration [169, 175]. Stiffness alteration of motile leukocytes is also implicated in the immunocytochemistry work of Wolosewick, who showed that the distribution of actin in transmigrating leukocytes varied temporally, with sequential detection of actin in a cell anterior podosomal structure early into dispedesis, in the caudal region where the cell is constricted by an intercellular opening, and finally in the posterior region [95].

The extravasation of T cells at their target tissues critically depends on chemokines [110]. As introduced in Chapter 1, chemokines promote both T cell adhesion and diapedesis during the extravasation process. Even though it is known that chemokines promote T cell transmigration by modulating the cell's cytostructure (Figure 2-16, d-f) [110], these changes have not been directly linked to any mechanical properties of T cells. Based on the observation that T cells with deficient actin regulation (WAS-/-) demonstrated impaired chemotaxis in transwell migration assays [19, 20], the most obvious mechanical property to investigate is the cell stiffness. Micropipette aspiration experiments were conducted and determined an average apparent Young's modulus of 128+/-33 Pa for naïve WT T cells that migrated in response to the chemokine CCL19, a dramatic reduction from the 290+/-102 Pa before stimulation. This result suggests that chemokines promote dispedesis of T cells by increasing their compliance so they can easily reshape to accommodate environmental constraints. This modulus decrease agrees with the prior finding that chemokine binding triggers the release of ERM proteins in T cells, detaching the plasma membrane from the cortical actin cytoskeleton and thus fluidizing

the former to increase cell deformability [111]. Activated T cells have higher motility than their naïve counterparts, and we showed in section 3.4.3 that the former is about two times more compliant. In this work, we showed that transmigration corresponded to stiffness reduction. Taken together, these results suggest that modification of the cellular elasticity may be a general requirement for T cell migration.

WAS-/- T cells display impaired chemotaxis even though their expressions of adhesion and chemokine receptors were found to be normal [20]. This result and the present discovery that the stiffness of WT T cells was reduced in response to chemokines together raised the question of whether the defective migration of WAS-/- T cells could be partially caused by insufficient and/or ineffective modulation of cell elasticity in the absence of WASp. Transwell migration experiments showed a statistically insignificant ($p > 0.05$) change in the modulus of these cells upon chemokine stimulation. This outcome supports the hypothesis that WAS-/- T cells are less capable to migrate because of inappropriate adjustment of cellular deformability.

Since T cells play a critical role in adaptive immune responses, understanding their mechanical properties that affect their migration is extremely important. Knowledge of T cell deformability may provide insights to current controversies connected to the cells' migration process. For example, these cells are known to transmigrate into tissues via both the transcellular pathway and the paracellular pathway [66]. It is still under debate whether one pathway is preferred over the other, and whether the selection could be specific to the T cell subtype (naïve, activated, memory). A detailed characterization of the

mechanical responses of these cells may help clarify these issues. Quantitative measurements of the mechanical properties of T cells can be used for simulation of T cell biomechanical behaviors that may reveal rare cell phenomena not easily detected during experiments, as well as allow predictions of cell responses under abnormal circumstances, such as in T cell diseases. One such disease that was specifically investigated in this study is WAS. The pathogenesis of the immunodeficiency phenotype of this disease has been partially attributed to impaired homing of immune cells in vivo, but details on why and how this defect arises are still missing. However, Haddad and coworkers demonstrated the importance of this information by showing that abnormal chemotaxis of T cells from WAS patients correlated with the severity of the disease in these individuals [74]. Knowledge of how the mechanical properties of WAS-/- T cells differ from those of WT T cells may lead to a better understanding of the homing defect, which in turn may help design better or new treatment regimens for the disease.

Despite the precautions taken to ensure the health of the cell subjects, we could not rule out the accidental inclusion of dying T cells, which stained faint blue by the trypan blue dye and were hard to identify under a microscope. This population could perhaps account for some of the data scatter. In addition, samples of activated T cells always contained a heterogeneous size distribution that reflected the different phases of the cell cycle that the cells were in. For testing we selected cells of the average size, which were also the most abundant population in the sample. This selection could have favored cells in a particular stage of the cell cycle and should be kept in mind when comparing results from this study with other works.

Model selection

Research work on neutrophils demonstrated that these cells mechanically behaved like a liquid [84, 88, 176], and a few studies that investigated leukocytes in general also used a liquid model to describe the cell's mechanical characteristics [176]. However, it is a well-established observation that naïve T cells typically have a large nucleus enveloped in a thin layer of cytoplasm [177], and the cytoplasm to nucleus ratio of these cells increases when they become activated. Furthermore, a more recent study by Rosenbluth *et al.* showed that the Hertz solid model generated a better fit for their AFM indentation data on naïve T cells than did the liquid droplet model [138]. Considering this information, solid models compatible with the micropipette aspiration and AFM techniques were selected to fit the experimental results of the present work. The cell subject was assumed to be a linearly elastic material, the simplest mechanical characterization of a solid, with the intention of starting with a simple model to see whether it would delineate the essence of T cell behaviors before considering models that are more complex. For the two techniques, the choices are respectively the half-space model and the Hertz model, with the latter having been successfully applied to describe the apparent elastic modulus of a wide range of cell types including muscle cells, lymphocytes, breast cancer cells and endothelial cells [138, 162, 178, 179]. In order to satisfy the assumption of the Hertz model that the cell appears as a semi-infinite solid to the indenter, a pyramidal AFM probe was chosen at the expense of probing only localized cell stiffness that may not reflect the bulk stiffness of the cell. Five

to ten indentation curves were collected for every cell as an attempt to reduce the effect of local heterogeneity on the calculated apparent Young's modulus.

Despite the unrealistic assumptions the half-space model and the Hertz model make treating a cell as a homogeneous, isotropic, and linearly elastic solid, which obviously oversimplify the complex intracellular composition and structure of a real cell, these simple models were able to fit the data from naïve T cells very well (Figures 2-8, 2-10). The half-space model appeared to still generate good fits for micropipette aspiration data from activated T cells, but we observed that the AFM data from about 30% of the activated T cells, from both WT and WAS-/- mice, could not be satisfactorily described using the Hertz model. Instead of a smooth transition from the non-contact to the contact portion of the retraction curve, these incongruent cells displayed a 'kink' at the transition similar to that shown by Rosenbluth *et al.* as arising from a liquid-like behavior (Figure 2-18) during their comparison of the solid Hertz model and the liquid droplet model for fitting their AFM indentation results from HL60 cells, Jurkat cells, and human neutrophils [138]. As discussed earlier in this section, these cell types have similar properties as those of T cells. Rosenbluth *et al.* concluded that all three cell types were better described by the solid model, which is what we also observed in this study for the non-activated (ie, naïve) T cells. It is not surprising that activated T cells have a more fluid-like nature than their naïve counterparts since they have a higher cytoplasm to nucleus ratio.

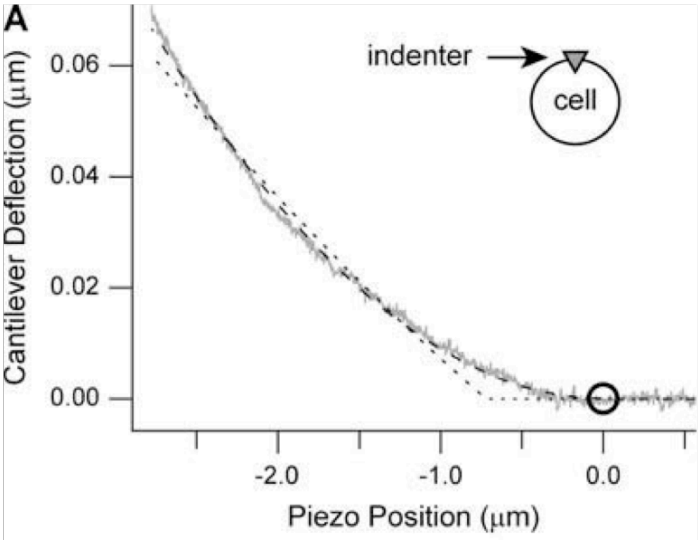

Figure 2-18: Comparison of the fitting of a representative cell indentation curve of the HL60 cell obtained via AFM. This figure is adapted from the work of Rosenbluth *et al.* [138]. The solid gray line is the actual experimental variation of the deflection of the AFM probe as the probe indents further (from positive to negative piezo position) into the cell. The dashed black line is the fit of the experimental curve to the solid Hertz model, and the dotted gray line is the fit using the liquid droplet model.

The fact that the majority of the activated T cells did not display the fluid-like characteristic suggests that this feature may reflect a different stage of the cell cycle, or it may be a result of a different degree of cell activation. This phenomenon has been reported by Tsai *et al.*, who observed variation of the apparent viscosity of the HL60 cell, a human myeloid leukemic cell line resembling immature neutrophils, during the cell cycle and process of maturation [180, 181]. HL60 cells induced to mature yielded a viscosity of 220 Pa·s in the G1 stage of the cell cycle. This value rose to 400 Pa·s for the S stage before approaching 130 Pa·s, the apparent viscosity of neutrophils, seven days into the maturation process. It may be interesting to determine whether the observed cellular fluidity has an impact on the migration capacity of activated T cells. The 30% of cells that did not fit the Hertz solid model were not included in the results presented in this thesis work. The

present finding reveals that a simple solid model does not entirely capture the elastic response of activated T cells. Instead, a model that incorporates both the solid and the liquid feature should be considered.

Chapter 3 Determination Of TCR-pMHC Dissociation Rate Using Dynamic Force Spectroscopy

3.1 Background

The recognition and conjugation of T cell receptor (TCR) to peptide-MHC (pMHC) is central to the development and activation of T cells, as well as to the homeostatic maintenance of the T cell pool in the periphery. Thymocytes (immature T cells) with TCR that can bind to self pMHC (spMHC) on thymic stromal cells are positively selected but those that bind strongly to either self MHC or spMHC are deleted, resulting in a T cell repertoire that interacts weakly with antigen-presenting cells (APCs) (Figure 3-1) [182]. Mature T cells interact with APCs in secondary lymphoid tissues and become activated when their TCR detects antigenic pMHC complexes. In the periphery, maintenance of the structural diversity (collection of different TCR specificities) in the naïve T cell pool requires naïve T cells to come physically close to APCs and bind their surface spMHC ligands to stay alive (Figure 3-2) [35, 183], with cells without adequate access to this resource maintained at low copy numbers. Naïve and memory T cells with the same TCR type also compete for spMHC to maintain balance between the two compartments in the periphery [184, 185].

In order to fully understand these phenomena, it is essential to study the interaction of TCR with pMHC at both the molecular and the cell level. A T cell can be activated when its TCR binds antigenic pMHC on an APC, which displays different types of

peptides at different copy numbers (Figure 3-3). This binding results in the formation of an immunological synapse (IS) that contains

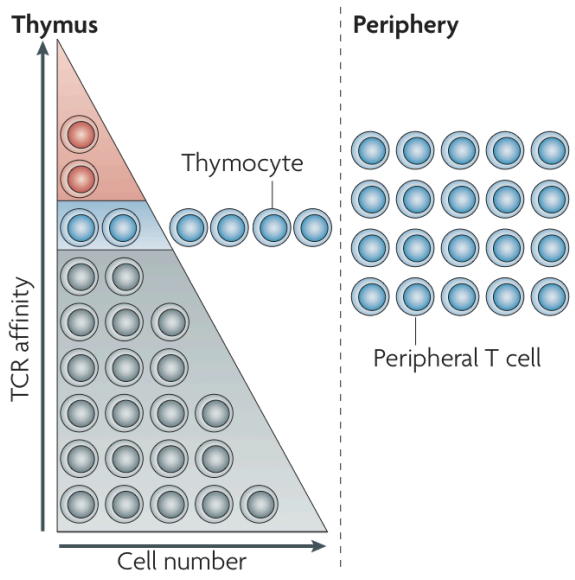

Figure 3-1: Selection of thymocytes during T cell development in the thymus. Most thymocytes display TCR that binds spMHC with very low strengths, or affinities (grey cells). These cells are eliminated from the potential T cell pool by death by neglect. Those that bind spMHC with high affinities (red cells) are negatively selected. Only thymocytes that bind spMHC with intermediate affinities (blue cells) are permitted to mature into adult T cells, which are subsequently released into the periphery. Illustration from Palmer and Naeher [182].

numerous TCR-pMHC complexes. Peptides can be categorized based on the T cell responses they induce. Those that are able to produce T cell activation are called agonists. Depending on the magnitude of the cell response, agonist peptides can be further classified as strong and weak [182]. Because the peptides presented on the surface of an APC embody a spectrum of activating potency, a T cell must be able to integrate multiple and possibly competing signals from the TCR-pMHC complexes at the T cell-APC interface and generate a net biological outcome.

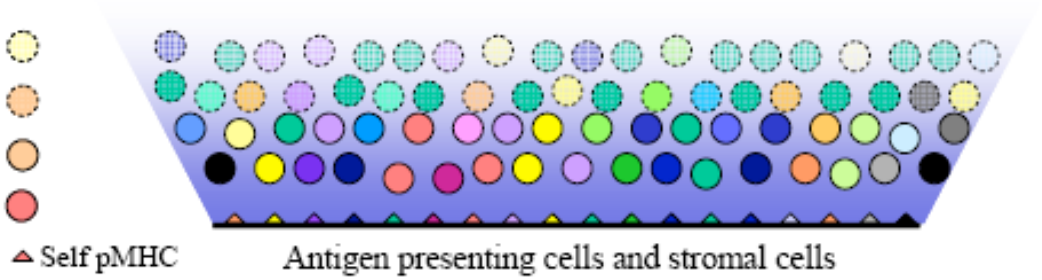

Figure 3-2. T cell clones bearing different TCR types compete for both pro-survival cytokines and spMHC ligands displayed on APCs and stromal cells. The circles represent T cell clones, with the solid and broken boundary representing those maintained at high and low copy numbers, respectively. The triangles designate the set of spMHC complexes that can be recognized by the T cell clone of the same color. The intensity of the background specifies the concentration of cytokines, cell-signaling molecules secreted by numerous cell types of the immune system, decreasing from bottom to top. Illustration from Vinay *et al.* [35].

The strength of binding between a TCR and a pMHC is conventionally measured in terms of their affinity for each other. When a chemical reaction is written to describe the formation of a TCR-pMHC conjugate:

$$\text{TCR} + \text{pMHC} \underset{k_{off}}{\overset{k_{on}}{\Leftrightarrow}} \text{TCR/pMHC conjugate} \qquad (3.1)$$

affinity, designated as K_D, is the equilibrium dissociation constant of the reaction given by the expression:

$$K_D = \frac{k_{off}}{k_{on}} \qquad (3.2)$$

where k_{on} (in units of $s^{-1}M^{-1}$) and k_{off} (in units of s^{-1}) are the rate of association and dissociation of the binding process, respectively. When multiple pairs of TCR and pMHC are considered, the binding strength that results is called avidity. While TCR-pMHC affinity has been extensively studied, substantially less information is available on TCR-pMHC avidity. It has been suggested that there exists a threshold avidity above which T cells are activated, and whether this threshold can be reached depends on the cumulative consequence of all the TCR-pMHC interactions that a T cell senses [47-49, 186-188].

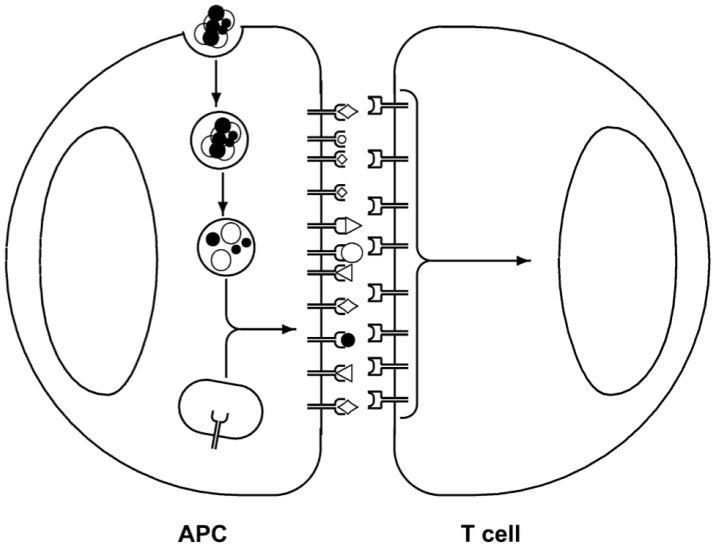

Figure 3-3: Interaction of TCR with pMHC at the T cell-APC contact site. An APC takes up proteins and degrades them into peptides, forms peptide-MHC complexes, and displays these complexes on its surface. Various peptides are presented at different copy numbers to the T cell, and some of them are recognized and engaged by the cell's surface TCRs. This engagement generates intracellular signals that are integrated by the T cell, which decides on a response based on the net signal. If enough TCRs are triggered the cell becomes activated. Illustration from van den Berg and Rand [49].

One paradox in the study of T cell recognition of antigen was how these cells detected rare antigenic pMHC ligands among a sea of endogenous pMHC on the surface of APCs, and how many TCR-pMHC pairs are needed to generate an activating signal. Studies

investigating TCR specificity for antigen showed correlation of the interaction strength of TCR with pMHC with the consequent biological response induced in the T cell. However, whether the response is governed by the affinity (K_D) or the dissociation rate (k_{off}) of the conjugate remains a controversy not completely resolved. Many studies found correspondence between increasing affinity and increasing potency of the pMHC ligand to activate T cells [36-38, 189, 190]. However, other works found TCR-pMHC combinations that did not conform to this pattern. Examination of these cases suggests dependence of T cell responses on the dissociation rate of the conjugate [40-42]. The model most widely accepted to explain the influence of k_{off} on the specificity of T cell recognition of antigen is the kinetic proofreading model [42], which suggests that the full activation machinery is assembled in stages so a pMHC ligand must occupy a TCR for sufficiently long (ie, small k_{off}) to complete the assembly. A weak ligand with a short half-life ($t_{1/2}$, where $k_{off} = \ln 2/t_{1/2}$) unbinds from a TCR quickly, resulting in insufficient time to carry out the series of events necessary for T cell signal transduction, including TCR clustering, phosphorylation of the ITAMs of the CD3 complex, recruitment and activation of the tyrosine kinase ZAP-70 (Chapter 1, section 1.1), and compartmentalization of signaling molecules [191]. In contrast, a potent ligand has a long half-life and stays engaged to a TCR long enough to accomplish these events. This mechanism enables a TCR to differentiate rare agonist pMHC ligands from the abundant spMHC ligands surrounding them. Imaging experiments that showed an APC serially engaged by multiple T cells [192] led to the proposal of the serial triggering model [193], in which binding between a TCR and a pMHC complex must be sufficiently short to allow a TCR to rapidly sample an array of pMHC complexes. These two models together imply that a window of optimal k_{off} exists, characterized by a Gaussian

distribution around k_{off} values that promote T-cell activation and outside of which non-optimal T cell activation results [194, 195]. Although this idea is supported by some studies [195, 196], results from work involving high-affinity TCR mutants contradict it. The latter found that the activation capacity of the T cells bearing these TCR mutants was unaffected by the affinity increase [53, 197, 198].

Work conducted to investigate T cell detection of antigen uncovered surprisingly high sensitivity. Irvine *et al.* demonstrated that a CD4+ T cell could respond to as few as a single agonist pMHC ligand [43]. The same study found that about 10 and 25 TCR-pMHC conjugates were needed to form an interface structure resembling that of a IS in the presence and absence of the CD4 coreceptor, a result in agreement with the facilitative role of the coreceptor in antigen sensing by T cells [65, 199, 200]. A subsequent study by Purbhoo *et al.* using CD8+ T cells revealed the same single-antigen sensitivity [44]. This study also found that neither complete activation nor a stable IS was necessary for cytotoxic T lymphocyte (CTL) cytotoxicity, as only three pMHC complexes were needed to induce target cell killing. The extremely high sensitivity of T cells suggested by these findings was surprising considering how weak a TCR-pMHC bond is. An early study looking at the interaction of 5C.C7 TCR with MCC-E^k and a related system, 228.5 TCR and MCC(99E)-E^k, showed that the affinity of a TCR for its ligand is in the range 4-6 x 10^{-5} M, about 1000 times lower than the 10^{-8}-10^{-10} M of an antibody that binds large protein surfaces [201]. Subsequent works consistently showed low affinities to characterize TCR-pMHC binding, with K_D values in the 1 to 50 μM range [202, 203]. These results raised the question of how such weak interactions would allow a T cell to efficiently detect antigen.

An explanation started to emerge when the potency of soluble oligomeric pMHC complexes to activate T cells was investigated. The result showed that TCR had to be cross-linked to produce an activating signal, with at least a dimer to generate a productive signaling unit [204-206]. This finding suggests that signal transduction initiated through TCR engagement is not accomplished by individual TCR-pMHC pairs but requires their clustering. The idea that endogenous pMHC might participate in T cell activation surfaced upon observation of their recruitment into the IS mediated through TCR [207]. Subsequent studies showed activation of T cells by soluble pMHC heterodimers carrying both an agonist peptide and an endogenous peptide [45, 46] (Figure 3-4). This finding founded the pseudodimer model for initiation of T cell activation, which suggests that a TCR binding an agonist pMHC ligand recruits a second TCR together with its coreceptor. The second TCR

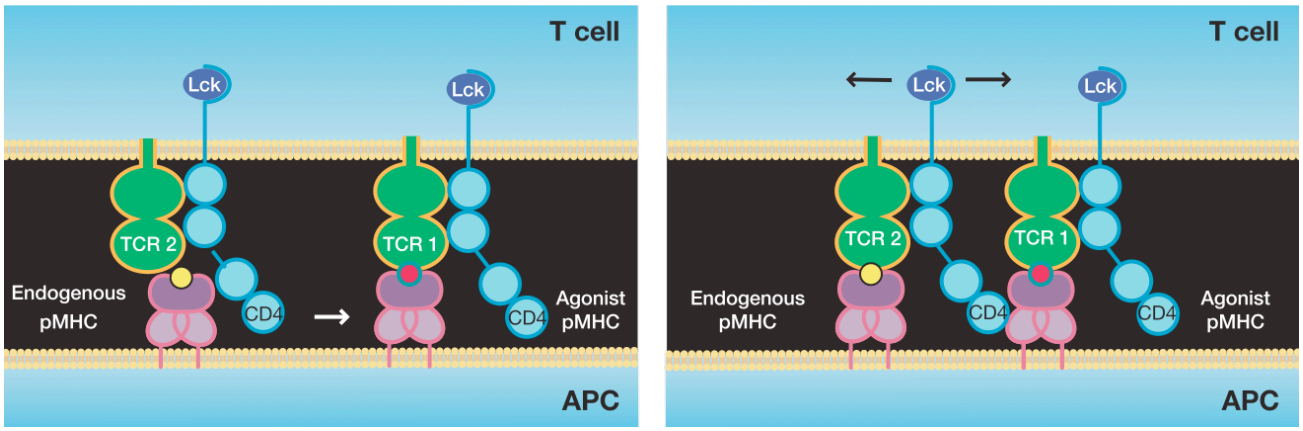

Figure 3-4: Assembly of a pseudodimer structure. Upon binding an agonist pMHC ligand, a TCR (TCR 1) recruits a second TCR (TCR 2) together with its associated CD4 coreceptor. TCR 2 conjugates a nearby co-agonist endogenous pMHC, and its CD4 binds the agonist pMHC engaged by TCR 1. This assembly creates a pseudodimer that initiates an activating signal from the protein kinase Lck on the recruited CD4. Figure from Krogsgaard *et al.* [45]

then conjugates a nearby spMHC unit while its coreceptor binds to the agonist pMHC engaged by the first TCR. This arrangement creates a pseudodimer that triggers the activation cascade starting from the protein kinase Lck on the recruited coreceptor (Figure 3-4). A key prediction of this model is that the co-agonist capability of spMHC ligands that leads to enhanced T-cell sensitivity would be most prominent at low concentrations of agonist complexes. Experimental results show good applicability of the pseudodimer model to CD4+ T cells but only partial validity in cases involving CD8+ T cells (reviewed in REF. 208). One explanation for this discrepancy was suggested to be the different affinities of the CD4 and CD8 coreceptors for MHC, with the former estimated to be at least 25-fold lower than the latter [209]. The observation that endogenous pMHC ligands can participate in T cell activation makes determining the dissociation parameters (K_D and k_{off}) of these ligands essential to understanding the kinetic basis of their contribution to T-cell sensitivity. However, spMHC complexes in general bind very weakly to TCR such that the dissociation mechanism for some of them cannot be reliably characterized with the currently available methods [194, 208]. Therefore, in order to conduct studies involving these complexes, a technique that is capable of detecting very weak molecular interactions is needed.

The necessity for such a technique is further emphasized in the development of thymocytes, which are selected for maturation by the spectrum of endogenous pMHC displayed on thymic stromal cells. The accumulation of all the individual TCR-pMHC interactions in the thymocyte-stromal cell interface results in a net binding strength that determines whether a thymocyte will die by neglect, be positively selected, or be negatively selected [210]. Those cells that are retained for maturation have affinities that fall within

an affinity window (Figure 3-1) [182]. A study characterizing this affinity window showed it to span about one logarithm and begin roughly three folds below the affinity for negative selection [51]. In the presence of the CD8 coreceptor, an affinity of 6.1 μM was found to separate positive from negative selection [211]. A subtle difference in affinity between a positively and negatively selecting pMHC ligand at the negative selection boundary was discovered to generate different selection outcomes by causing differential compartmentalization of signaling molecules participating in TCR-mediated signaling process [191]. Naeher *et al.* reported an interesting discovery that a 'universal' affinity threshold may exist for the negative selection process of MHC Class I-restricted TCRs. They reacted various class I pMHC ligands with appropriate TCRs and measured similar negative selection thresholds when only the TCR type and both the TCR and the pMHC were changed, as long as the TCR examined remained MHC class I-restricted [211].

Even though immunologists traditionally utilize affinity to compare the selection potency of two spMHC complexes, the retention of thymocytes for maturation really depends on the avidity between their TCR and the spMHC ligands. It has been proposed that there exists a selection threshold above which thymocytes are negatively selected, and whether this threshold could be reached depends on the sum of all the TCR-spMHC interactions that a thymocyte senses. Many studies showed that agonist peptides trigger biological responses in mature T cells tend to negatively select thymocytes, while peptides that positively select thymocytes usually act as antagonists toward T cells [212-214]. However, not all peptides strictly maintain their selecting nature. Administration of a high-affinity pMHC ligand at very low concentrations could result in positive selection [48, 215],

while a high dosage of a low-affinity ligand could cause negative selection [188, 200]. This observation suggests that the fate of a thymocyte depends on the number of TCR occupied by the selecting ligands. This mechanism is described by the occupancy model, which hypothesizes that the engagement of a TCR to a pMHC contributes a certain amount of signaling molecules toward fulfilling a selection threshold, and that if enough TCR is occupied, a positive selection outcome could be converted into a negative one [47, 48, 215]. In this case, weak and strong ligands respectively have low and high affinity [188], and both weak ligands administered at high dosage and strong ligands supplied at a minute amount could positively select thymocytes [48, 188, 200, 215]. The occupancy threshold is thus a product of the ligand affinity and its concentration [48, 215]. The cumulative nature of the selection signal in this case suggests that a very small number of weak ligands could possibly nudge a survival signal into a deleting one at the positive-versus-negative-selection boundary. Thus accurate determination of the binding properties of spMHC complexes is essential to studying thymocyte selection in depth.

Observing that endogenous pMHC ligands play an important role both in the selection of thymocytes for development and in the the sensitivity of antigen detection by T cells, it is essential to be able to measure the weak binding strengths they induce in terms of K_D or k_{off}. These parameters have been measured using competitive binding assays, microcalorimetry, fluorescence activated cell sorting and surface plasmon resonance (SPR) [53, 216, 217]. Being the most widely used technique, SPR offers highly sensitive and label-free detection of adsorbed mass with a resolution of 0.1 pg/mm^2 [218]. It also enables the studying of molecular binding in real-time, thus allowing the binding kinetics to be

revealed. However, measurement with this method becomes challenging when very weak TCR-pMHC interactions, such as those arise in the presence of endogenous peptides, need to be probed. SPR can reliably determine K_D and k_{off} values only within the range of 10^{-11}-10^{-4} M and 10^{-5}-10^{-1} s^{-1}, respectively [57]. In comparison, the interaction of 2C TCR with a spMHC dEV8-K^b yields a K_D of 0.84 x 10^{-4} M [53], a value that approaches the upper limit of the measurable range. Some endogenous pMHC ligands can even generate affinities higher than 300 μM [194, 208]. Moreover, for low affinity interactions such as those with $t_{1/2}$ between 0.3 and 2 sec (k_{off} = $\ln 2/t_{1/2}$), SPR determination of the kinetic parameters requires high protein concentrations, which can raise the background signal and make accurate measurements difficult [194]. Such high concentrations may also cause the association phase of the SPR method to be limited by mass transport of the analyte and the dissociation phase to be disturbed by analyte rebinding, thus underestimating the k_{on} and k_{off} value in the respective scenario [218].

As the techniques currently available for K_D and k_{off} measurements do not have enough sensitivity to resolve very weak binding events, a new methodology capable of detecting minute forces is necessary. Atomic force microscopy (AFM) can be used to measure forces from a few picoNewtons (10^{-12}) up to the microNewton (10^{-6}) range [137]. Forces are sensed by a flexible cantilever, on which a light source is shined and reflected to a photodetector (Figure 3-5). Bending of the cantilever due to a force changes the position of the reflected light on the photodetector, which generates a voltage output proportional

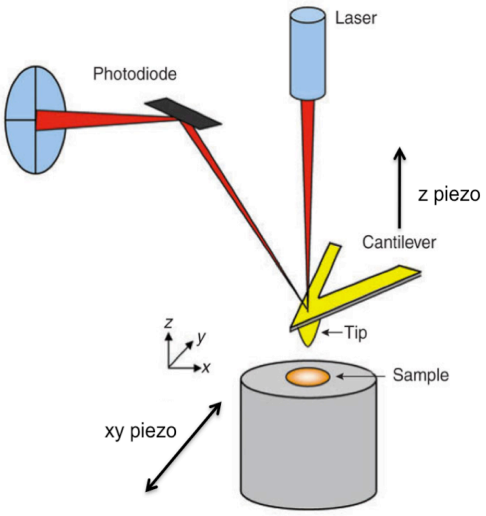

Figure 3-5: Principle of AFM operation. When the interaction of the AFM tip and the sample generates a force that causes the flexible cantilever to bend, the position of the reflected laser beam on the photodiode changes. This position change is converted into a voltage output that is subsequently converted into a force through appropriate calibrations. The x-, y- and z-movement of the tip with respect to the sample are controlled by piezotubes.

to the force. Through a calibration of the displacement of the piezotube that moves the cantilever (which approximates the cantilever deflection) with the variation in the voltage output a deflection value is obtained, which is subsequently multiplied by the cantilever spring constant to yield a force. When an AFM probe is modified to present a biological ligand on its surface, a procedure called functionalization, its contact with a substrate containing the complementary receptor allows the determination of the interaction force between these molecules. Importantly, when this study is conducted for a range of probing rates, a procedure called dynamic force spectroscopy (DFS) [59], the unbinding forces detected can be fitted to a mathematical model to derive a k_{off} value for the ligand-receptor pair under study. Since the unbinding force is the only input and it increases with the loading rate, weak interactions can be effectively 'amplified' if experiments are conducted at sufficiently high testing speeds. Thus, DFS is theoretically capable of measuring very

large dissociation rates, such as those from TCR-pMHC interactions involving self-peptides. This procedure has been successfully applied to various molecular systems across different research fields to divulge their dissociation kinetics [59-64].

The present work investigated the possibility of applying DFS to studying TCR binding with pMHC, with a particular interest on whether the technique could probe extremely weak TCR-pMHC interactions. DFS was first conducted on a receptor-ligand system (ConA and mannose), whose k_{off} had been determined by this method and reported, to validate the experimental setup, testing conditions, and data analysis procedure of the present AFM testing system. This system was subsequently used to measure the unbinding forces between 2C TCR, a CD8+ cytotoxic T cell clone [65], or 2C* TCR, a high affinity variant of 2C TCR [65], and MHC class I K^b conjugated to two peptides, SIRGL and p2Ca, at different AFM retraction speeds. These two peptide were chosen to represent the two ends of a peptide potency spectrum, with the SIRGL peptide inducing strong 2C* TCR-K^b binding and the self-peptide p2Ca inducing very weak binding of 2C TCR and K^b. The forces determined were fitted to the Bell model [219, 220] to derive k_{off} values for the two TCR-pMHC conjugates.

3.2 Methods

3.2.1 Synthesis of pMHCs

MHC Class I K^b heavy chain (HC) and β2 microglobulin (β_2m) were synthesized in *E. coli* hosts. These subunits were harvested and refolded in the presence of a photocleavable 'dummy' peptide (see below). The resultant pMHC complex was subsequently subjected to a peptide-exchange process that replaced the 'dummy' peptide with a peptide to be studied. The final structure of the 'dummy' peptide-conjugated MHC complex is shown in Figure 3-6.

Synthesis of Photocleavable 'Dummy' Peptide

A photocleavable peptide was synthesized by the Biopolymers & Proteomics Core Facility in David H. Koch Institute at MIT via the standard FMOC technology. The original amino acid sequence of this OVA peptide is SIINFEKL, and it was rendered UV light-cleavable by replacing its 4^{th} amino acid residue to the right of the amino terminus with an ANP linker [221]. The presence of the peptide product was confirmed by matrix-assisted laser desorption/ionization (MALDI). Crude peptides (peptide ~75% by weight) were used without high-performance liquid chromatography (HPLC) purification and dissolved in DMSO to make up a stock solution at 30 mg/mL. Aliquots of the solution were wrapped with aluminum foil and stored at -20°C until use.

Synthesis of Photocleavable 'Dummy' Peptide-Conjugated MHCs

LB agar plates with 100 μg/mL ampicillin were prepared, and 10-μL pipette tips were used to retrieve from frozen aliquots and smeared on these plates some *E. coli* that had

incorporated the plasmids for the MHC class I K^b HC and β_2m. These plates were incubated at 37°C overnight for the bacterial colonies to develop. Three colonies from each of the K^b HC and β_2m plates were picked with 10-μL pipette tips, which were then dropped into glass test tubes that each contained 3 mL of LB medium supplemented with 100 μg/mL ampicillin (LB/Amp). The tubes were incubated overnight in a 37°C shaker, after which the content from each tube was added to a 200-mL flask

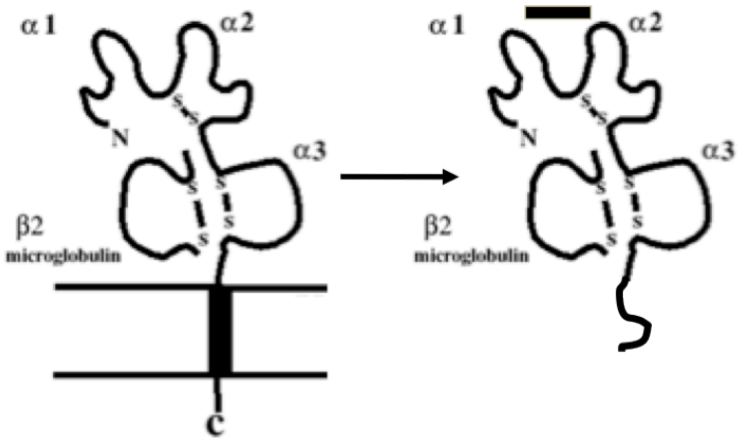

Figure 3-6: Schematic illustrating the structure of the 'dummy' peptide-conjugated K^b. The membrane-bound K^b (left) was rendered soluble (right) by having its transmembrane and cytosolic sequences removed. A photocleavable 'dummy' peptide (see text) occupies the binding cleft. This peptide can be cleaved by UV light and easily exchanged for any peptide of interest. Illustration from REF. 30 and modified.

containing 100 mL of the LB/Amp medium. The flasks were incubated overnight in a 37°C shaker, and the next day their contents were added to 2-L flasks, each containing 900 mL of the LB/Amp medium. These flasks were incubated in a 37°C shaker, and the optical density (OD) of the bacterial suspension was regularly checked until an OD value of 0.8 was reached. At this point, 1 mL of the bacteria culture was collected, and Isopropyl β-D-1-thiogalactopyranoside (IPTG) was added to the flasks to a final concentration of 100 μg/mL

to induce protein production. The flasks were returned to the 37°C shaker for 3 hours, and 1 mL of the bacteria culture was collected at the end. The contents in the flasks were transferred to 500-mL centrifuge bottles and centrifuged in a Beckman CS-15R centrifuge fitted with a FO630 rotor at 10,000 rpm for 30 minutes at 4°C to pellet the bacteria.

The pre- and post-induction samples for both the K^b HC and the β_2m were spun down at maximum speed on a bench-top centrifuge for 10 minutes, the supernatant was removed, and each pellet was resuspended in 25 μL of PBS. 5 μL of a 6x sample loading dye was added to the suspension, and afterward these samples, together with a broad-range protein ladder (New England BioLabs), were ran on a 12% SDS PAGE gel to verify the expression of the induced proteins.

Peptide-bound MHC complexes were prepared following a protocol available on the NIH Tetramer Core Facility web site [222]. After the success of the induction step was confirmed, three bacteria pellets resulting from 3 L of cultures (either K^b HC or β_2m) were resuspended in 60 mL of resuspension buffer, then the suspension was transferred to a polypropylene container and stirred at moderate speed with a stir bar. The bacteria were lyzed by the sequential and drop-wise addition of lysozyme, $MgCl_2$, DNase, Triton X-100, and DTT. The stir bar was removed, and the lysate was placed in a larger polypropylene container filled with ice such that the smaller beaker sat firmly in ice. The lysate was then sonicated for 1.5 minutes at 0.5-second alterations using an ultrasonic converter that was set at power 4. This step was repeated until no obvious viscosity could be observed in the lysate. At this point, the lysate was transferred to centrifuge tubes and centrifuged in a

Beckman CS-15R centrifuge fitted with a FO630 rotor at the maximum speed for 10 minutes at 4°C. After the supernatant was decanted, the pellet was resuspended in 15 mL of wash buffer with a stir rod and sonicated as before using the same setting. The washing and sonication steps were repeated until the pellet appeared white, indicative of the removal of most contaminants. During the last washing step, the pellet was resuspended in wash buffer without Triton X-100, and the suspension was spun down as before. The supernatant was discarded, and the pellet was resuspended in 200 μL of ddH_2O, resulting in the formation of a white paste that contained the inclusion bodies with unfolded K^b HC (or β_2m) proteins. These inclusion bodies were dissolved in 10 mL of urea, and the solution was spun down in a Beckman CS-15R centrifuge fitted with a FO630 rotor at the maximum speed for 10 minutes at 4°C. The supernatant was harvested and stored in a 15-mL polypropylene tube, and the protein concentration in the supernatant was determined using a NanoDrop (Thermo Scientific).

At this point, the MHC K^b protein was refolded with the photocleavable OVA peptide. 500 mL of folding buffer was placed in a 1L glass flask and chilled in a 4°C cold room. A large stir bar was placed in the flask, which was transferred to a magnetic stir plate. Reduced glutathione, oxidized glutathione, and PMSF were added to the chilled folding buffer, followed by the addition of the peptide. Unfolded K^b HC (500 nmol) and unfolded β_2m (1000 nmol) were loaded into two 5 mL syringes using 20-gauge needles. The needles were then switched to 26 gauge needles instead. The folding buffer from before was stirred at a high speed, and as close to the stir bar as possible, the K^b HC and the β_2m were forcefully injected into the folding buffer. The protein solution was incubated

overnight in a 4°C cold room without stopping the stirring, set at 70 rpm. The next morning the unfolded K^b HC (500 nmol) was loaded into a 5 mL syringes with a 20-gauge needle and injected forcefully into the folding buffer close to the stir bar. The folding reaction was continued at 70 rpm and stored in the 4°C cold room until the evening. At this time, the unfolded K^b HC (500 nmol) was again injected into the folding buffer, and the resultant solution was again incubated overnight.

The folding buffer containing the refolded pMHCs was evenly divided among three 250-mL centrifuge tubes and spun down at 13,000 rpm for 15 minutes using a Beckman centrifuge with an appropriate rotor. This step helped to remove any precipitated proteins. The supernatant was collected and subjected to a protein concentration step. Ultrafiltration membranes 76 mm in diameter and made of regenerated cellulose (Millipore) were used together with a concentrator to raise the protein concentration from 0.12 mg/mL to 4.8 mg/mL, and to reduce the volume from 1 L to 25 mL.

The volume of the concentrated protein solution was further reduced from 25 mL to 10 mL using the concentrator. The resultant solution was diluted with PBS to bring the total volume to 100 mL before the concentrator was operated again to bring the volume down to 10 mL. This step was repeated one more time, then the concentrated solution was transferred to a 15-mL tube and centrifuged at 10,000-14,000 X g for 10-15 minutes. The supernatant was collected and poured back into the concentration chamber. After adding 90 mL of PBS to the chamber, the concentration procedure was performed twice, and the final concentrate was pipetted into a 15-mL polypropylene tube and stored at 4°C.

Peptide Exchange

A styroform box capable of fitting a 96-well plate was filled with ice, and a piece of aluminum foil was placed on top of the ice before a 96-well plate was placed on top of the foil. 50 μL of the photocleavable 'dummy' peptide-conjugated K^b (0.32 mg/mL, not purified) and 4 μL of a desired peptide (0.5 mg/mL) were combined in a well and thoroughly mixed by pipeting up and down. The plate was transferred to a UV light chamber that contained a light source at the wavelength of 365 nm. The plate was left in the chamber for 20 minutes to cleave the 'dummy' peptide. The 96-well plate was then removed from the styrofoam box and incubated in a 37°C incubator for one hour. Afterward, the K^b complexes that have been peptide-exchanged were recovered from the wells, centrifuged to remove air bubbles, and stored at -20°C as 50-μL aliquots.

Two peptides were exchanged with the photocleavable 'dummy' peptide. The SIRGL peptide, with the amino acid sequence SIYRYYGL, is a synthetic peptide that strongly promotes the activation of 2C T cells when it is bound to K^b. The p2Ca peptide has the sequence LSPFPFDL and is a degradation product of the murine protein α-ketoglutarate dehydrogenase. It is a self-peptide and behaves like a weak inducer of activation in the 2C system when it is conjugated to K^b.

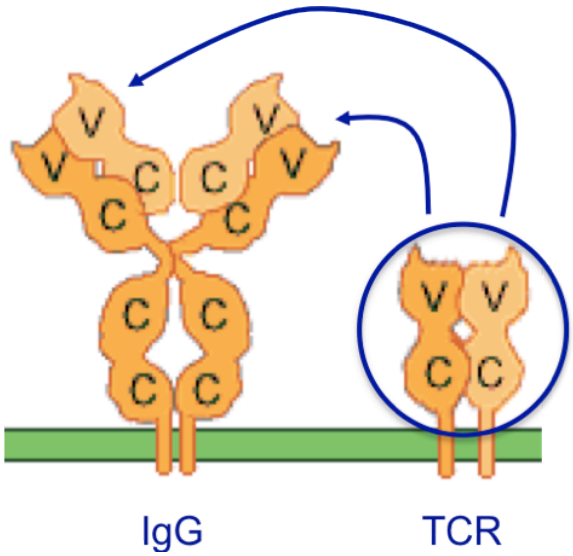

Figure 3-7: Schematic illustrating the construction of the TCR dimer. Two 2C (or 2C*) TCR molecules (right) without the transmembrane and cytosolic sequences were fused to the variable regions of an immunoglobulin G (IgG) molecule (left). The IgG molecule was rendered soluble by removing its transmembrane and cytosolic sequences. Illustration from REF. 223 and modified.

3.2.2 Synthesis of 2C and 2C* TCR Dimers

TCR dimers of the 2C system [224] and a high affinity variant of it, designated as 2C* [65], were made by fusing two TCR molecules to the two variable domains of an IgG1 molecule (Figure 3-7). These dimers were synthesized in insect cells infected with viruses that had been modified to contain the genes for the desired TCR α and β subunits. The genes were cloned into the Baculovirus expression vector system (PharMingen) to express the subunits. TCR proteins were harvested from the culture medium of the cells, purified via protein G affinity chromatography, and dialyzed into PBS. The procedure described here was carried out twice to make 2C and 2C* TCR dimers.

To start, Sf9 insect cells were cultured in tissue culture flasks at 27°C, and the supernatant containing baculoviruses (10^4-10^5 viruses per 100 μL of supernatant) that carried the transgenes for 2C TCRs was added to the flasks. These cells were allowed to proliferate for 2-3 days, and infected cells were identified using a fluorescence microscope as green spots, since GFP was coexpressed within the infected cells. The culture medium of the infected cells, which contained a higher viral titre than the viral supernatant that was used for the initial infection, was collected and used to start another round of infection. This step was repeated a few times to amplify the viral titre to about 2 x 10^8 pfu/mL. Now a large-scale cell culture was initiated at 27°C with an initial seeding density of 5x10^5 cells/mL in 2-L spinner flasks that were kept at ~60 rpm. The high viral titre supernatant was added to the cell suspension when the cell density reached ~2 x 10^6 cell/mL. This was done by removing about 1/8 of the volume in each flask and adding back an equivalent volume of the viral supernatant. Cells were cultured on stirring plates in a 27°C chamber for 3-4 days. The progress of the infection was checked regularly during this period by flow cytometry. When about 90% of the cells in the flasks were infected, contents from these flasks were collected and spun down at 1,200 rpm for 5 minutes.

TCR proteins were purified from the supernatant using a chromatography column packed with 2 mL of protein G-coated Sepharose beads (Sigma). Protein G binds the constant region of an IgG molecule, thus the desired TCR products ended up bound to the beads. A tubing system extended from the supernatant reservoire to the top of the column and from the bottom of the column to the collection bottle. After the column was washed with buffer, the supernatant was flown into the column such that the flow rate at

the end of the collecting tube was approximately 10 drops per minutes, with each drop being 50-100 μL. Afterward, the column was washed extensively with buffer until the absorbance value of the wash at 280 nm wavelength (A_{280}) was less than 0.01. This was done using a NanoDrop. The bound TCR molecules were subsequently eluted by adding elution buffer to the column. The tubing at the bottom of the column was removed, and the eluted proteins were directly collected from the opening of the column and fractionated into 5 1.5-mL eppendorfs. The protein concentration in each fraction was determined with a NanoDrop by measuring the A_{280} value of the fraction. The extinction coefficient of TCR was approximated as 10 so that 1 A_{280} was equivalent to 1 mg/mL.

The eluted fractions were pooled together, and the protein product was dialyzed using Slide-A-Lyzer Dialysis Cassettes (Thermo Scientific) with a MW cutoff of 10,000 Da. The protein solution was carefully injected into a cassette using a syringe and needle, then air was withdrawn from the cassette so the solution could completely wet the membranes. The cassette was sandwiched in a floater, and this assembly was transferred to a 2-L beaker filled with 1.5 L of PBS with the cassette facing down and immersed in PBS. A stirring bar was placed in the beaker, and together with the cassette assembly, the beaker was placed on a stirring plate. With the stirring speed set at 3, the protein sample was dialyzed in a 4^{o}C cold room for three days, with fresh PBS replaced every 24 hours.

3.2.3 Preparation of Samples

TCR dimers and pMHC complexes were bound through poly(ethylene) glycol (PEG) linkers to a glass substrate and an AFM probe, respectively, to be used in AFM studies. This section describes the sequential attachment of the various components. The final molecular configurations on the two surfaces are illustrated in Figure 3-8.

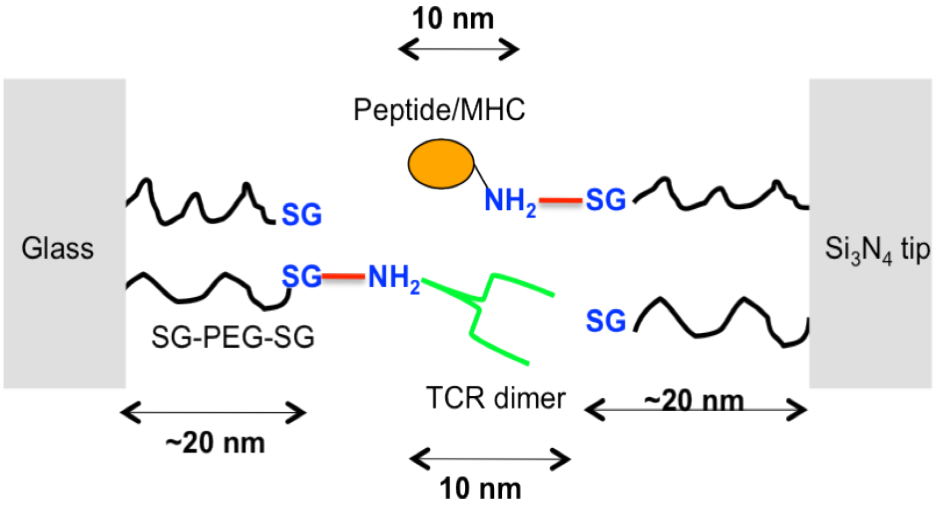

Figure 3-8: Schematic of an AFM probe (right) and a glass substrate (left) functionalized with pMHC and dimeric TCR, respectively. pMHC and TCR are attached to the surfaces using PEG linkers. The approximate length of each molecular component is indicated. The red lines are not physical linkers but illustrate the covalent bonds formed between the indicated chemical groups.

Attachment of TCRs and pMHCs

A silicon nitride AFM probe (Model# TR400PSA, Olympus) was degreased by gently washing it 3 times with chloroform, dried with nitrogen, then plasma-cleaned for 2 minutes. The glass substrate was sonicated in consecutive acetone and methanol baths for 10 minutes each, dried with nitrogen, then plasma-cleaned for 10 minutes. These surfaces were than activated with $-NH_2$ groups by immersion in an aminosilane solution for 30

minutes at room temperature, washed 3 times with methanol, and dried with nitrogen. The aminosilane solution was prepared by combining 47 mL of methanol, 3 mL of water, 500 μL of 3-aminopropyltriethoxysilane, and 3 μL of acetic acid.

SG-PEG-SG (SG = succinimidyl glutarate ester) linkers (CreativeBiochem) of a molecular weight of 3,400 kD were used to tether TCR and pMHC molecules to the NH_2-coated probe and substrate. The surfaces were respectively incubated with 50 μL and 500 μL of 1mM SG-PEG-SG in dry DMSO for 1 hour at room temperature. Afterward, they were washed twice with DMSO and once with PBS, then carefully blotted dry on a piece of kimwipe. At this point, the AFM tip was submersed in 50 μL of 2 μM K^b/peptide and the glass substrate was covered with 500 μL of 5 μM 2C (or 2C*) TCR dimers. Both were incubated overnight at 4^oC and subsequently washed three times with PBS to remove the unbound molecules. The PBS baths used for the AFM probe was supplemented with 200 nM of the same peptide that was bound to K^b. The samples was tested either immediately, or stored in PBS and tested within 24 hours of preparation.

Determination of Molecular Density

A chromogenic reaction as a result of an enzyme cleaving its substrate was used to determine the density of the PEG linkers on a substrate. This protocol was adopted from the work of Riener *et al.* [225] and modified to be used for biotin-PEG-SG linkers.

Generation of Standard Curve

ExtrAvidin-peroxidase (Thermo Scientific) was reacted with its substrate *o*-phenylenediamine·2HCl (Sigma) to produce an orange-brown product. The buffers involved had compositions as follow:

Buffer A: PBS with 0.1% Tween 20

Buffer B: 50 mM citric acid, pH 5.5

Buffer C: Buffer B plus 0.8 mg/mL of o-phenylenediamine.2HCl

Buffer C*: Buffer B plus 0.4 mg/mL of o-phenylenediamine.2HCl

Buffer D: 3% H_2O_2

In order to find the enzyme:substrate ratio that would best resolve the linker density resulting from the functionalization procedure described in section 3.2.3, three sets of experiments that tested different volumes of the enzyme and the substrate were conducted to generate three standard curves:

1st Set:

Blank → 400 μL Buffer C + 4 μL Buffer D

Samples → 10 μL of one of the following ExtrAvidin-peroxidase dilutions + Blank

100 μg/mL, 50 μg/mL, 10 μg/mL, 5 μg/mL, 1 μg/mL, 500 ng/mL, 100 ng/mL, 50 ng/mL, 10 ng/mL

2nd Set:

Blank → 400 μL Buffer C + 2 μL Buffer D

Samples → 10 μL of one of the following ExtrAvidin-peroxidase dilutions + Blank

100 μg/mL, 50 μg/mL, 10 μg/mL, 5 μg/mL, 1 μg/mL, 500 ng/mL, 100 ng/mL, 50 ng/mL, 10 ng/mL

3rd Set:

Blank → 400 μL Buffer C* + 4 μL Buffer D

Samples → 10 μL of one of the following ExtrAvidin-peroxidase dilutions + Blank

100 μg/mL, 50 μg/mL, 10 μg/mL, 5 μg/mL, 1 μg/mL, 500 ng/mL, 100 ng/mL, 50 ng/mL, 10 ng/mL

The working concentration of the ExtrAvidin-peroxidase solution was 100 μg/mL, and this concentration was obtained by diluting the ExtrAvidin-peroxidase stock (2.1 mg/mL) in Buffer A. The reagents were combined in the wells of 48-well plates, and the resultant mixtures were incubated for 30 minutes at room temperature covered with Al foil. Afterward, the absorbance value from each well was read at 490 nm using a NanoDrop.

Determination of Molecular Linker Density

The density of the TCR and pMHC molecules conjugated to sample surfaces was assessed using the ExtrAvidin-peroxidase assay described in the previous section. 10mm x 10mm glass chips were cut out from the same glass substrates that were used to prepare AFM samples, cleaned, and functionalized with biotin-PEG-SG linkers the same way as the glass

substrate. With the availa-bility of an absorbance v.s. ExtrAvidin concentration curve, the density of the PEG linkers on the glass was assessed by reacting ExtrAvidin-peroxidase with the biotin end of the linkers in the presence of the substrate for the enzyme and comparing the absorbance value from this reaction with the standard curve. In order to determine what PEG concentration to use to achieve a single-molecule density, a rough estimation was made as follows. The area of an AFM tip can be esti-mated from its radius to be ~1256.6 nm^2 (area = πr^2, r = 20 nm). The requirement of probing a single molecular pair means the presence of one PEG linker in this area, which corresponds to 7.958 x 10^{10} PEG linkers on a 10 mm x 10 mm chip. Based on this simple calculation, glass chips with three different concentrations of biotin-PEG-SG, corresponded to 1, ~7, and 10 linkers within the contact area of an AFM tip, were prepared and examined.

3.2.4 AFM Experimental System

This section starts with an introduction to the AFM instrument. Then a detailed description of the steps taken to conduct an AFM force spectroscopy experiment, including force calibration, force curve collection, as well as the testing conditions used (temperature, duration), is given.

The AFM Device

The AFM used to conduct the cell indentation experiments was the same device used previously for AFM force microscopy. A detailed description of this system was given in Chapter 2, section 2.2.3.

Experimental Procedure

A glass disc that had been functionalized with TCR dimers was quickly loaded into a fluid cell, and 2 mL of PBS supplemented with 200 nM of the appropriate peptide was immediately pipetted into the fluid cell. An AFM probe functionalized with K^b/peptide was quickly loaded into the tip holder and covered with a drop of the PBS/peptide solution. This solution was then removed, and the tip holder was clamped onto the AFM head, which was quickly inverted and lowered to immerse the functionalized tip in the PBS/peptide solution contained in the fluid cell. The AFM probe was slowly lowered by rotating the thumbwheel on the AFM head until the setpoint was reached, indicating the contact of the tip of the AFM probe and the substrate, before the tip was retracted 5 turns from the surface. At this point, the AFM system was allowed to equilibrate for ~30 minutes for the deflection signal to stabilize.

After zeroing the deflection signal, the tip was engaged and the sensitivity of the probe was determined from a force-distance plot. The tip was then disengaged from the surface, and a thermal spectrum was collected in the testing medium. The AFM software automatically calculated the spring constant of the probe using the sensitivity and the thermal spectrum obtained. For this work, the spring constant ranged 0.17-0.24 N/m,

which was in good agreement with the value (0.20 N/m) quoted by the manufacturer. Force-distance curves were now collected using different combinations of the retract velocity (the speed at which the AFM tip retracted from the substrate), the trigger point, and the dwell time, to try to determine the experimental condi-tions that would reveal the binding of a single pair of TCR and pMHC at a particular retract speed. All experiments were conducted at room temperature using the same approach velocity. AFM force spectroscopy was conducted at random locations on the sample. At each location, 20-30 force-distance curves were obtained, and between 8-12 locations were tested per sample, yielding a total of 200-300 curves for each sample.

3.2.5 Data Analysis

Force-distance curves collected from AFM experiments were analyzed using the computer software MATLAB. The force of unbinding of a TCR-pMHC pair and the point of contact were determined as a result. The unbinding force values obtained at increasing AFM retraction speeds were fitted using the modified Bell model to derive a dissociation rate, k_{off}, for the TCR-pMHC pair under study.

Determination of TCR-pMHC Unbinding Forces

A MATLAB program was written to identify TCR-pMHC unbinding events. The raw data collected experimentally were deflection v.s. LVDT curves, and for all the analyses only the retract portions of the curves were used. The position at which the AFM probe contacted

the sample was deter-mined by performing least-square linear fitting on both the portion of the retract curve 1) when the tip was touching the sample and 2) when the tip was far removed from the sample. For the first scenario, the program started with performing least-square linear fitting on the first 10 data points of the retract curve and outputting an initial error value. This step was repeated, each time including one more data point to the

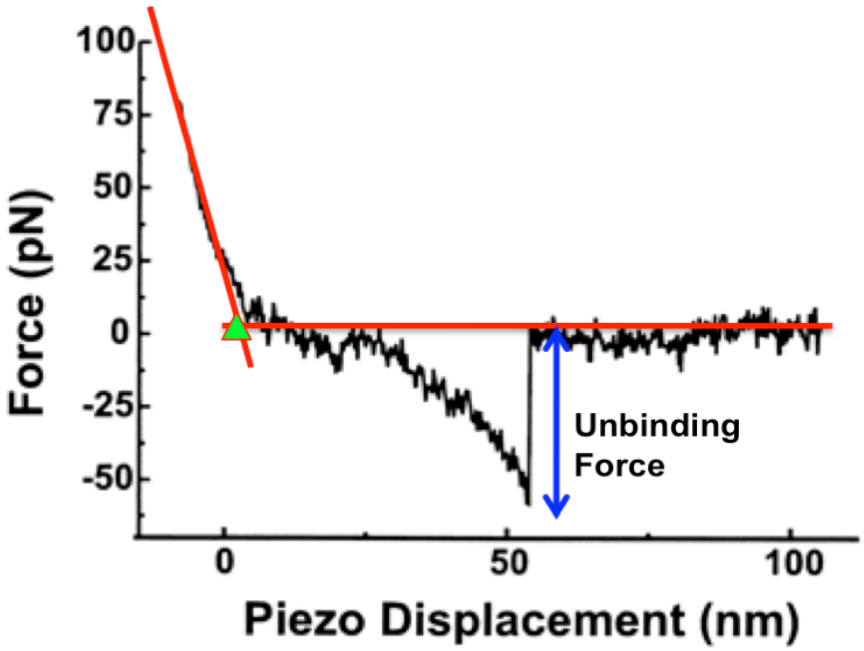

Figure 3-9: Schematic of an AFM retraction curve showing how the contact point of the AFM probe with the sample and the force of an unbinding event are determined. The red lines are linear fits of the pre-contact and post-contact regions of the curve, and their intersection gives the point of contact, labeled by a green triangle. The blue line indicates the force required to unbind a pair of TCR and pMHC.

right, until a user-specified maximum error level was reached. This maximum error varied for different retract velocities and was chosen based on the principle of using the fewest data points to generate a fit that best described the shape of the experimental curve. The same fitting strategy was also used on the second scenario, except that in this case the initial fit was based on the last 10 data points of the retract curve, and every time the fitting

was repeated a point to the right was included. Also, the maximum error for the second scenario was usually different from that of the first scenario. The intersection of the two resultant fits was taken as the contact point of the tip and the substrate (Figure 3-9). The retract curve could be roomed in enough such that both the beginning and the end of a jump in the force value, indicative of a TCR-pMHC unbinding event, could be easily identified. These two points were manually selected, and the difference between their force values equaled the force needed to separate a TCR-pMHC conjugate (Figure 3-6).

Derivation of k_{off} for TCR-pMHC Interaction

The unbinding forces determined for a range of loading rates were fitted to a mathematical model to derive a dissociate constant for the TCR-pMHC pair under study. This model was originally proposed by Bell [219] and further developed by Evans and coworkers [220]. The Bell model observes that the survival time of a bond depends on how fast a force is applied to break the bond. In the absence of externally applied forces, bond dissociation is thermally activated and obeys the relation:

$$k_{off}(0) = \left(\frac{1}{t_D}\right)\exp\left(-\frac{E_b}{k_B T}\right) \qquad (3.1)$$

where $k_{off}(0)$ is the dissociation constant of the bond, t_D and E_b are respectively the characteristic time and energy barrier of dissociation, T is the temperature, and k_B is Boltzmann's constant. The application of a force reduces E_b and facilitates bond breaking.

Under this circumstance, the dissociation of the affected bond is described by the expression:

$$k_{off}(F) = k_{off}(0)\exp\left(\frac{F\chi_\beta}{k_B T}\right) \tag{3.2}$$

where $k_{off}(F)$ is the dissociation constant of a bond in the presence of a force, F is the force exerted, and χ_β is the bond length at the moment of bond breaking. When force is applied at a constant rate, this expression is simplified to the form [220]:

$$F = \frac{k_B T}{\chi_\beta}\ln\left(\frac{r\chi_\beta}{k_{off}(0)k_B T}\right) = \frac{k_B T}{\chi_\beta}\ln r + \frac{k_B T}{\chi_\beta}\ln\left(\frac{\chi_\beta}{k_{off}(0)k_B T}\right) \tag{3.3}$$

where r is the loading rate in N/sec. Therefore, a plot of F versus ln(r) reveals the barriers traversed in the energy landscape along the unbinding pathway. Each barrier governs the unbinding strength of the bond on a different time scale. From this final expression, it is obvious that χ_β can be calculated from the slope of the F versus ln(r) plot. When this plot is extrapolated to cross the y-axis, the y intercept allows the determination of $k_{off}(0)$ when χ_β is known.

In order to use equation 3.3 for this work, r needs to be the instantaneous loading rate, which is the loading rate at the moment of bond breaking, instead of the experimental loading rate. This conversion must be made because the PEG linkers used to

tether the molecules behave like nonlinear springs, so the loading rate changes as the linker is pulled taut during an unbinding event. The instantaneous loading rate is equal to k*r, where k* is the spring constant of the PEG linker/molecule assembly and r is the experimental loading rate. k* is given by the slope of the force-distance plot immediately before a bond breaks.

3.3 Results

3.3.1 Molecular Density Assessment

In order to probe the interaction of a single TCR-pMHC pair, it was necessary to ensure that not more than one bond could be formed within the contact area of the AFM probe and the sample. A chromogenic assay based on the reaction of the enzyme peroxidase and its substrate was used to assess the density of the receptor and ligand on the interacting surfaces. The experiment was designed such that PEG-biotin linkers were attached to a glass substrate following the same chemistry as would be used to prepare real samples, then peroxidase-conjugated avidin was allowed to bind to the biotin. By reacting the enzyme with its substrate and comparing the optical density reading of the resultant colored product to values from known enzyme concentrations, the density of the linkers on the prepared glass surface could be approximated.

A standard curve was first generated by reacting various concentrations of peroxidase with its substrate and reading the resultant color change at 490 nm using a spectrometer (Figure 3-10, Set #1). Observing that the A490 reading was saturated when the logarithm of the enzyme concentration increased above -12.5 and without knowing whether the logarithm of the linker density corresponding to the single-molecule level would be above this value, the amount of catalyst (Set #2) and substrate (Set #3) was varied to try to resolve this region.

A simple estimation described previously in the Methods section showed that the PEG density needed to achieve a single-molecule density with respect to the AFM tip area was 7.958×10^{10} PEG linkers on a 10 mm x 10 mm chip. Based on this result, glass chips with PEG concentrations corresponding to 1, ~7, and 10 PEG linkers within the contact area of an AFM tip were prepared. All three samples yielded a A490 value of roughly 0.2. From the calibration curve (Figure 3-10, Set #3), this number corresponds to a logarithm value of roughly -14. Assuming ExtrAvidin-peroxidase was added in excess of the linkers so that every biotin was bound by one ExtrAvidin, 7.958×10^{10} ExtrAvidin molecules were needed to detect the biotinylated PEGs on a 10 mm x 10 mm chip. Since the ratio of avidin to peroxidase is 0.7 according to the manufacturer, 7.958×10^{10} ExtrAvidin corresponds to 1.137×10^{11} molecules (or 1.888×10^{-13} mole) of peroxidase. The present assay depends on the reaction of peroxidase and its substrate, thus 1.888×10^{-13} mole of ExtrAvidin-peroxidase is needed to detect PEG linkers that are distributed at the single-molecule

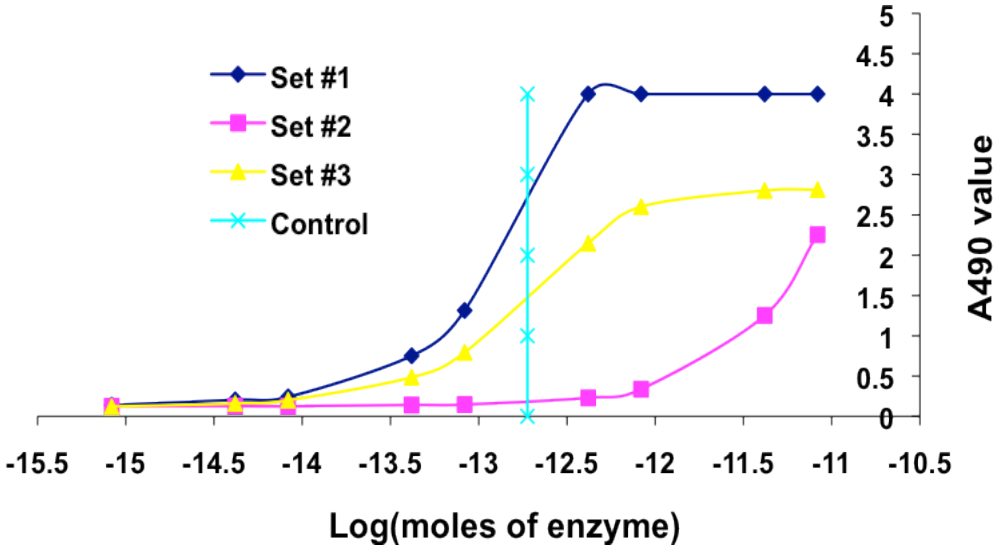

Figure 3-10: Calibration curve of absorbance values from chromogenic reactions between NeutrAvidin-peroxidase and its substrate. Three sets of experiments involving different amounts of the enzyme and substrate were conducted to find the enzyme:substrate ratio that best resolved the linker density resulting from the present functionalization procedure. The Control is the estimated linker density that would yield a single-molecule density (see text).

density. The logarithm of this value is -12.724 (Control in Figure 3-10). To reach -12.724 from -14, the amount of peroxidase (in moles) needs to be increase by about 100 times. Since the ratio of avidin/oxidase is 0.7, the amount of avidin needs to increase by about 70 times in order to bind all the biotin molecules on the 10 mm x 10 mm glass chip. It is unlikely that all the linkers that are incubated on a surface will bind to it, thus all the AFM samples were prepared with a linker concentration that was 100 times higher than the concentration estimated above.

3.3.2 System Validation

Before experiments were conducted to investigate TCR-pMHC binding, it was desirable to validate the AFM experimental system and the data analysis procedure described above using a different receptor-ligand system whose dissociation rate had been determined using DFS. This was done by applying the AFM technique to study the binding of Concanavalin A to mannose, whose k_{off} had been reported to be 0.17 s^{-1} [226]. The unbinding forces of this system at five different retraction speeds were measured and fitted to the Bell model to generate a force-versus-loading rate plot (Figure 3-11), from which a k_{off} of 0.15 s^{-1} was calculated. The comparableness of this value and that reported in the literature suggests that the present AFM technique is robust.

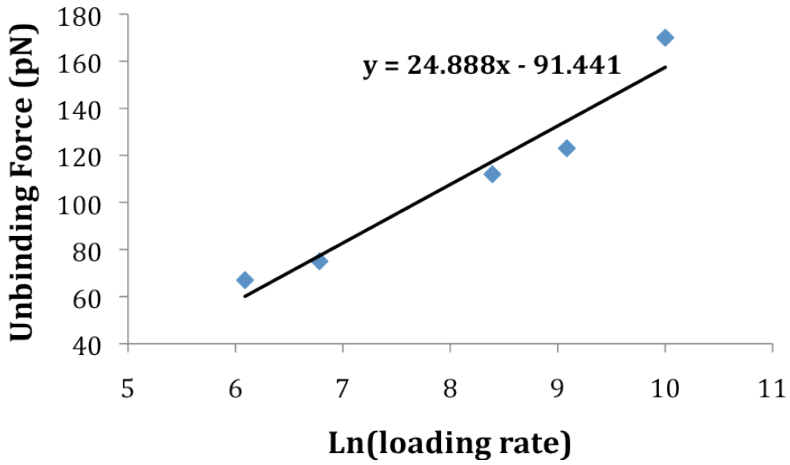

Figure 3-11: Derivation of Concanavalin A - mannose dissociation rate through the Bell model. The unbinding forces measured at different AFM loading rates are plotted against the natural logarithm of the loading rate, and the data points are joined by a best-fit line, whose equation is displayed in the plot. From the slope and the y-intercept of this line, a χ_β and k_{Dim} for the binding pair can be calculated.

3.3.3 Unbinding Force Measurement

In order to derive a k_{off} value for a TCR-pMHC system using DFS, the unbinding force between the molecules needs to be measurable using an AFM. In this work, the interaction force between 2C* TCR dimer and SIRGL-K^b and between 2C TCR dimer and p2Ca-K^b were examined. The affinity and the k_{off} of the former, although with the TCR in the monomeric form, have been determined using SPR and FACS [53] (the 2C* TCR in this study is the m33α TCR in the reference). The affinity of 2C TCR for p2Ca-K^b has been assessed previously, but the k_{off} of this system has not been measured due to the very fast dissociation of the TCR-pMHC complex. This system tests the ability of DFS to determine high k_{off} values that are beyond the sensitivity of the conventional methods such as SPR.

The unbinding forces and their frequencies of occurrence obtained for dimeric 2C* TCR interacting with SIRGL-K^b at AFM retraction velocities of 50 nm/sec, 100 nm/sec, 500 nm/sec, and 1 μm/sec, are shown in Figure 3-12. There is always an inherent spread in the measured force because of 1) dispersive lengths of the PEG linkers, 2) non-orthogonality of the pulling geometry of the tip with respect to the sample, and 3) partial unfolding of the interacting molecules during tip retraction. Force histograms from DFS work are commonly fitted to a Gaussian distribution to obtain peak forces that are regarded as the unbinding forces corresponding to the respective testing speed [194, 220]. However, unbinding events were very rare in the current study, a signature of single-molecule-level detection and possibly also as a result of the non-optimal orientation of the molecular species (see the Discussion section), such that not all the force histograms appear to be Gaussian-distributed. Inspection of the histograms by eye suggests that the most probable unbinding force for the retraction speed of 50 nm/sec falls between 30 and

40 pN. This value increases to 40-50 pN, 70-80 pN and 90-100 pN, when the retract velocity was increased to 100 nm/sec, 500 nm/sec, and 1 μm/sec. However, because of the shape of the force histograms, instead of identifying a peak unbinding force by fitting each to a Gaussian function, the geometric means of the interaction forces measured for each AFM retraction velocity were calculated and assumed to be the unbinding forces. This approach yielded 45+/-18 pN (mean +/- SD), 54+/-21 pN, 81+/-32 pN, and 124+/-62 pN for retraction at 50 nm/sec, 100 nm/sec, 500 nm/sec, and 1 μm/sec, in that order.

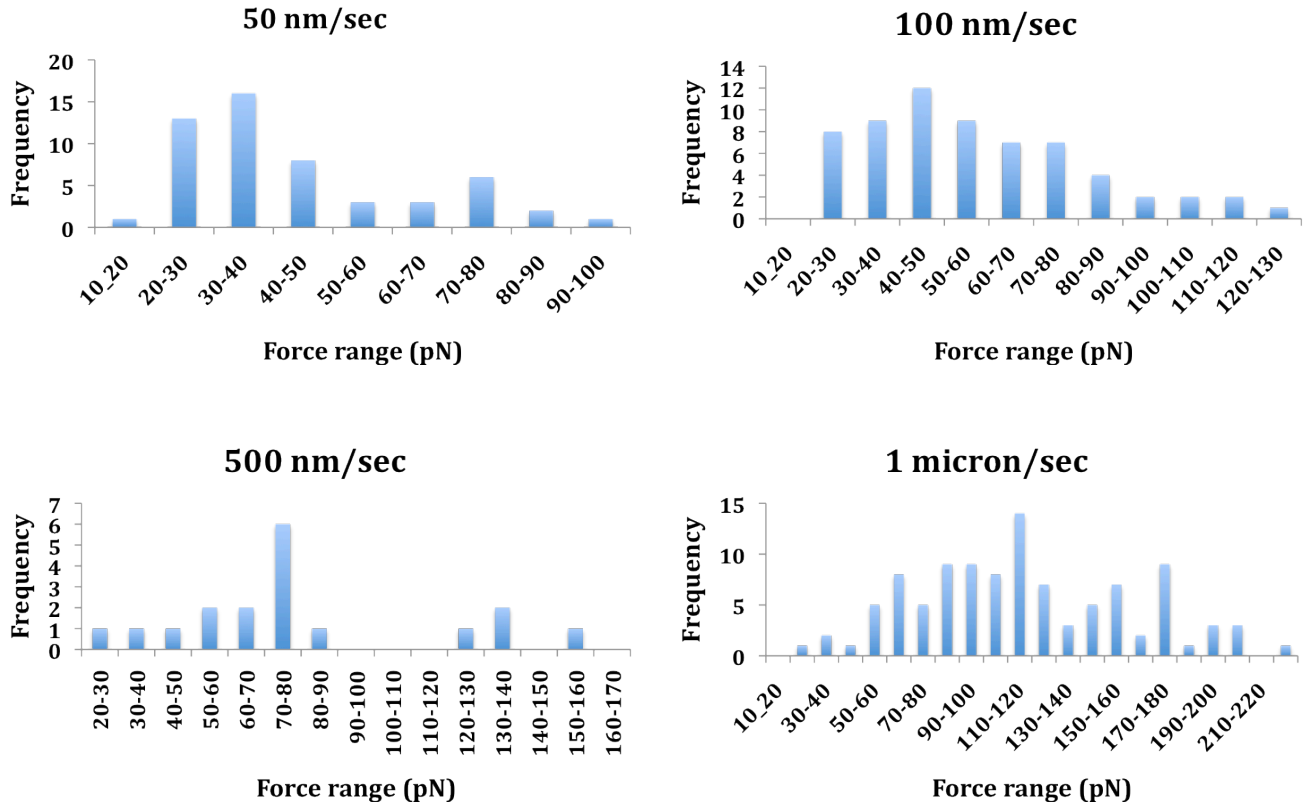

Figure 3-12: Unbinding forces of 2C* TCR dimer from SIRGL-K^b and their occurring frequencies measured at the indicated AFM retraction velocities.

The TCR and pMHC were attached to interacting surfaces via polyethylene glycol (PEG) linkers that were about 20 nm in length. These linkers served two purposes. They

enabled the molecules to orient themselves freely, thus increasing the chance of the molecules' finding the correct binding configuration. In addition, knowledge of the length of the tethers facilitates the exclusion of nonspecific interactions, which usually occur at small intermolecular separations, from the data set. With the identification of the piezotube position at which the AFM probe contacted the sample surface (ie, point of contact), the separation distance between the probe and the sample at which a TCR-pMHC unbinding event occurred could be calculated. This information was determined for all the interaction events observed for the AFM retraction speed of 50 nm/sec, 100 nm/sec, and 1 μm/sec and compiled into a histogram that reveals the distribution of the separation distance (Figure 3-13). Since any specific interactions must happen beyond 40 nm due to the double-tether configuration, separation distances below this value were excluded. The results show that for all three speeds, specific binding events occurred between 40 and 110 nm of separation distances. This pattern suggests that the detected interactions most likely were specific in nature, as nonspecific binding events most likely would result in randomly distributed separation distance values. As the retraction velocity increased, more unbinding events occurred at larger separations. This shift is reasonable since molecules are stretched more at higher loading rates.

The specific nature of the detected binding events was also confirmed by blocking experiments. It was observed that SIRGL-K^b-coated AFM probes blocked with 2C TCR showed almost no interaction with 2C* TCR-coated substrates. The negative controls of experiments involving either no TCR on the substrate or no SIRGL-K^b on the AFM probe also showed no specific interactions.

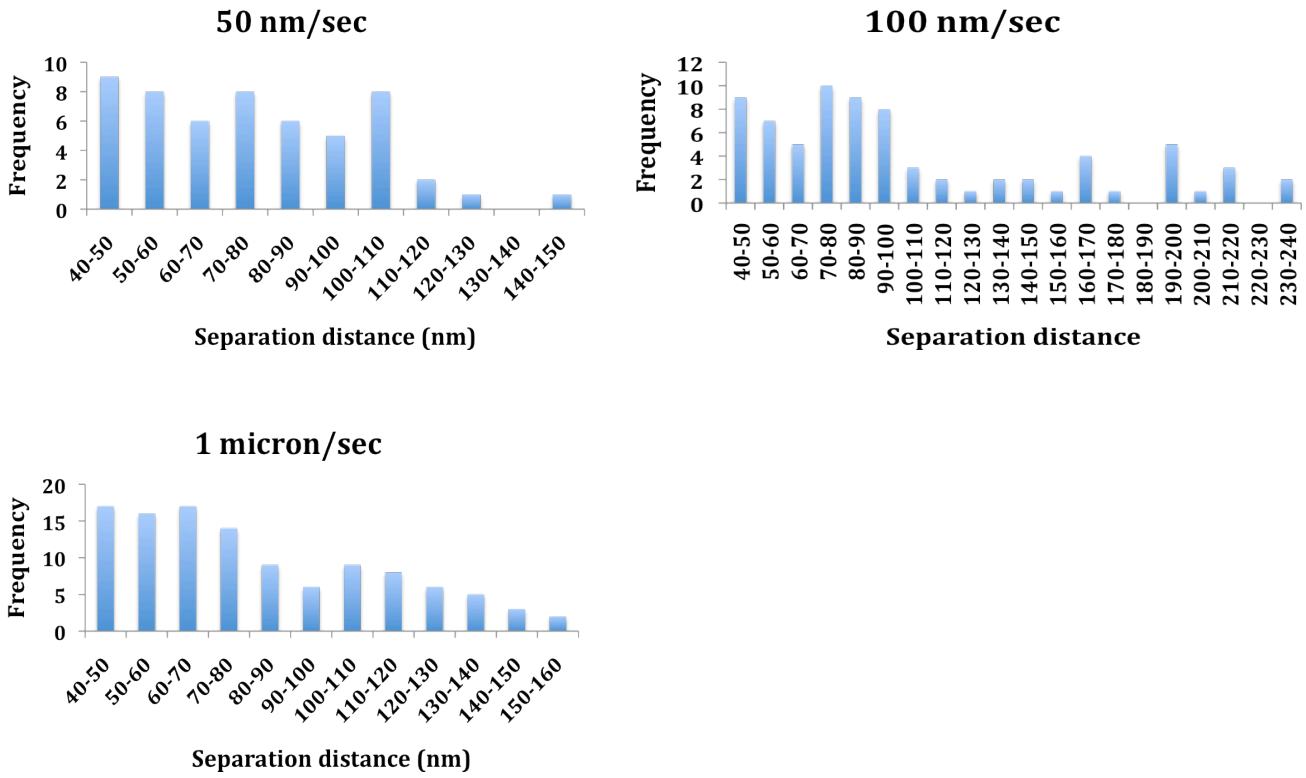

Figure 3-13: Separation distances at which 2C* TCR dimer-SIRGL-K^b unbinding events were detected and their occurring frequencies obtained at the indicated AFM retraction velocities.

The unbinding forces and their frequencies of occurrence were similarly obtained for dimeric 2C TCR interacting with p2Ca-K^b at AFM retraction velocities of 100 nm/sec, 500 nm/sec, 1 μm/sec, and 5 μm/sec (Figure 3-14). When the probe was retracted at 100 nm/sec, between 20 and 40 pN of force was necessary to break a TCR-pMHC pair. This value rose with increasing retraction speeds and was found to be 70-80 pN, 80-100 pN, and 130-150 pN for the velocities 500 nm/sec, 1 μm/sec, and 5 μm/sec in that order. As observed for the interaction of 2C* TCR with SIRGL-K^b, unbinding events were very rare and the force histograms they form also do not appear Gaussian-distributed. Therefore,

instead of identifying a peak unbinding force, the geometric means of the interaction forces measured for each AFM retraction velocity were calculated as before to yield 37+/-26 pN, 97+/-37 pN, 87+/-38 pN pN, and 147+/-84 pN for retraction at 100 nm/sec, 500 nm/sec, 1 μm/sec, and 5 μm/sec.

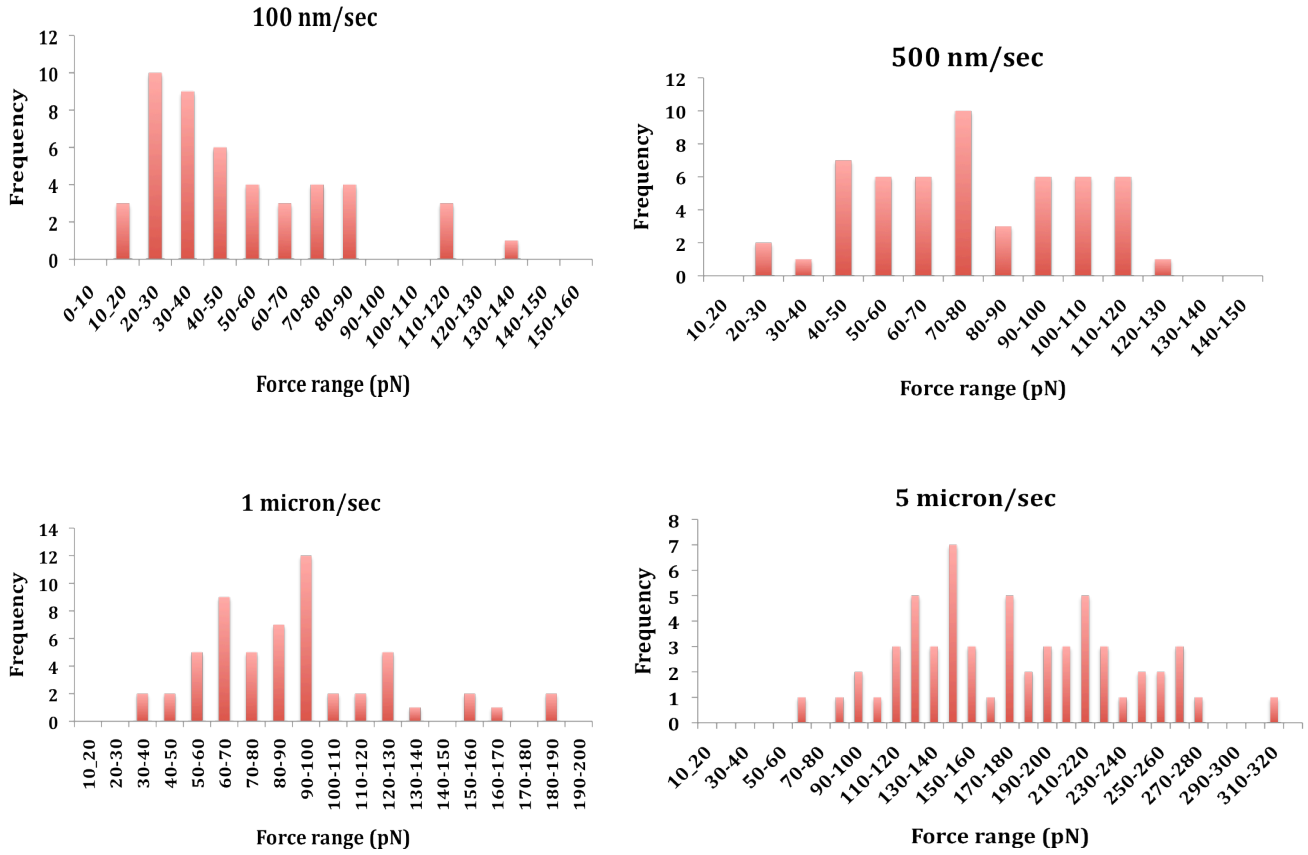

Figure 3-14: Unbinding forces of 2C TCR dimer from p2Ca-K^b and their occurring frequencies measured at the indicated AFM retraction velocities.

3.3.4 k_{off} Derivation From Unbinding Forces

This work assumes a dimeric TCR as a reacting unit and determines a dimeric k_{off}, designated hereafter as k_{Dim}. In order to use the Bell model (equation 3.3), the experimental

retraction speeds were first converted into instantaneous loading rates. The spring constant of the PEG/TCR-pMHC assembly was estimated to be 0.2 pN/nm, and this value converted the four retraction speeds of 50 nm/sec, 100 nm/sec, 500 nm/sec, and 1 μm/sec into loading rates of 10, 20, 100, and 200 pN/sec, in that order. Combining this information with the unbinding forces determined previously at the respective loading rate, 45+/-18 pN, 54+/-21 pN, 81+/-32 pN, and 124+/-62 pN, a plot of the unbinding force against the natural logarithm of the instantaneous loading rate (Figure 3-15) allows χ_β and k_{Dim} to be calculated from the slope and the y-intercept of the plot,

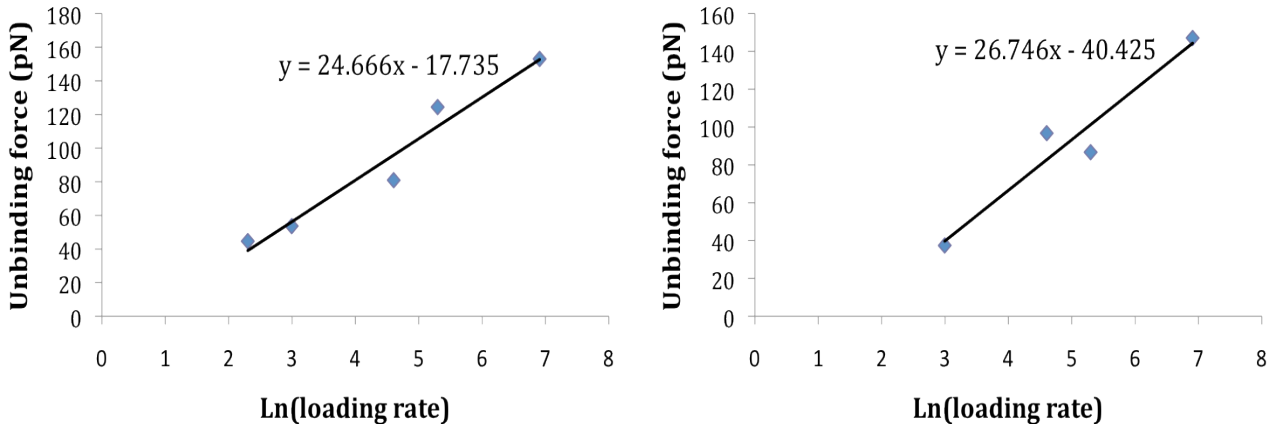

Figure 3-15: Derivation of TCR dimer-pMHC dissociation rate through the Bell model. The unbinding force between dimeric 2C* TCR and SIRGL-K^b (left) and dimeric 2C TCR and p2Ca-K^b (right) is plotted against the natural logarithm of the loading rate, and the data points are joined by a best-fit line, whose equation is displayed in the plot. From the slope and the y-intercept of this line, a χ_β and k_{Dim} are respectively calculated.

respectively. For 2C* TCR dimer associating with SIRGL-K^b, χ_β was found to be 1.67 Å (1 Å = 1×10^{-10} m), and k_{Dim} was 0.054 sec^{-1}. A χ_β and k_{Dim} value was similarly determined for the association of dimeric 2C TCR with p2Ca-K^b (Figure 3-15). With a spring constant of 0.2 pN/nm for the PEG/TCR-pMHC assembly and unbinding forces of 37+/-26 pN, 97+/-37 pN,

87+/-38 pN pN, and 147+/-84 pN, the Bell model yielded a χ_β of 1.54 Å and a k_{off} of 0.170 sec^{-1} for 2C TCR dimer associating with p2Ca-K^b.

3.4 Discussion

Observing that endogenous pMHC ligands can crucially affect both the sensitivity of antigen detection by T cells and the outcome of thymocyte selection, it is important to be able to measure the weak binding strengths they induce, in terms of K_D or k_{off}, in order to investigate these T cell phenomena in depth. The current work explored the possibility of applying DFS to study TCR-pMHC conjugates, with the goal of using this technique to expand the lower limit of the currently measurable affinity range. A model that is commonly used in DFS studies is the Bell model (equation 3.3), which allows the derivation of k_{off} of a ligand-receptor pair from the force required to unbind the pair at different loading rates.

No prior studies have been conducted to measure the unbinding force between a dimeric TCR and a pMHC so a direct comparison of the values obtained in the current study to the literature is not possible. In order to gauge the reliability of the present findings, the unbinding force of a TCR-pMHC pair could be estimated from the energy barrier of the bond. Rearranging equation (3.1) gives

$$E_b = k_B T \ln\left(\frac{1}{k_{off}(0)t_D}\right) \tag{3.4}$$

Since energy equals force times distance, E_b can be approximated as $F^*\chi_\beta$. Therefore,

$$F \sim \frac{E_b}{\chi_\beta} = \frac{k_B T}{\chi_\beta} \ln\left(\frac{1}{k_{off}(0)t_D}\right) \tag{3.5}$$

For two receptor-ligand systems, the ratio of their unbinding forces is

$$\frac{F_1}{F_2} = \frac{\frac{k_B T}{\chi_\beta^1} \ln(\frac{1}{k_{off}^1(0)t_D^1})}{\frac{k_\beta T}{\chi_\beta^2} \ln(\frac{1}{k_{off}^2(0)t_D^2})} \tag{3.6}$$

Assuming χ_β and t_D for the two systems are similar, equation (3.6) simplifies to

$$\frac{F_1}{F_2} = \frac{\ln(k_{off}^2(0)t_D)}{\ln(k_{off}^1(0)t_D)} \tag{3.7}$$

Thus, once F_1, $k_{off}^1(0)$, $k_{off}^2(0)$, and t_D are known, the unbinding force F_2 can be estimated from equation (3.7). Using the well-studied receptor-ligand pair streptavidin and biotin as the reference system, previous studies reported its F and k_{off} to be 5-170 pN [59] and 2.4 x 10^{-6} s^{-1} [226], respectively. k_{off} for the interaction of monomeric 2C* TCR and SIRGL-K^b has

been determined to be 6.6 x 10^{-3} s^{-1} [53], and molecular dynamics studies showed that 1/ t_D is 10^9-10^{10} s^{-1} [228]. Substituting these numbers into the above expression results in an estimated unbinding force of 7-223 pN for the 2C* TCR monomer–SIRGL-K^b interaction. The forces obtained for the unbinding of a 2C* TCR dimer from SIRGL-K^b in the present study are on the same order of magnitude as the calculated forces.

Even though molecules are attached to surfaces in DFS experiments, they possess 3-dimensional orientational freedom made possible by the long, flexible polymer linkers that connect them to the substrates. As a result, the reaction geometry of these molecules is more similar to TCR interacting with pMHC in solution than to TCR binding with pMHC on the cell membrane, where the molecular movement is confined to two dimensions. Therefore, we deemed that comparison of the results obtained in the present work to those gathered from in vitro SPR experiments, in which the receptor is bound to a surface and the ligand is flown over the receptor, would be more appropriate than to findings from cell-based experiments, such as those conducted by Huang *et al.* and Huppa *et al.* [229, 230].

Using the Bell model, the χ_β and k_{Dim} for the interaction of 2C* TCR dimer with SIRGL-K^b were determined to be 1.67 Å and 0.054 sec^{-1}, respectively. A k_{off} of this TCR-pMHC system but with the TCR in the monomeric form has been measured by Holler *et. al.* using SPR and was reported as 0.0066 sec^{-1} [53]. A smaller dissociation rate was expected of the dimeric than the monomeric TCR as increasing the valence of a molecule is supposed to promote binding. However, a larger dissociation constant was also measured by Sulchek

et. al. using AFM (2.6 x 10^{-3} sec^{-1}) than using SPR (0.4 x 10^{-3} sec^{-1}) in their work probing the same interaction involving Mucin1 peptide and a single-chain variable fragment antibody against the peptide [230]. The dimerization of the 2C* TCR in this case makes determining the source of the present discrepancy difficult. Nevertheless, the observed difference in k_{off} seems to depend partly on the robustness of the AFM data. A quick calculation (data not shown) revealed that by decreasing the slope of the force-versus-loading-rate plot by 1 pN, the calculated k_{off} altered from 0.054 sec^{-1} to 0.078 sec^{-1}. This result indicates that when DFS is utilized, it is very important to collect a large number of force curves to improve the resolution of the unbinding force.

Analysis of 2C TCR dimer binding to p2Ca-K^b uncovered a χ_β of 1.54 Å and a k_{Dim} of 0.170 sec^{-1}. The affinity for this TCR-pMHC pair was previously assessed to be roughly 300 μM via competitive binding assays [36], but a dissociation constant for this system does not appear to be available in the literature due to the extremely weak conjugation of 2C TCR with the spMHC ligand p2Ca-K^b. The present demonstration that DFS could be successfully used to determine a dissociation rate for this system suggests capability of this methodology at probing very weak TCR-pMHC interactions that are challenging to the conventional techniques. In order to compare the present result to the literature, an association rate (k_{on}) is estimated to convert the derived dissociation rate to an affinity. A previous kinetics study via SPR on 2C TCR dissociating from their ligands revealed a k_{on} of 2.2 x 10^3 and 2.3 x 10^3 $s^{-1}M^{-1}$ for dEV8-K^b and SIRGL-K^b, respectively [53]. Like p2Ca, dEV8 is also a self-peptide in the 2C system that induces weak binding of 2C TCR to K^b, with a K_D of 84.1 μM. In contrast, the SIRGL peptide induces strong binding of 2C TCR and K^b,

generating a K_D of 31.9 μM. Observing that despite being at the two ends of the affinity spectrum the two peptides have similar association rates, it is assumed that the k_{on} for the present case may be approximated as 2.2×10^3 $s^{-1}M^{-1}$. This value together with 0.170 sec^{-1} for k_{Dim} results in a K_D of 77.3 μM, a factor of 3.88 lower than the 300 μM obtained when 2C TCR is in the monomeric form [36]. It is expected that a TCR dimer would bind tighter than a TCR monomer to a pMHC due to increased valence in the former, and this is indeed the trend observed here. Since the k_{on} used in this estimation is for the 2C TCR monomer and is likely a larger value for a dimeric situation, the K_D determined is probably an underestimate of the actual number. A prior work found k_{off} for SIRGL-K^b and dEV8-K^b interacting with 2C TCR to be 0.075 sec^{-1} and 0.185 sec^{-1} respectively [53]. The 0.170 sec^{-1} calculated in this case is much closer to the latter value, a result that makes sense since both p2Ca and dEV8 are self-peptides and induce weak 2C TCR-K^b binding.

It should be noted that just like SPR, DFS does not take into account the contribution of the CD8 or CD4 coreceptor to the binding of TCR and pMHC. However, the coreceptor can drastically improve the sensitiviy of TCR-pMHC when the affinity is low. This facilitation is prominently demonstrated by Holler *et al.*, who found efficient stimulation of T cells displaying high affinity TCRs (K_D of 5-3000 nM, $t_{1/2}$ of 30-1500 s) regardless of the presence of CD8 [65]. In contrast, CD8 increased the efficiency of stimulation in T cells with low affinity TCRs (K_D values above 3 μM) by as many as seven and nine orders of magnitude in the presence of CD8α and both CD8α and CD8β, respectively. In addition, like any cell-free system, factors that are only intact in a cell that also influence TCR-pMHC binding, such as the glycosylation state of the TCR [232] and the

membrane micronenvironment [233], cannot be investigated using the present experimental setup.

The sample preparation procedure of DFS is quite demanding, with multiple molecule-attaching and washing steps during which the proteins to be studied may become denatured. Because the densities of the receptor and their ligand are tailored very low to achieve a single-molecule condition, unbinding events are rare so hundreds of force-distance curves need to be collected to build a good force histogram. This makes the data acquisition process very lengthy. Finally, quite a large volume of the ligand and receptor solutions is needed to coat the AFM probe (~50 μL) and the sample substrate, which can be an issue when the supply of the molecules is limited or if the molecules are pricey. Despite these shortcomings, DFS offers many advantages over the currently available methods. The setup of the system allows direct probing of the interaction of a single TCR-pMHC pair when low densities of the molecules are placed on the probe and sample substrate. This is a possibility that conventional methods, such as SPR, cannot offer. Furthermore, TCR-pMHC avidity may be studied by using multimeric TCR and pMHC ligands and tailoring the ligand densities. Finally, this system enables investigation of TCR-pMHC dissociation rates at the biological temperature of 37^{o}C with the usage of a commercially available sample holder equipped with a heating device. A similar experiment is challenging for SPR since both the association and dissociation rates become elevated at 37^{o}C, which makes accurate detection of TCR-pMHC unbinding events difficult [194].

Chapter 4 Conclusions

T Cell Mechanical Property Characterization

T cells are required by their biological roles to recirculate in the body and migrate to tissue sites to perform their immunological functions. During this journey they experience external forces that distort their shapes and physical barriers that can potentially interrupt their movement. Thus, successful and unimpeded migration requires these cells to possess sufficient deformability, supplied by their cytoskeleton, to accommodate and respond to the physical constraints demanded by their environment. Understanding the deformability of T cells motivates investigation of their mechanical properties, which quantitatively characterize a cell's capacity to deform and allow comparisons to be made across different cell types. The mechanical responses of a cell also reflect its cytoskeletal configuration and integrity, thus providing a way to gauge the cytoskeletal dissimilarities between two cell populations. Finally, computer simulations of T cell behaviors require the cells' mechanical properties as inputs and can help predict alteration of these behaviors under abnormal and hypothetical circumstances, such as in the presence of diseases and potential drug candidates that affect T cell migration. The literature on the biomechanics of nonadherent cells, with a small subset of it on T cells, provides mostly qualitative observations and data. Therefore, it was a goal of this thesis work to quantitatively characterize T cell deformability. We chose to study the elastic and viscous behaviors of T cells as these two

properties are important determinants of many aspects of leukocyte migration, including tethering, rolling, and diapedesis.

This work specifically examined T cell mechanical properties before and after the cell activation process. This particular scenario is important because T cells are only equipped with effector functions that can combat infections when they are activated, and activated T cells no longer adopt the same migration route as their naïve counterparts but instead travel to infection sites. Assuming that cells have mechanical capacity that facilitates their biological roles and functions, we hypothesized a change in the mechanical properties of T cells upon activation. Micropipette aspiration and AFM experimental procedures were designed and conducted to determine the elastic and viscous properties of naïve and activated T cells. For the latter technique, microwell arrays were fabricated and used to physically confine cells and prevent them from lateral movement. A statistically significant reduction of more than two folds in the apparent Young's modulus of T cells was discovered as a result of cell activation. The average modulus was 290+/-102 Pa and 94+/-49 Pa for naïve and activated T cells, respectively. This work is one of the very few studies that quantify the stiffness of primary T cells. This is the first time that elasticity changes in T cells were studied in the context of their activation state. Inspection of the variation of the apparent Young's modulus with deformation rate revealed a possible increase in the viscous resistance to cell movement if naïve T cells were to migrate at high speeds (> 10 μm/sec).

This work also investigated the elastic and viscous behaviors of WAS-/- T cells. One characterizing symptoms of the WAS genetic disease is progressive immunodeficiency, which causes frequent infections in WAS patients. Works uncovering the underlying pathophysiology found decreased cellularity in lymphoid organs and impaired T cell migration, both homing in vivo and chemotaxis in vitro. Since cell movement critically depends on the cytoskeleton, this observation suggests abnormal cytoskeletal organization in WAS-/- T cells that may translate into altered mechanical properties compared to WT T cells. The same micropipette aspiration and AFM experimental procedures used for WT T cells were applied to WAS-/- T cells. An apparent Young's modulus of 190+/-69 Pa and 121+/-41 Pa was determined for naïve and activated WAS-/- T cells, respectively. The former is 1.5 times smaller than that of naïve WT cells, and the latter does not result in a statistically significant difference when compared with activated WT cells. However, an impaired viscous response was observed in activated WAS-/- T cells. These results suggest that the WAS disease confers inappropriate mechanical properties on T cells, which may partly explain the aberrant migration behavior of the affected cells. Compared to the more than two folds reduction of the elastic modulus in WT cells upon activation, WAS-/- cells yielded a mere 1.6-fold decrease. This study is the first time that the elastic property of WAS-/- T cells, both in the naïve and activated states, has been quantitatively determined. This is also the first work that probes the viscous response of WAS-/- T cells and reveals impairment in this response in activated WAS-/- cells.

Chemokines are known to promote T cell extravasation by mobilizing the molecular machinery and signaling cascade responsible for cell movement, inducing

redistribution of cytoskeletal elements and cell membrane molecules. The result is a polarized, motile cell. In light of the impaired chemotaxis exhibited by WAS-/- T cells in in vitro experiments, it was desired to better understand the influence of chemokines on T cell deformability. Tranwell migration experiments were setup to induce T cell migration toward a chemokine source. Micropipette aspiration testing of naïve WT and naïve WAS-/- T cells that migrated in response to the stimulation revealed a drastic modulus reduction from 290+/-102 Pa to 128+/-33 Pa for the former, but an insignificant decrease from 190+/-69 Pa to 152+/-102 Pa for the latter. This finding suggests that one way that chemokines facilitate T cell transmigration is by reducing the elasticity of these cells. The present result also suggests that the abnormal chemotactic behavior of WAS-/- T cells may be due to their inability to reorganize their cytoskeleton, most likely the actin network as WAS is an a regulator of actin, to acquire sufficient deformability for transmigration.

Determination Of TCR-pMHC Dissociation Rate Using Dynamic Force Microscopy

It is important and essential to study TCR recognition of and binding to pMHC as this process is key in many biological phenomena involving T cells. In the thymus, thymocytes with TCR that can bind self pMHC ligands but do so only weakly are selected for survival and allowed to develop into mature T cells. Mature T cells egress the thymus and begin circulating in the body to participate in immunosurveillance. They must be activated by

APCs that present antigenic pMHC recognizable by their membrane-bound TCR to mount immune responses. As means to maintain a diverse pool of T cells in the body in preparation for any infectious agent, a naïve T cell must compete with other naïve T cells and with memory T cells having the same TCR type for spMHC and pro-survival cytokines. Those that have limited or no access to these resources will respectively be maintained at low copy numbers or die out.

A great amount of effort has been devoted to characterizing TCR-pMHC interactions, and it is known that the peptide presented by the MHC determines whether a positive signal, rescuing a thymocyte from apoptosis or activating a naïve T cell, or a negative signal, deleting a thymocyte or failing to trigger T cell activation, is delivered. The nature of these signals depends on how strongly the TCR binds to the pMHC, which has been shown to correlate with the affinity (K_D) or the dissociation rate (k_{off}) of the conjugate. The biological consequence induced in a T cell results from the sum of the individual TCR-pMHC signals, or the TCR-pMHC avidity, that the cell senses when interacting with an APC. As the thymocyte maturation process involves TCR binding to MHC complexes that present self-peptides, which typically induce very weak interactions between the molecules, it is important and essential to be able to measure very weak TCR-pMHC interactions. Furthermore, endogenous pMHC ligands have been shown to participate in T cell recognition of antigen and enhance the sensitivity of this process. A technique capable of probing fast molecular dissociation may allow the kinetic basis of this involvement to be revealed.

Many methodologies have been employed to determine K_D or k_{off}, with SPR being the most widely used technique. Despite the abundant results that SPR has generated, applying this technique to weakly conjugated TCR-pMHC pairs can be challenging as the interactions can approach the detection limit of the instrument. Signals from weak interactions may be boosted by increasing the protein concentration used for a SPR experiment, but this manipulation can raise the noise level of the detected response and reduce its accuracy, as well as can potentially lead to underestimation of the k_{off} value due to limited mass transport of the analyte. Observing these limitations, this work explored the possibility of using another method, DFS (dynamic force spectroscopy), to probe weak TCR-pMHC interactions. DFS is an AFM-based procedure that has been successfully applied to a large number of receptor-ligands systems to determine their k_{off} values.

A sample preparation protocol was developed to attach TCR and pMHC molecules to substrates using PEG linkers without compromising the biological functions of the proteins. The linkers facilitated identification of specific binding events from nonspecific adhesion and conferred orientational freedom to the receptors and ligands to promote their binding. As pMHC complexes become unstable when the peptide unbinds, special incubation and washing steps had to be designed to preserve their integrity. In addition, since DFS relies on the detection of a single receptor-ligand pair, samples were prepared with low protein densities that still satisfied this criterion. A testing procedure was developed to determine the experimental conditions that revealed the unbinding forces of two TCR-pMHC systems, 2C* TCR binding to SIRGL-K^b and 2C TCR binding to p2Ca-K^b, at different AFM loading rates. The latter system involves an extremely weak

interaction such that a dissociation rate has not been measured. These forces were subsequently used to derive k_{off} values for the two systems. Assessment of the accuracy of the present results shows them to be on the same order of magnitude as values reported in the literature. The k_{off} of the interaction of 2C* TCR with SIRGL-K^b is more than three folds larger than that of 2C TCR binding to p2Ca-K^b, a result in agreement with the much higher affinity of the former than the latter. This preliminary finding supports the application of DSF to probe TCR-pMHC interactions and suggests the capability of this technique at investigating cases that involved very weak TCR-pMHC interactions.

Chapter 5 System Improvements and Follow-Up Work

This work measured the apparent Young's modulus of T cells and found a reduction in the modulus both when WT cells were activated and in WAS-/- T cells compared to their WT partners. It was suspected that in the absence of WASp a defective cytoskeleton was formed that gave rise to a decrease in stiffness. This idea may be investigated by disrupting the cytoskeleton of WT T cells with drugs and measuring the change in the elastic modulus in these cells to see if the result might be comparable to those obtained from WAS-/- cells. If a cytoskeletal component is fluorescently labeled, the micropipette device offers the possibility to simultaneously deform a cell by aspira-tion and observe how the stained component rearranges in response to the applied force. This capability is useful when it is desired to study the time-dependent response of the cell cytoske-leton.

For the present work, a linear elastic solid model was chosen to analyze the data based on the knowledge that naïve T cells have a large nucleus to cytoplasm ratio. Even though this model could fit naïve T cells well, it did not satisfactorily describe the elastic behavior of about 30% of the activated T cells. The latter population appeared to exhibit a fluid-like nature. Therefore, a more advanced mathematical model able to account for both solid-like and liquid-like mechanical responses should be used for future studies on activated T cells. The linear elastic solid model does not directly yield a viscosity value but

allows the viscous nature of two cells to be compared based on their apparent elastic moduli at different loading rates. To directly quantify the viscosity, creep experiments could be conducted on T cells using the micropipette aspiration device, and the data could be fitted using a standard solid model to output an elastic modulus and a viscosity.

This work showed a reduction in the stiffness of naïve WT T cells that underwent transwell migration in response to chemokine stimulation. To try to decouple the influence that chemokine exposure and cell migration have on this measured stiffness, the apparent Young's modulus should be separately measured for cells without chemokine stimulation, cells stimulated with chemokine but do not migrate, and cells stimulated with chemokine and transmigrate in response. The transwell migration assay may be repeated using activated T cells to observe if the change in the cell activation state changes the elasticity requirement for transmigration. Finally, the expo-sure of T cells to chemokines and cytoskeleton-disrupting agents simultaneously may reveal insightful information on how the cells process opposing signals.

Preliminary results from the current study demonstrate the potential of using DFS to study very weak receptor-ligand interactions, in this case TCR-MHC binding in the presence of a self-peptide. Because it was desired to probe a single TCR-pMHC pair, the density of the TCR and pMHC on the interacting surfaces was kept low, resulting in few binding events. This number was further reduced by the non-directional binding of the homobifunctional PEG linker to the TCR dimer (or the pMHC), which relied on the reaction of one of its NHS ester groups with any –NH2 group on the protein, as well as by the

extremely weak conjugation of the TCR dimer to the spMHC. The outcome is rare observation of binding events that makes data collection very lengthy and cumbersome. Therefore, an improvement of the AFM experimental system is to engineer unique chemical groups into the TCR and the MHC to achieve directional binding. A possible approach is the addition of a –SH group to the carboxyl terminus of the K^b heavy chain, which can react with a maleimide group on a PEG linker to always orient the binding groove of K^b outward. Since the derivation of a dissociate rate through the Bell model relies on the slope of the best-fit line that fits the unbinding forces at different loading rates, accurate determination of these forces is essential. Therefore, the data pool from this work needs to be increased to create better unbinding force histograms.

Additional studies should be conducted to verify the preliminary results reported here. Other devices, such as a biomembrane force probe and optical tweezers, may be used to repeat the unbinding force measurements to obtained force values for comparison. The same AFM procedure should be repeated for monomeric 2C and 2C* TCRs, and the affinity values thus obtained should be compared to those reported in the literature. To complement these data, SPR studies could be conducted using TCR dimers to see if a k_{off} similar to that derived from the present results could be obtained.

Bibliography

1. Kuby Immunology, 6th Edition. Kindt TJ, Goldsby RA, Osborne BA (Eds.), W. H. Freeman and Company, New York, 2007.

2. Popel AS and Pittman RN. Biomechanics Principles and Applications, Schneck DJ and Bronzino JD (Eds.), CRC Press, 2003, pp.215-226.

3. http://psychology.wikia.com/wiki/Thymus_gland

4. http://www.britannica.com/EBchecked/media/17657/Internal-and-external-structures-of-a-lymph-node

5. http://immunotrends.blogspot.com/2010/04/t-lymphocyte-family-at-glance.html

6. http://bioweb.wku.edu/courses/biol328/tcr.htm

7. Vicente-Manzanares M, Sánchez-Madrid F (2004) Role of the cytoskeleton during leukocyte responses. *Nature Rev Immunol* 4:110-122.

8. Kole TP, Tseng Y, Jiang I, Katz JL, Wirtz D (2005) Intracellular mechanics of migrating fibroblasts. *Mol Bio Cell* 16:328–338.

9. Nieminen M, Henttinen T, Merinen M, Marttila–Ichihara F, Eriksson JE, Jalkanen S (2006) Vimentin function in lymphocyte adhesion and transcellular migration. *Nature Cell Bio* 8:156-162.

10. Jacobelli J, Bennett FC, Pandurangi P, Tooley AJ, Krummel MF (2009) Myosin-IIA and ICAM-1 regulate the interchange between two distinct modes of T cell migration. *J Immunol* 182:2041–2050.

11. Lautenschlager F, Paschke S,1, Schinkinger S, Bruel A, Beil M, Guck J (2009) The regulatory role of cell mechanics for migration of differentiating myeloid cells. *Proc Natl Acad Sci USA* 106:15696-15701.

12. Mora JR, von Andrian UH (2006) T-cell homing specificity and plasticity: new concepts and future challenges. *Trends Immunol* 27:235-243.

13. Norman MU, Hickey MJ (2005) Mechanisms of lymphocyte migration in autoimmune disease. *Tissue Antigens* 66:163–172.

14. Thrasher AJ (2002) WASp in immune-system organization and function. *Nature Rev Immunol* 2:635-646.

15. Symons M. *et al.* (1996) Wiskott–Aldrich syndrome protein, a novel effector for the GTPase Cdc42Hs, is implicated in actin polymerization. *Cell* 84:723–734.

16. Aspenstrom P, Lindberg U, Hall A (1996) Two GTPases, Cdc42 and Rac, bind directly to a protein implicated in the immunodeficiency disorder Wiskott–Aldrich syndrome. *Curr Biol* 6:70-75.

17. Billadeau DD, Nolz JC, Gomez TS (2007) Regulation of T-cell activation by the cytoskeleton. *Nature Rev Immunol* 7:131-143.

18. Zhang J *et al.* (1999) Antigen receptor–induced activation and cytoskeletal rearrangement are impaired in Wiskott-Aldrich syndrome protein–deficient lymphocytes. *J Exp Med* 190: 1329–134.

19. Snapper SB *et al.* (2005) WASP deficiency leads to global defect of directed leukocyte migration in vitro and in vivo. *J Leuk Bio* 77:993-998.

20. Gallego MD, de la Fuente MA, Anton IM, Snapper S, Fuhlbrigge R, Geha RS (2006) WIP and WASP play complementary roles in T cell homing and chemotaxis to SDF-1α. *Int Immunol* 18:221–32.

21. Park EY *et al.* (2002) Comparison of PSGL-1 microbead and neutrophil rolling: microvillus elongation stabilizes P-selectin bond clusters. *Biophys J* 82:1835–1847.

22. McCarty OJ, Tien N, Bochner BS, Konstantopoulos K (2003) Exogenous eosinophil activation converts PSGL-1-dependent binding to CD18-dependent stable adhesion to platelets in shear flow. *Am J Physiol Cell Physiol* 284:C1223–C1234.

23. Dong C, Lei XX (2000) Biomechanics of cell rolling: shear flow, cell-surface adhesion, and cell deformability. *J Biomechanics* 33:35-43.

24. Finger E, Bruehl RE, Bainton DF, Springer TA (1996) A Differential Role for Cell Shape in Neutrophil Tethering and Rolling on Endothelial Selectins Under Flow. *J Immunol* 157:5085-5096.

25. Merryman WD, Youn I, Lukoff HD, Krueger PM, Guilak F, Hopkins RA, Sacks MS (2006) Correlation between heart valve interstitial cell stiffness and transvalvular pressure: implications for collagen biosynthesis. *Am J Physiol Heart Circ Physiol* 290: H224 –H231.

26. Cuerrier CM, Gagner A, Lebel R, Gobeil F Jr, Grandbois M (2009) Effect of thrombin and bradykinin on endothelial cell mechanical properties monitored through membrane deformation. *J Mol Recognit* 22: 389–396.

27. Titushkin I, Cho M (2006) Distinct Membrane Mechanical Properties of Human Mesenchymal Stem Cells Determined Using Laser Optical Tweezers. *Biophy J* 90: 2582-2591.

28. Eekhoff A, Bonakdar N, Alonso JL, Hoffmann B, Goldmann WH (2011) Glomerular podocytes: A study of mechanical properties and mechano-chemical signaling. *Biochem Biophy Res Com* In Press.

29. Goldmann WH (2000) Mechanical manipulation of animal cells: cell indentation. *Biotech Lett* 22: 431–435.

30. http://www.cartage.org.lb/en/themes/Sciences/LifeScience/GeneralBiology/Immunology/Recognition/MajorHistocompatibility/StructureMHC/StructureMHC.htm

31. www.lesc.ic.ac.uk/ projects/appp.html

32. Davis MM (2004) Panning for T-cell gold High resolution and video microscopy begin to reveal molecular underpinnings of T-cell recognition. *TheScientist* 18:28.

33. Huppa JB, Davis MM (2003) T-cell-antigen recognition and the immunological synapse. *Nature Rev Immunol* 3:973-983.

34. Goldrath AW, Bevan MJ (1999) Selecting and maintaining a diverse T-cell repertoire. *Nature* 402:255-262.

35. Mahajan VS, Leskov IB, Chen J (2005) Homeostasis of T Cell Diversity. *Cell Mol Immunol* 2:1-10.

36. Sykulev Y, Brunmark A, Jackson M, Cohen RJ, Peterson PA, Eisen HN (1994) Kinetics and affinity of reactions between an antigen-specific T cell receptor and peptide-MHC complexes. *Immunity* 1:15-22.

37. Tian S, Maile R, Collins EJ, Frelinger JA (2007) CD8+ T cell activation is governed by TCR-peptide/MHC affinity, not dissociation rate. *J Immunol* 179:2952-60.

38. Schmid DA *et al.* (2010) Evidence for a TCR affinity threshold delimiting maximal CD8 T cell function. *J Immunol* 184:4936-4946.

39. Matsui K, Boniface JJ, Steffner P, Reay PA, Davis MM (1994) Kinetics of T-cell receptor binding to peptide/I-Ek complexes: correlation of the dissociation rate with T-cell responsiveness. *Proc Natl Acad Sci USA* 91:12862–12866.

40. Lyons DS, Lieberman SA, Hampl J, Boniface JJ, Chien YH, Berg LJ, Davis MM (1996) A TCR binds to antagonist ligands with lower affinities and faster dissociation rates than to agonists. *Immunity* 5:53–61.

41. Kersh GJ, Kersh EN, Fremont DH, Allen PM (1998) High- and low-potency ligands with similar affinities for the TCR: the importance of kinetics in TCR signaling. *Immunity* 9:817–826.

42. McKeithan TW (1995) Kinetic proofreading in T-cell receptor signal transduction. *Proc Natl Acad Sci USA* 92:5042–5046.

43. Irvine DJ, Purbhoo MA, Krogsgaard M, Davis MM (2002) Direct observation of ligand recognition by T cells. *Nature* 419:845-849.

44. Purbhoo MA, Irvine DJ, Huppa JB, Davis MM (2004) T cell killing does not require the formation of a stable mature immunologi- cal synapse. *Nat Immunol* 5:524–530.

45. Krogsgaard M, Juang J, Davis MM (2007) A role for "self" in T-cell activation. *Semin Immunol* 19:236–244.

46. Li QJ et al. (2004) CD4 enhances T cell sensitivity to antigen by coordinating Lck accumulation at the immunological synapse. *Nature Immunol* 5:791–799.

47. Watanabe N, Arase H, Onodera M, Ohashi PS, Saito T (2000) The quantity of TCR signal determines positive selection and lineage commitment of T cells. *J Immunol* 165:6252-6261.

48. Ashton-Rickardtand PG, Tonegawa S (1994) A differential-avidity model for T-cell selection. *Immunol Today* 15:362-366.

49. van den Berg HA, Rand DA (2007) Quantitative theories of T-cell responsiveness. *Immunol Rev* 216: 81–92.

50. Allen PM (1994) Peptides in positive and negative selection: a delicate balance. *Cell* 76:593–596.

51. Alam SM, Travers PJ, Wung JL, Nasholds W, Redpath S, Jameson SC, Gascoigne NR (1996) T-cell-receptor affinity and thymocyte positive selection. *Nature* 381:558–559.

52. Alam SM *et al.* (1999) Qualitiative and quantitative differences in T cell receptor binding of agonist and antagonist ligands. *Immunity* 10:227–237.

53. Holler PD, Kranz DM (2003) Quantitative analysis of the contribution of TCR/pepMHC affinity and CD8 to T cell activation. *Immunity* 18:255-264.

54. Dutz JP, Tsomides TJ, Kageyama S, Rasmussen MH, Eisen HN (1994) A cytotoxic T lymphocyte clone can recognize the same naturally occurring self peptide in association with a self and a nonself class I MHC protein. *Mol Immunol* 31:967-975.

55. Ober *et al.* (2000) Affinity of thymic self-peptides for the TCR determines the selection of CD8+ T lymphocytes in the thymus. *Int Immunol* 12:1353-1363.

56. Homola J, Yee SS, Gauglitz G (1999) Surface plasmon resonance sensors: review. *Sensors Actuators B* 54:3–15.

57. Ivarsson B and Malmqvist M Surface Plasmon resonance Development and use of BIACORE instruments for biomolecular interaction analysis. "Biomolecular Sensor", p.241-268, edited by Gizeli E and Lowe CR.

58. Krogsgaard M, Li Q-J, Sumen C, Huppa JB, Huse M, Davis MM (2005) Agonist/endogenous peptide–MHC heterodimers drive T cell activation and sensitivity. *Nature* 434:238-243.

59. Merkel R, Nassoy P, Leung A, Ritchie K, Evans E (1999) Energy landscapes of receptor–ligand bonds explored with dynamic force spectroscopy. *Nature* 397:50-53.

60. Schwesinger *et al.* (2000) Unbinding forces of single antibody-antigen complexes correlate with their thermal dissociation rates. *Proc Natl Acad Sci USA* 97:9972-9977.

61. Bonanni B *et al.* (2005) Single molecule recognition between cytochrome C551 and gold-immobilized azurin by force spectroscopy. *Biophy J* 89:2783-2791.

62. Yu J *et al.* (2007) Single-molecule force spectroscopy study of interaction between transforming growth factor β1 and its receptor in living cells. *J Phys Chem* 111:13619-13625.

63. Taranta M, Bizzarri AR, Cannistraro S (2008) Probing the interaction between p53 and the bacterial protein azurin by single molecule force spectroscopy. *J Mol Recognit* 21:63-70.

64. Baumgartner W, Hinterdorfer P, Ness W, Raab A, Vestweber D, Schindler H, Drenckhahn D (2000) Cadherin interaction probed by atomic force microscopy. *Proc Natl Acad Sci USA* 97:4005–4010.

65. Holler PD, Lim AR, Cho BK, Rund LA, Kranz DM (2001) $CD8^-$ T cell transfectants that express a high affinity T cell receptor exhibit enhanced peptide-dependent activation. *J Exp Med* 194:1043-1052.

66. Vestweber D (2007) Adhesion and signaling molecules controlling the transmigration of leukocytes through endothelium. *Immunol Rev* 218: 178–196.

67. Beltman JB, Marée AFM, Lynch JN, Miller MJ, de Boer RJ (2007) Lymph node topology dictates T cell migration behavior. *J Exp Med* 204:771-780.

68. Miller MJ, Wei SH, Parker I, Cahalan MD (2002) Two-photon imaging of lymphocyte motility and antigen response in intact lymph node. *Science* 296:1869-1873.

69. Stein JV, Nombela-Arrieta C (2005) Chemokine control of lymphocyte trafficking: a general overview. *Immunology* 116:1–12.

70. Cinamon G, Shinder V, Alon R (2001) Shear forces promote lymphocyte migration across vascular endothelium bearing apical chemokines. *Nature Immuno* 2:515-522.

71. Kishimoto TK, Hollander N, Roberts TM, Anderson DC, Springer TA (1987) Heterogeneous mutations in the β subunit common to the LFA-1, Mac-1, and p150,95 glycoproteins cause leukocyte adhesion deficiency. *Cell* 50:193–202.

72. Etzioni A, Harlan JM, Pollack S, Phillips LM, Gershoni-Baruch R, Paulson JC (1993) Leukocyte adhesion deficiency (LAD) II: a new adhesion defect due to absence of sialyl Lewis X, the ligand for selectins. *Immunodeficiency* 4:307–308.

73. Aspenstrom P, Lindberg U, Hall A (1996) Two GTPases, Cdc42 and Rac, bind directly to a protein implicated in the immunodeficiency disorder Wiskott–Aldrich syndrome. *Curr Biol* 6:70-75.

74. Haddad E *et al.* (2001) The interaction between Cdc42 and WASP is required for SDF-1–induced T-lymphocyte chemotaxis. *Blood* 97:33-38.

75. Zicha D *et al.* (1998) Chemotaxis of macrophages is abolished in the Wiskott-Aldrich syndrome. *Br J Hem* 101:659-665.

76. Badolato R *et al.* (1998) Monocytes from Wiskott-Aldrich patients display reduced chemotaxis and lack of cell polarization in response to monocyte chemoattractant protein-1 and formyl-methionyl-leucyl-phenylalanine. *J Immunol* 161:1026-1033.

77. Zhang H *et al.* (2006) Impaired integrin-dependent function in Wiskott-Aldrich syndrome protein-deficient murine and human neutrophils. *Immunity* 25:285–295.

78. Binks M, Jones GE, Brickell PM, Kinnon C, Katz DR, Thrasher AJ (1998) Intrinsic dendritic cell abnormalities in Wiskott-Aldrich syndrome. *Eur J Immunol* 28:3259-3267.

79. Schmid-Schonbein GW, Sung K-L P, Tozeren H, Skalak R, Chien S (1981) Passive mechanical properties of human leukocytes. *Biophys J* 36:243-256.

80. Pasternak C, and Elson EL (1985) Lymphocyte mechanical response triggered by cross-linking surface receptors. *J Cell Bio* 100:860-872.

81. Wu Y *et al.* (2009) Membrane surface nanostructures and adhesion property of T lymphocytes exploited by AFM. *Nanoscale Res Lett* 4:942–947.

82. Cai X, Xing X, Cai J, Chen Q, Wu S, Huang F (2010) Connection between biomechanics and cytoskeleton structure of lymphocyte and Jurkat cells: An AFM study. *Micron* 41:257-262.

83. Evans E and Kukan B (1984) Passive material behavior of granulocytes based on large deformation and recovery after deformation tests. *Blood*, 64:1028.

84. Evans E and Yeung A (1989) Apparent viscosity and cortical tension of blood granulocytes determined by micropipet aspiration. *Biophys J*, 56:151.

85. Tsai MA, Frank RS, Waugh RE (1994) Passive mechanical behavior of human neutrophils: effect of Cytochalasin B. *Biophys J*, 66:2166.

86. Needham D and Hochmuth RM (1992) A sensitive measure of surface stress in the resting neutrophil. *Biophys J*, 61:1664.

87. Tsai MA, Frank RS, Waugh RE (1993) Passive mechanical behavior of human neutrophils: power-law fluid. *Biophys J*, 65:2078.

88. Tran-Son-Tay R *et al.* (1991) Time-dependent recovery of passive neutrophils after large deformation. *Biophys J*, 60:856.

89. Hochmuth RM *et al.* (1993) Viscosity of passive human neutrophils undergoing small deformations. *Biophys J*, 64:1596.

90. Zhelev DV, Needham D, Hochmuth RM (1994) Role of the membrane cortex in neutrophil deformation in small pipets. *Biophys J*, 67:696.

91. Lim CT, Zhou EH, Quek ST (2006) Mechanical models for living cells—a review. *J Biomech* 39:195–216.

92. Small JV, Stradal T, Vignal E, Rottner K (2002) The lamellipodium: where motility begins. *Trends Cell Bio* 12:112-120.

93. Lammermann T, Sixt M (2009) Mechanical modes of 'amoeboid' cell migration. *Curr Opin Cell Bio* 21:636–644.

94. Janmey PA, Euteneuer U, Traub P, Schliwa M (1991) Viscoelastic properties of vimentin compared with other filamentous biopolymer network. *J Cell Bio* 113:155-160.

95. Wolosewick JJ (1984) Distribution of actin in migrating leukocytes in vivo. *Cell Tissue Res* 236:517-525.

96. Gabriele S, Benoliel A-M, Bongrand P, Theodoly O (2009) Microfluidic investigation reveals distinct roles for actin cytoskeleton and myosin II activity in capillary leukocyte trafficking. *Biophys J* 96: 4308–4318.

97. Jacobelli J, Chmura SA, Buxton DB, Davis MM, Krummel MF (2004) A single class II myosin modulates T cell motility and stopping, but not synapse formation. *Nature Immunol* 5:531-538.

98. Ratner S, Sherrod WS, Lichlyter D (1997) Microtubule retraction into the uropod and its role in T cell polarization and motility. *J Immunol* 159:1063-1067.

99. Fuchs E, Cleveland DW (1998) A structural scaffolding of intermediate filaments in health and disease. *Science* 279:514-519.

100. Brown MJ, Hallam JA, Colucci-Guyon E, Shaw S (2001) Rigidity of circulating lymphocytes is primarily conferred by vimentin intermediate filaments. *J Immunol* 166:6640-6646 (2001).

101. Brown MJ, Hallam JA, Liu Y, Yamada KM, Shaw S (2001) Integration of human T lymphocyte cytoskeleton by the cytolinker plectin. *J Immunol* 167:641-645.

102. Nieminen M, Henttinen T, Merinen M, Marttila–Ichihara F, Eriksson JE, Jalkanen S (2006) Vimentin function in lymphocyte adhesion and transcellular migration. *Nature Cell Bio* 8:156-162.

103. Fooksman DR *et al.* (2010) Functional anatomy of T cell activation and synapse formation. *Annu Rev Immunol* 28:79–105.

104. Reicher B, Barda-Saad M (2010) Multiple pathways leading from the T-cell antigen receptor to the actin cytoskeleton network. *FEBS Lett* 584:4858–4864.

105. Geiger B, Rosen D, Berke G (1982) Spatial relationships of microtubule-organizing centers and the contact area of cytotoxic T lymphocytes and target cells. *J Cell Biol* 95:137–143.

106. Kupfer A, Dennert G, Singer SJ (1983) Polarization of the Golgi apparatus and the microtubule- organizing center within cloned natural killer cells bound to their targets. *Proc Natl Acad Sci USA* 80:7224–7228.

107. Kupfer A, Mosmann TR, Kupfer H (1991) Polarized expression of cytokines in cell conjugates of helper T cells and splenic B cells. *Proc Natl Acad Sci USA* 88:775–779.

108. Faure S *et al.* (2004) ERM proteins regulate cytoskeleton relaxation promoting T cell–APC conjugation. *Nature Immunol* 5:272-279.

109. Burkhardt JK, Carrizosa E, Shaffer MH (2008) The actin cytoskeleton in T cell activation. *Annu Rev Immunol* 26:233-259.

110. Alon R, Feigelson S (2002) From rolling to arrest on blood vessels: leukocyte tap dancing on endothelial integrin ligands and chemokines at sub-second contacts. *Semin Immunol* 14:93-104.

111. Brown MJ *et al.* (2003) Chemokine stimulation of human peripheral blood T lymphocytes induces rapid dephosphorylation of ERM proteins, which facilitates loss of microvilli and polarization. *Blood* 102: 3890-3899.

112. Ridley AJ *et al.* (2003) Cell migration: integrating signals from front to back. *Science* 302:1704–1709.

113. Barreiro O, de la Fuente H, Mittelbrunn M, Sanchez-Madrid F (2007) Functional insights on the polarized redistribution of leukocyte integrins and their ligands during leukocyte migration and immune interactions. *Immunol Rev* 218:147–164.

114. Carman CV *et al.* (2007) Transcellular diapedesis is initiated by invasive podosomes. *Immunity* 26:784–797.

115. Friedman RS, Jacobelli J, Krummel MF (2005) Mechanisms of T cell motility and arrest: Deciphering the relationship between intra- and extracellular determinants. *Sem Immunol* 17:387–399.

116. Carman CV, Springer TA (2008) Trans-cellular migration: cell-cell contacts get intimate. *Curr Opin Cell Biol* 20:533–540.

117. Sarantos MR *et al.* (2008) Transmigration of neutrophils across inflamed endothelium is signaled through LFA-1 and Src family kinase. *J Immunol* 181:8660–8669.

118. Barreiro O *et al.* (2002) Dynamic interaction of VCAM-1 and ICAM-1 with moesin and ezrin in a novel endothelial structure for adherent leukocytes. *J Cell Biol* 157:1233–1245.

119. Carman CV, Springer TA (2004) A transmigratory cup in leukocyte diapedesis both through individual vascular endothelial cells and between them. *J Cell Biol* 167:377–388.

120. Cuvelier SL, Patel KD (2001) Shear-dependent eosinophil transmigration on interleukin 4–stimulated endothelial cells: A role for endothelium-associated eotaxin-3. *J Exp Med* 194:1699-1709.

121. Moazzam F, DeLano FA, Zweifach BW, Schmid-Schonbein GW (1997) The leukocyte response to shear stress. *Proc. Natl Acad. Sci. USA* 94:5338–5343.

122. Rabodzey A, Alcaide P, Luscinskas FW, Ladoux B (2008) Mechanical forces induced by the transendothelial migration of human neutrophils. *Biophys J* 95:1428–1438.

123. de Bruyn PPH (1946) The amoeboid movement of the mammalian leukocyte in tissue culture. *Anat Rec* 95:117–192.

124. Nourshargh S, Hordijk PL, Sixt M (2010) Breaching multiple barriers: leukocyte motility through venular walls and the interstitium. *Nature Rev Mol Cell Biol* 11:366-378.

125. Campbell DJ, Kim CH, Butcher EC (2003) Chemokines in the systemic organization of immunity. *Immunol Rev* 195:58–71.

126. Forster R, Mattis AE, Kremmer E, Wolf E, Brem G, Lipp M (1996) A putative chemokine receptor, BLR-1, directs B cell migration to defined lymphoid organs and specific anatomic compartments of the spleen. *Cell* 87:1037-1047.

127. Kurihara T, Warr G, Loy J, Bravo R (1997) Defects in macrophage recruitment and host defense in mice lacking the CCR2 chemokine receptor. *J Exp Med* 186:1757-1762.

128. Campbell JJ, Butcher EC (2000) Chemokines in tissue-specific and microenvironment-specific lymphocyte homing. *Curr Opin Immunol* 12:336–341.

129. Foxman EF, Kunkel EJ, Butcher EC (1999) Integrating conflicting chemotactic signals: the role of memory in leukocyte navigation. *J Cell Biol* 147:577-588.

130. Foxman EF, Campbell JJ, Butcher EC (1997) Multistep navigation and the combinatorial control of leukocyte chemotaxis. *J Cell Biol* 139:1349-1360.

131. Hochmuth RM (2000) Micropipette aspiration of living cells. *J Biomech* 33:15-22.

132. Alcaraz J, Buscemi L, Grabulosa M, Trepat X, Fabry B, Farre R, Navajas D (2003) Microrheology of human lung epithelial cells measured by atomic force microscopy. *Biophys J* 84:2071–2079.

133. Zhang H, Liu K-K (2008) Optical tweezers for single cells. *J R Soc Interface* (2008) 5:671–690.

134. Maksym GN, Fabry B, Butler JP, Navajas D, Tschumperlin DJ, Laporte JD, Fredberg JJ (2000) Mechanical properties of cultured human airway smooth muscle cells from 0.05 to 0.4 Hz. *J App Physiol* 89: 1619–1632.

135. Thoumine O, Albrecht Ott A (1997) Time scale dependent viscoelastic and contractile regimes in fibroblasts probed by microplate manipulation. *J Cell Sci* 110:2109-2116.

136. Zahalak GI, McConnaughey WB, Elson EL (1990) Determination of cellular mechanical properties by cell poking, with an application to leukocytes. *J Biomech Eng* 112:283-294.

137. Suresh S (2007) Biomechanics and biophysics of cancer cells. *Acta Biomaterialia* 3:413–438.

138. Rosenbluth MJ, Lam WA, Fletcher DA (2006) Force microscopy of nonadherent cells: a comparison of leukemia cell deformability. *Biophys J* 90:2994-3003.

139. Kasas S, Ikai A (1995) A method for anchoring round shaped cells for atomic force microscope imaging. Biophys J 68: 1678-1680.

140. van der Mei HC, Busscher HJ, Bos R, de Vries J, Boonaert CJP, Dufrene YF (2000) Direct probing by atomic force microscopy of the cell surface softness of a fibrillated and nonfibrillated oral streptococcal strain. *Biophys J* 78:2668–2674.

141. Jones WR, Ting-Beall HP, Lee GM, Kelley SS, Hochmuth RM, Guilak F (1999) Alterations in the Young's modules and volumetric properties of chondrocytes isolated from normal and osteoarthritic human cartilage. *J Biomechanics* 32:119-127.

142. Sato M, Theret DP, Wheeler LT, Ohshima N, Nerem RM (1990) Application of the micropipette technique to the measurement of cultured porcine aortic endothelial cell viscoelastic properties. J BiomechEng 112:263-268.

143. Khalilian M, Navidbakhsh M, Valojerdi MR, Chizari M, Yazdi PE (2010) Estimating Young's modulus of zona pellucida by micropipette aspiration in combination with theoretical models of ovum. *J R Soc Interface* 7: 687-694.

144. Frank RS (1990) Time-dependent alterations in the deformability of human neutrophils in response to chemotactic activation. *Blood* 76: 2606–2612.

145. Van Vliet KJ, Bao G, Suresh S (2003) The biomechanics toolbox: experimental approaches for living cells and biomolecules. *Acta Materialia* 51:5881–5905.

146. Mills JP, Qie L, Dao M, Lim CT, Suresh S (2004) Nonlinear elastic and viscoelastic deformation of the human red blood cell with optical tweezers. *MCB* 1:169-180.

147. Brandao MM, Fontes A, Barjas-Castro ML, Barbosa LC, Costa FF, Cesar CL, Saad STO (2003) Optical tweezers for measuring red blood cell elasticity: application to the study of drug response in sickle cell disease. *Eur J Haematol* 70:207–211.

148. Maksym GN, Fabry B, Butler JP, Navajas D, Tschumperlin DJ, Laporte JD, Fredberg JJ (2000) Mechanical properties of cultured human airway smooth muscle cells from 0.05 to 0.4 Hz. *J App Physiol* 89: 1619–1632.

149. Park EY, Smith MJ, Stropp ES, Snapp KR, DiVietro JA, Walker WF, Schmidtke DW, Diamond SL, Lawrence MB (2002) Comparison of PSGL-1 microbead and neutrophil rolling: microvillus elongation stabilizes P-selectin bond clusters. *Biophys J* 82:1835–1847.

150. McCarty OJ, Tien N, Bochner BS, Konstantopoulos K (2003) Exogenous eosinophil activation converts PSGL-1-dependent binding to CD18-dependent stable adhesion to platelets in shear flow. *Am J Physiol Cell Physiol* 284:C1223–C1234.

151. Jadhav S, Eggleton CD, Konstantopoulos K (2005) A 3-D Computational Model Predicts that Cell Deformation Affects Selectin-Mediated Leukocyte Rolling. *Biophys J* 88:96-104.

152. Dong C, Lei XX (2000) Biomechanics of cell rolling: shear flow, cell-surface adhesion, and cell deformability. *J Biomechanics* 33:35-43.

153. Finger E, Bruehl RE, Bainton DF, Springer TA (1996) A Differential Role for Cell Shape in Neutrophil Tethering and Rolling on Endothelial Selectins Under Flow. *J Immunol* 157:5085-5096.

154. Theret DP, Levesque MJ, Sato M, Nerem RM, Wheeler LT (1988) The application of a homogeneous half-space model in the analysis of endothelial cell micropipette measurements. *Trans ASME* 110:190–199.

155. Costa KD, Yin FCP (1999) Analysis of indentation: implications for measuring mechanical properties with atomic force microscopy. *J Biomech Eng* 121:462-471.

156. Costa KD (2006) Imaging and probing cell mechanical properties with the atomic force microscope. *Methods Mol Bio* 319:331-361.

157. Barda-Saad M, Braiman A, Titerence R, Bunnell SC, Barr VA, Samelson LE (2005) Dynamic molecular interactions linking the T cell antigen receptor to the actin cytoskeleton. Nature Immunol 6:80-89.

158. Sancho D, Vicente-Manzanares M, Mittelbrunn M, Montoya MC, Gordón-Alonso M, Serrador JM, Sánchez-Madrid F (2002) Regulation of microtubule-organizing center orientation and actomyosin cytoskeleton rearrangement during immune interactions. *Immunol Rev* 189:84-97.

159. Collins SJ, Gallo RC, Gallagher RE (1977) Continuous growth and differentiation of human myeloid leukemic-cells in suspension culture. *Nature* 270:347-349.

160. Parsey MV, Lewis GK (1993) Actin polymerization and pseudopod reorganization accompany anti-CD3-induced growth arrest in Jurkat T cells*. J Immunol* 151:1881-1893.

161. Titushkin I, Cho M (2007) Modulation of cellular mechanics during osteogenic differentiation of human mesenchymal stem cells. *Biophys J* 93: 3693–3702.

162. Mathur AB, Collinswortha AM, Reicherta WM, Krausb WE, Truskey GA (2001) Endothelial, cardiac muscle and skeletal muscle exhibit different viscous and elastic properties as determined by atomic force microscopy. *J Biomech* 34:1545-1553.

163. Guilak, Farshid *et al.* (1999) Viscoelastic Properties of Intervertebral Disc Cells: Identification of Two Biomechanically Distinct Cell Populations. *Spine* 24:2475-2483.

164. Koay EJ, Shieh AC, Athanasiou KA (2001) Development of a novel method for creep indentation of single chondrocytes. *Ann Biomed Eng* 29:S22.

165. Dong C, Skalak R, Sung KL (1991) Cytoplasmic rheology of passive neutrophils. *Biorheology* 28:557-567.

166. Gallego MD, Santamaria M, Pena J, Molina IJ (1997) Defective actin reorganization and polarization of Wiskott-Aldrich T cells in response to CD-mediated stimulation. *Blood* 90:3089-3097.

167. Goley ED, Welch MD (2006) The ARP2/3 complex: an actin nucleator comes of age. *Nat Rev Mol Cell Biol* 7:713–26.

168. Ardouin L, Bracke M, Mathiot A, Pagakis SN, Norton T, Hogg N, Tybulewicz VLJ (2003) Vav1 transduces TCR signals required for LFA-1 function and cell polarization at the immunological synapse. Eur J Immunol 33:790–797.

169. Nagayama M, Haga H, Kawabata K (2001) Drastic change of local stiffness distribution correlating to cell migration in living fibroblasts. *Cell Motility Cytoskeleton* 50:173–179.

170. Su J, Brau RR, Jiang X, Whitesides GM, Lange MJ, So PT (2007) Geometric confinement influences cellular mechanical properties II—intracellular variances in polarized cells. *Mol Cell Biomech* 4: 105–118.

171. Yanai M, Butler JP, Suzuki T, Sasaki H, Higuchi H (2004) Regional rheological differences in locomoting neutrophils. *Am J Physiol Cell Physiol* 287: C603–C611.

172. Yamazaki D, Kurisu S, Takenawa T (2005) Regulation of cancer cell motility through actin reorganization. *Cancer Sci* 96: 379–386.

173. Azeloglu EU, Bhattacharya J, Costa KD (2008) Atomic force microscope elastography reveals phenotypic differences in alveolar cell stiffness. *J Appl Physiol* 105: 652–661.

174. Shroff SG, Saner DR, Lal R (1995) Dynamic micromechanical properties of cultured rat atrial myocytes measured by atomic force microscopy. *Am J Physiol Cell Physiol* 269: C286–C292.

175. Haga H, Sasaki S, Kawabata K, Ito E, Ushiki T, Abe K, Sambongi T (2000) Elasticity mapping of living fibroblasts by AFM and immunofluorescence observation of cytoskeleton. *Ultramicroscopy* 82:253–258.

176. Lima CT, Zhou EH,b, Quek ST (2006) Mechanical models for living cells - a review. *J Biomechanics* 39:195–216.

177. Loffler H, Gassmann W (1994) Morphology and cytochemistry of acute lymphoblastic leukaemia. *Baillieres Clin Haematol* 7:263–272.

178. Li QS, Lee GYH, Ong CN, Lim CT (2008) AFM indentation study of breast cancer cells. *Biochem Biophys Res Comm* 374:609–613.

179. Ohashi T, Ishii Y, Ishikawa Y, Matsumoto T, Sato M (2002) Experimental and numerical analyses of local mechanical properties measured by atomic force microscopy for sheared endothelial cells. *BioMed Mater Eng* 12:319–327.

180. Tsai MA, Waugh RE, Keng PC (1996) Cell cycle dependence of HL-60 cell deformability. *Biophys J* 70:2023.

181. Tsai MA, Waugh RE, Keng PC (1996) Changes in HL-60 cell deformability during differentiation induced by DMSO. *Biorheology* 33:1.

182. Palmer E, Naeher D (2009) Affinity threshold for thymic selection through a T-cell receptor– co-receptor zipper. *Nature Rev Immunol* 9:207-213.

183. Troy AE, Shen H (2003) Cutting edge: homeostatic proliferation of peripheral T lymphocytes is regulated by clonal competition. *J Immunol* 170:672-676.

184. Sprent J, Surh CD (2003) Cytokines and T cell homeostasis. *Immunol Lett.* 85:145-149.

185. Ge Q, Bai A, Jones B, Eisen HN, Chen J (2004) Competition for self-peptide-MHC complexes and cytokines between naïve and memory CD8+ T cells expressing the same or different T cell receptors. *Proc Natl Acad Sci USA* 101:3041-3046.

186. Friedl P, Gunzer M (2001) Interaction of T cells with APCs: the serial encounter model. *Trends Immunol* 22:187-191.

187. Henrickson SE, von Andrian UH (2007) Single-cell dynamics of T-cell priming. *Curr Opin Immunol* 19:249–258.

188. Liu C-P, Crawford F, Marrack P, Kappler J (1998) T cell positive selection by a high density, low affinity ligand. *Proc Natl Acad Sci USA* 95:4522–4526.

189. Rosette C *et al.* (2001) The impact of duration versus extent of TCR occupancy on T cell activation: a revision of the kinetic proofreading model. *Immunity* 15:59-70.

190. Ely LK *et al.* (2005) Antagonism of antiviral and allogeneic activity of a human public CTL clonotype by a single altered peptide ligand: implications for allograft rejection. *J Immunol* 174:5593-601.

191. Daniels MA *et al.* (2006) Thymic selection threshold defined by compartmentalization of Ras/MAPK signaling. *Nature* 444:724-729.

192. Miller MJ, Safrina O, Parker I, Cahalan MD (2004) Imaging the single cell dynamics of CD4+ T cell activation by dendritic cells in lymph nodes. *J Exp Med* 200:847-856.

193. Valitutti S, Muller S, Cella M, Padovan E, Lanzavecchia A (1995) Serial triggering of many T-cell receptors by a few peptide–MHC complexes. *Nature* 375:148-151.

194. Stone JD, Chervin AS, Kranz DM (2008) T-cell receptor binding affinities and kinetics: impact on T-cell activity and specificit. *Immunology* 126:165–176.

195. Kalergis AM, Boucheron N, Doucey MA, Palmieri E, Goyarts EC, Vegh Z, Luescher IF, Nathenson SG (2001) Efficient T cell activation requires an optimal dwell-time of interaction between the TCR and the pMHC complex. *Nat Immunol* 2:229-234.

196. Riquelme E, Carreño LJ, González PA, Kalergis AM (2009) The duration of TCR/pMHC interactions regulates CTL effector function and tumor-killing capacity. *Eur J Immunol* 39:2259–2269.

197. Holler PD, Lim AR, Cho BK, Rund LA, Kranz DM (2001) $CD8^-$ T cell transfectants that express a high affinity T cell receptor exhibit enhanced peptide-dependent activation. *J Exp Med* 194:1043-1052.

198. Weber KS, Donermeyer DL, Allen PM, Kranz DM (2005) Class II- restricted T cell receptor engineered in vitro for higher affinity retains peptide specificity and function. *Proc Natl Acad Sci USA* 102:19033–19038.

199. Zamoyska R (1998) CD4 and CD8: modulators of T-cell receptor recognition of antigen and of immune responses? *Curr Opin Immunol* 10:82–87.

200. Motyka B, Teh H-S (1998) Naturally Occurring Low Affinity Peptide/MHC Class I Ligands Can Mediate Negative Selection and T Cell Activation. *J Immunol* 160:77-86.

201. Matsui K, Boniface JJ, Reay PA, Schild H, Destgroth BF, Davis MM (1991) Low affinity interaction of peptide-MHC complexes with T cell receptors. *Science* 254:1788-1791.

202. Davis MM, Boniface JJ, Reich Z, Lyons D, Hampl J, Arden B, Chien Y (1998) Ligand recognition by alpha beta T cell receptors. *Annu Rev Immunol* 16:523–544.

203. Gascoigne NRJ, Zai T, Alam SM (2001) T-cell receptor binding kinetics in T-cell development and activation. *Exp Rev Mol Med* 12 February, http://www-ermm.cbcu.cam.ac.uk/01002502h.htm.

204. Boniface JJ *et al.* (1998) Initiation of signal transduction through the T cell receptor requires the multivalent engagement of peptide/MHC ligands *Immunity* 9:459-466.

205. Cochran JR, Cameron TO, Stern LJ (2000) The relationship of MHC-peptide binding and T cell activation probed using chemically defined MHC class II oligomers. *Immunity* 12:241-250.

206. Stone JD, Stern LJ (2006) CD8 T cells, like CD4 T cells, are triggered by multivalent engagement of TCRs by MHC-peptide ligands but not by monovalent engagement. *J Immunol* 176:1498-505.

207. Wulfing C *et al.* (2002) Costimulation and endogenous MHC ligands contribute to T cell recognition. *Nature Immunol* 3:42–47.

208. Krogsgaard M, Juang J, Davis MM (2007) A role for "self" in T-cell activation. Semin Immunol 19:236–244.

209. Davis SJ, Ikemizu S, Evans EJ, Fugger L, Bakker TR, van der Merwe PA (2003) The nature of molecular recognition by T cells. *Nat Immunol* 4:217–224.

210. Jameson SC, Hogquist KA, Bevan MJ (1995) Positive selection of thymocytes. *Annu Rev Immunol* 13:93.

211. Naeher D, Daniels MA, Hausmann B, Guillaume P, Luescher I, Palmer E (2007) A constant affinity threshold for T cell tolerance. *J Exp Med* 204:2553-2559.

212. Hogquist KA, Jameson SC, Heath WR, Howard JL, Bevan MJ, Carbone FR (1994) T cell receptor antagonist peptides induce positive selection. *Cell* 76:17.

213. Barnden MJ, Heath WR, Rodda S, Carbone FR (1994) Peptide antagonists that promote positive selection are inefficient at T cell activation and thymocyte deletion. *Eur J Immunol* 24:2452.

214. Hogquist KA, Jameson SC, Bevan MJ (1995) Strong agonist ligands for the T cell receptor do not mediate positive selection of functional $CD8^+$ T cells. *Immunity 3:79.*

215. Sebzda E, Wallace VA, Mayer J, Yeung RSM, Mak TW, Ohashi PS (1994) Positive and negative thymocyte selection induced by different concentrations of a single peptide. *Science* 263:1615.

216. Persaud SP, Donermeyer DL, Weber KS, Kranz DM, Allen PM (2010) High-affinity T cell receptor differentiates cognate peptide–MHC and altered peptide ligands with distinct kinetics and thermodynamics. *Mol Immunol* 47:1793–1801.

217. Colf LA *et al.* (2007) How a single T cell receptor recognizes both self and foreign MHC. *Cell* 129:135–146.

218. De Crescenzo G, Boucher C, Durocher Y, Jolicoeur M (2008) Kinetic characterization by surface plasmon resonance-based biosensors: principle and emerging trends. *Cell Mol Bioeng* 1:204–215.

219. Bell GI (1978) Models for the specific adhesion of cells to cells. *Science* 200:618-627.

220. Evans E, Ritchie K (1997) Dynamic strength of molecular adhesion bonds. *Biophy J* 72:1541-1555.

221. Brown BB, Wagner DS, Geysen HM (1995) A single-bead decode strategy using electrospray ionization mass spectrometry and a new photolabile linker: 3-Amino-3-(2-nitrophenyl)propionic acid. *Mol Diversity* 1:4-12.

222. http://tetramer.yerkes.emory.edu/client/protocols

223. www.elec-intro.com/ igd-immunoglobulin

224. Garcia KC, Tallquist MD, Pease LR, Brunmark A, Scott CA, Degano M, Stura EA, Peterson PA, Wilson IA, Teyton L (1997) Alphabeta T cell receptor interactions with syngeneic and allogeneic ligands: affinity measurements and crystallization. *Proc Natl Acad Sci USA* 94:13838-13843.

225. Riener et al (2003) Simple test system for single molecule recognition force microscopy. *Analytica Chimica Acta* 479:59-75.

226. Chen A and Moy VT (2000) Cross-Linking of Cell Surface Receptors Enhances Cooperativity of Molecular Adhesion. *Biophy J* 78:2814-2820.

227. Piran U, Riordan WJ (1990) Dissociation rate constant of the biotin-streptavidin complex. *J Immunol Methods* 133:141-143.

228. Grubmuller H, Heymann B, Tavan P (1996) Ligand binding: molecular mechanics calculation of the streptavidin-biotin rupture force. *Science* 271:997-999.

229. Huang J, Zarnitsyna VI, Liu B, Edwards LJ, Jiang N, Evavold BD, Zhu C (2010) The kinetics of two-dimensional TCR and pMHC interactions determine T-cell responsiveness. *Nature* 464:932-936.

230. Huppa JB *et al.* (2010) TCR–peptide–MHC interactions in situ show accelerated kinetics and increased affinity. *Nature* 463:963-967.

231. Sulchek *et al.* (2005) Dynamic force spectroscopy of parallel individual Mucin1-antibody bonds. *PNAS* 102:16638-16643.

232. Zhu DM, Dustin ML, Cairo CW, Golan DE (2007) Analysis of two-dimensional dissociation constant of laterally mobile cell adhesion molecules. *Biophys J* 92:1022–1034.

233. Lillemeier BF *et al.* (2010) TCR and LAT occur in separate membrane domains and concatenate during activation. *Nature Immunol* 11:90–96.